NATIONAL AND KAPODISTRIAN UNIVERSITY OF ATHENS
FACULTY OF GEOLOGY AND GEOENVIRONMENT

Division of Economic Geology and Geochemitry

Diploma Thesis

Petrographic and geochemical study of barite from actively forming, Au-rich polymetallic sulfide-sulfate hydrothermal chimneys from the shallow-submarine Kolumbo volcano, Hellenic (South Aegean) Volcanic Arc, Greece: contribution to the chimney growth model

Vasilios Pletsas

Supervisor: Prof. Stephanos P. Kilias

Athens 2022

Abstract

Seafloor Massive Sulfides (SMS) are thought to be the modern day analogue of the known Volcanogenic Massive Sulfides (VMS) that occur on the land. VMS are known to mankind for thousands of years being one the best targets for mineral resources, mainly copper. They also exhibit great enrichment in other base metals such as gold, silver, zinc and lead but also at trace elements such as antimony and thallium. It is of critical importance to study and understand how the SMS deposits are formed and grow both chronologically and spatially. SMS located at shallow water level systems are ideal for future potential recovery, than those at pelagic margins. There are two known shallow SMS systems inside European Union's exclusive economic water zones. One located at the Palinuro Volcanic Complex, Aeolian Island Arc, Italy and one at the Santorini Volcanic Complex, Hellenic (South Aegean) Volcanic Arc, on the crater floor of the Kolumbo shallow-submarine volcano.

Kolumbo submarine arc-volcano hydrothermal system that was first discovered in 2006 and it's the only known SMS deposit forming on continental thinned crust. Recent researches on hydrothermal chimney samples revealed an unusual enrichment in gold (Au), silver (Ag), copper (Cu), lead (Pb), zinc (Zn), antimony (Sb), arsenic (As), mercury (Hg), molybdenum (Mo) and thallium (Tl). The calculated Au to base metal ration over unity is 1.9, classifies the Kolumbo SMS as an auriferous-SMS deposit (Marcier-Langevin et al., 2011). The main sulfide minerals that make up the hydrothermal chimneys and mounds are pyrite, marcasite, sphalerite, galena, chalcopyrite, stibnite and unidentified Pb-Sb-sulfosalts and As-sulfides. Barite is the main sulfate mineral that constructs an initial wall, which in turn forms the substate matrix for the development of the sulfide SMS mineralization. In order to better understand the sulfide-sulfate chimneys growth model, we performed petrographic and geochemical study of the barite textures, as all the previous studies focused on the sulfides.

Reflected and transmitted light Optical Mineralogy and petrography work revealed that anhydrite is the first mineral phase to precipitate, which later dissolves and gets replaced by barite crystals. This dissolution of early anhydrite releases more SO_4^- ions making it easier for barite crystals to precipitate (Griffith et al., 2012). Anhydrite mainly occurs in the outer parts of the chimney as dissolution relics of anhedral to subhedral crystals that usually are replaced by barite and it is often related with small pyrite grains. Four different generations of barite mineralization displaying a great variety of textures, have been identified. The first generation consists of aggregates of large barite laths and blades, and rarer as recrystallized mosaic structures. The second generation is related with (Pyrite stage) mineralization and consists of big individual open-space filling laths and blades, but also as rosette and plumose aggregates usually lining open conduits. The third generation is related to (Zn-Pb-Sb stage) mineralization and it exhibits a great textural variation. This is typically found in the form of plumose, rosette and dendritic aggregates, but also needle-like crystals and individual blades and laths that create complex intergrowths have been identified. This generation is often related to both solid and fluid primary inclusions.

The fourth generation comprises the outer wall of the chimney where the As-sulfides are deposited. Again, in this generation the main petrographic type is plumose and rosette aggregates and zoned barite crystals related with As-sulfides due to co-precipitation.

Scanning Electron Microscopy (SEM) coupled with Energy Dispersive Spectroscopy (EDS) has revealed small concentrations of strontium (Sr), Zn, Fe, Pb, and As in the barite crystals showing that barite is directly related to the sulfide deposition.

Chimney growth begins with the formation of a sulfate (anhydrite) wall that the sulfides and sulfosalts precipitate on. Later, anhydrite dissolves and gets replaced by the first barite generation which is accompanied by colloform pyrite (Pyrite stage). Through the continuous hydrothermal activity and zone refinement processes the inner pyrite stage of the central parts of the chimney develops into the Zn-Pb-Sb stage that occurs at the outer parts of the Inner Sulfide-Sulfate Core (ISSC), which is dominated by pyrite± sphalerite± galena ±Pb-Sb-sulosalts while barite comprises the matrix. In the ISSC marcasite, ±galena ± sphalerite ± chalcopyrite and minor pyrite intergrowths form thin rims around pyrite channels in the Fe-Zn-Pb-Cu stage mineralization. Finally, on the surface of the chimney, the Outer Arsenic Layer (OAsL) is formed by co-precipitation of barite, As-Pb-Sb-sulfosalts, As-sulfides and stibnite during the last stages of mineralization as the product of mixing of hot hydrothermal fluids with cold seawater.

Acknowledgments

First of all, I would like to thank my parents for always being there for me and my brother and for their continuous support through all the stages of my life, I wouldn't be able to achieve anything without them.

I would also like to thank my fully committed supervisor Professor Stephanos Kilias for trusting me to work on this project with him and for always believing in me. I would also like to thank him for passing me down his passion for the science of Geology, nothing would be possible without his guidance. At this point I would also like to thank my very good friend and colleague Nikolaos Zegkinoglou for all of his aid throughout this thesis, all the helpful conversations and for making funnier this whole experience, I wish him the best of luck with his PhD research. I would also like to thank Dr. Clifford Patten and Simon Hector, KIT Karlsruhe for always helping with sample preparations and helpful conversations. I would like to also thank Professor Paraskevi Nomikou for all the sampling expeditions, providing us that way access to the mysteries of the Aegean.

I am also grateful to Vasilis Skounakis and to Dr Elizabeth Stathopoulou for aiding and helping me learn how to operate the SEM analyses and also Professor Maria Triantafyllou for granting me access to the SEM of the Division of Historical Geology.

Lastly, I would also like to thank my friends for making this Geological experience a lot better.

Table of contents

List of Acronyms and Abbreviations

Anh	Anhydrite
BSE	Backscatter electron
Brt	Barite
Cpy	Chalcopyrite
CKS	Christianna-Santorini-Kolumbo
CDR	Coupled Dissolution Reprecipitation
CRM	Critical Raw Materials
EDS	Energy Dispersive Spectroscopy
Gn	Galena
HCMR	Hellenic Centre Marine Research
HSA	Hellenic Sedimentary Arc
HSS	Hellenic Subduction System
HVA	Hellenic Volcanic Arc
IGME	Institute of Geology and Mineral Exploration
ISSC	Inner Sulfide-Sulfate Core
KHF	Kolumbo Hydrothermal Field
Mrc	Marcasite
MORB	Mid-Ocean-Ridge-Basalts
OAsL	Outer As-sulfide-dominated Layer
PXRD	Powder X-Ray Diffraction
Py	Pyrite
ROV	Remotely Operated Vehicle
SEM	Scanning Electron Microscopy
SFeC	Fe-(hydrated)-oxyhydroxide-dominated surface Fe crust
SMS	Seafloor Massive Sulfide
Sph	Sphalerite
Stb	Stibnite
USGS	United States Geological Survey
VMS	Volcanogenic Massive Sulfides

List of Tables

List of Figures

1. Introduction

A continuously evolving society cannot be maintained without the use of mineral resources. Particularly, the raw materials that are most important economically and have a high risk of supply are called Critical Raw Materials (CRM). In order to maintain a continuously evolving society, the use of CRM is of strategic importance. These materials have a wide variety of technological uses and are essential to establish a strong industrial economy. Furthermore in this time and age where the need for a low carbon emission society is necessary, due to the problems of climate change and that of overpopulation, CRM play a key role. To develop such a strong and independent economy alongside with an environmental friendly power source, the European Union focuses their interest into the search of CRM. (European Commission, Study on the EU's list of Critical Raw Materials – Final Report 2020).

A new perspective in the research for raw materials is exploration of marine/sub-marine environments. Regions of great interest for their concentration of metals and metalloids are the Modern seafloor hydrothermal systems and their associated Seafloor Massive Sulfide deposits (SMS) (Beaulieu et al., 2017, Hannington et al., 2017). These types of deposits are usually rich in base metals and often in CRM as they comprise the closest modern analogue of Volcanogenic Massive Sulfide (VMS) deposits. Also they are a natural laboratory for scientist to study and understand the ore forming processes as they unfold in real time (Monecke et al., 2016). Observing them can provide information about the nature of magmatic degassing or potential inputs from the subducted slab to the mantle wedge in arc-related settings, crustal fluid flow, metal and metalloids sources and their transportation and eventually their deposition on/below seafloor surface (e.g.,Von Damm, 1990; Rona and Scott, 1993; de Ronde et al.,2003; Hannington et al., 2005; Berkenbosch et al., 2012).

These diverse systems occur in various tectonic settings such as mid-ocean ridges (MOR) (Francheteau et al.,1979; Spiess et al.,1980; Fouquet et al., 1994; Kong et al.,1985; Krasnov et al., 1995; Murton et al., 1995; Rona et al., 1986; Halbach et al., 1998; Herzig and Plüger, 1988; Plüger et al., 1990; Connelly et al., 2012) and arc related settings (Both et al.,1986; Craig et al.,1986; Kastner et al.,1986; Fouquet et al.,1991; Halbach et al., 1989; Rogers et al., 2012; de Ronde et al.,2001; Stoffers et al., 1999; Wright et al., 1998). This difference of tectonic settings makes these types of deposits differ in many ways, mostly by the magmatic contributions of fluids and metals to the hydrothermal system (e.g. Hannington et al., 2005; de Ronde, 2005).

Arc- related hydrothermal venting systems with significant mineral potential can be found in Europe's two active magmatic arcs, the Aeolian and the Hellenic. Those two active systems are known for their shallow submarine (<500m) polymetallic sulfide mineral occurrences at Palinuro [Aeolian-arc], Panarea [Aeolian-arc], and Kolumbo [Aegean-arc] (Dekov et al., 2013; Kilias et al., 2013; Petersen et al., 2014), which resemble epithermal deposits located on land. Exploitation of these types of deposits on shallow-sea environment on continental margins faces fewer challenges compared to their deep-sea counterparts (Hannington et al., 2005). Also they can provide information about the circulation and the source of toxic metals (e.g. Sb, Hg, Tl) in marine environment. Further research on these models will bring into light the secrets of their genesis and evolution, as they are underexplored and little is known about them due to their complexity.

The SMS deposit that is currently being formed in the crater of Kolumbo shallow submarine arc-volcano, Santorini, Hellenic Volcanic Arc (HVA) is uniquely enriched in economically and environmentally significant metals and metalloids such as antimony (Sb), thallium (Tl), mercury (Hg), arsenic (As), gold (Au), silver (Ag), lead (Pb)and zinc (Zn), indicating a new hybrid seafloor analogue of epithermal to VMS deposits (Kilias et al. 2013). The average and maximum bulk concentrations of Au (9 ppm and 32 ppm respectively) are among the highest reported from modern seafloor hydrothermal systems worldwide (Kilias et al. 2013).

The major sulfate mineral that consist the matrix and plays a key role in the development of the chimneys is barite ($BaSO_4$). The sulfide minerals that are most abundant and therefore are the ones controlling the bulk concentrations of the metalloids in the system are pyrite (FeS_2), sphalerite (ZnS), galena (PbS) (Kilias et al. 2013).

2. Barium (Ba)

2.1 Physical Properties

Barium (Ba) belongs in the group of Alkaline Earth Elements and with an atomic number of 56, it can be found as the fifth element of group II in the periodic table. Its name originates from the Greek word “βαρύ-υς” which means “heavy”, explaining the high density of barium-containing minerals. The atomic weight of barium is calculated to 137.332 g/mol, making it not so heavy compared to other elements. Barium related minerals were first found in the early 1600s by Vincenzo Casciarolo in Bologna, Italy. But the first to discover the new unknown, for the times, element was Carl Wilhelm Scheele, as he was investigating some pyrolusite crystals. But it wasn’t isolated until 1808, when Sir Humphry Davy was the first to achieve it with the process of electrolysis of molten barium salts .Barium is a soft and ductile metal with a silver white lust when freshly cut (Ropp, 2013).

General properties of Barium	
Name, Symbol, Number	Barium, Ba, 56
Element Category	Alkaline Earth Metals
Group Period Block	2, 6, s
Standard Atomic Weight	137.33 $g \cdot mol^{-1}$
Electron Configuration	[Xe] 6 s2
Electrons per shell	2, 8, 18, 18, 8, 2
Physical Properties	
Phase	Solid
Density	(Near r.t) 3.51 $g \cdot cm^{-3}$
Liquid density at mp	3.338 $g \cdot cm^{-3}$
Melting Point	1000 K
Boiling Point	2170 K
Heat of fusion	7.12 $kJ \cdot mol^{-1}$
Heat of vaporization	140.3 $kJ \cdot mol^{-1}$

Specific heat capacity	(25 °C) 28.07 $J \cdot mol^{-1} \cdot K^{-1}$
Atomic Properties	
Oxidation states	2 (strongly basic oxide)
Electronegativity	0.89 (Pauling scale)
Ionization energies	1^{st} : 502.9 $kJ \cdot mol^{-1}$ 2^{nd}: 965.2 $kJ \cdot mol^{-1}$ 3^{rd} : 3600 $kJ \cdot mol^{-1}$
Atomic radius	222 pm
Covalent radius	215 ± 11 pm
Van der Waals radius	268 pm
Other Properties	
Crystal Structure	Body-centered cubic
Magnetic Ordering	Paramagnetic
Electrical resistivity	(20 °C) 332 nΩ·m
Thermal Conductivity	(300 K) 18.4 $W \cdot m^{-1} \cdot K^{-1}$
Thermal Expansion	(25 ° C) 20.6 $\mu m \cdot m^{-1} \cdot K^{-1}$
Mohs hardness	1.25

Table 1: The most important properties of Barium metal (Modified by Hanusa 2013).

Barium Isotopes				
Isotope	Z(p)	N(n)	Mass	Half-life
^{130}Ba	56	74	129.9063208	Primordial Radioactive [7E+13a]
^{132}Ba	56	76	131.9050613	STABLE [>300E+18 a]
^{133}Ba	56	77	132.9060075	10.51(5) a
^{134}Ba	56	78	133.9045084	Stable
^{135}Ba	56	79	134.9056886	Stable
^{136}Ba	56	80	135.9045759	Stable
^{137}Ba	56	81	136.9058274	Stable
^{138}Ba	56	82	137.9052472	Stable

Table 2: Presenting the all known barium Isotopes. All Ba isotopes are stable except ^{133}Ba (Modified by Hanusa, 2013).

2.2 Geochemistry

The concentration of barium in the Earth's crust is estimated around 0.03% making it the 14^{th} most abundant element in it. Although it's a very common metal in the crust, it can never be found free in nature due to its reactivity with air or in water. The most common form of barium in the geological environment is the divalent cation $Ba^{2+}$and its primary found in the minerals barite ($BaSO_4$) and Whiterite ($BaCO_3$) (Johnson et al., 2017).

The Ba^{2+} ion is a Large Ion Lithophile Element (LILE), meaning it has an affinity for silicate phases but its big size, compared to other divalent ions, doesn't allow it to precipitate in them. For that reason it can be concentrated in the residual silicate liquid, during the process of fraction crystallization of silicate magmas and in silicate liquids by partial melting. Although, in minerals containing the almost equally large ions Pb^{2+} and Sr^{2+}, substitution by Ba^{2+} is very common. Substitution for Ca^{2+} and K^{2+} is less common, with the second requiring a coupled substitution to maintain a balanced charge (Johnson et al., 2017).

In Igneous rocks, granitoids tend to have higher concentration of barium than basaltic rocks. It can be found as a trace element in potassium feldspars and micas, substituting for K^{+} and rarer in plagioclase, pyroxene, amphiboles and apatite substituting for Ca^{2+}. In metamorphic environments the most common barium bearing minerals are celsian ($BaAl_2Si_2O_8$), a member of alkali-feldspars, and sanbornite ($BaSi_2O_5$) both indicating high temperatures, as a product of contact metamorphism. In sedimentary and hydrothermal rocks the most common barium bearing minerals are barite ($BaSO_4$) and whiterite ($BaCO_3$). Barium can also occur in the organic matter in sedimentary rocks.

3. Barite ($BaSO_4$)

Barite is the predominant Ba-bearing mineral and it's known to compose a solid solution series with celestine ($SrSO_4$). The Barium end member of the series is believed to form in a wide range of P-T conditions (0 to 400 °C and 1 to 2000 bars) (Hanor 2000, Ehya et al. 2017) as it appears in a great variety of sedimentary, metamorphic and igneous geological environments dating from Early Archean (~3.5 Ga) to the present (Hanor, 2000).Due to the excessively low solubility of Barite (ca 10^{-10} at 25 °C, 1 atm; Church and Wolgemuth, 1972), mixing and interaction between distinct fluids enriched in Ba and SO_4 is a common mechanism causing barite to precipitate in both continental and marine environments (Hanor, 2000; Griffith and Paytan,2012, Ehya et al. 2017). Although, it's mostly precipitated by aqueous solutions (Hanor 2000). So basically Barite precipitation is primarily dependent on the availability of its ionic constituents (Griffith et al., 2012, Ford 2014):

$$Ba^{2+} + SO_4^{2-} \longrightarrow BaSO_4$$

In oxidizing environments barite appears to be strongly stable, but in Hydrogen Sulfide (H_2S) stable environments tends to be easily dissolved. This important attribute can help in better understanding of Barite dissolution and transportation in hydrothermal environments (Johnson et al., 2017).

3.1 Barite in Continental environments

Barite's extreme diversion makes it easy to mineralize in all kinds of environments, even at continental ones. Usually found in hydrothermal veins and seldom even in magmatic/metasomatic occurrences. All these mineralization types might be of different origins, but they all share a basic genetic attribute. The fluid that

transferred the ionic constituents of barite was of Temperatures higher than 100 °C. Regional tectonics controls these systems, as the structures it creates will later become the pathways the hydrothermal fluid will follow and eventually mineralize barite (Johnson et al., 2017).

Hydrothermal Barite Veins

Vein barite is the most common type in terrestrial environments. Typically, found in narrow rift basins that contain red beds and other terrigenous sediments (Johnson et al., 2017). Also, found cross-cutting igneous rocks and is rarer related with Au (gold) mineralization. The source of Ba is of igneous origin or leached from Ba-rich sediments, while the source of SO_4^- can be either from meteoric water or from metamorphic and magmatic fluids. Its solubility increases with increasing salinity between temperatures of 100-250 °C. So a model of mixing of late stage mineralization hydrothermal water with meteoric water is suggested. That can explain the reason Barite appears at the margins of the basin (Rye 2004).

Magmatic Barite

In carbonatites, although is very rare, magmatic crystallization of barite has been observed in few cases (Néron al., 2018). Carbonatites are igneous rocks that contain more than 50% primary (magmatic) carbonate and less than 20% SiO_2 (Le Maitre 2002). Experimental studies have shown that carbonatite magmas can crystallize barite Ba content is high (Néron et al., 2018). Well known example is the Mountain Pass, where primary euhedral barite crystals occur in a carbonatite (Néron et al., 2018).

3.2 Barite in Marine environments

As mentioned before barite can precipitate in a wide range of P-T conditions, making it able to precipitate in many different ways, even in the same (marine) environment. The main aspect, in all the models of barite precipitation, is the Interaction between the ingredients of barite-rich fluids, precisely Ba^{2+} and SO_4^- that will lead in supersaturation within the formation environment. It is believed there are four main models for barite precipitation that are distinguished according to the source of origin of the ingredients of barite (Griffith et al., 2012).

3.3 Marine or pelagic Barite

Degradation of organic matter can release Ba content, capable of creating supersaturated with respect to barite, micro-environments. This is known as Marine or pelagic barite (Goldberg and Arrhenius, 1958; Bishop, 1988; Bernstein et al., 1992, 1998; Ganeshram et al.,2003, Griffith et al., 2012). Barite usually precipitates in the water column, but the Ba concentration in sea water is lower than the amount of Ba in some marine organisms. That observation shows that marine organisms can be another possible source of Ba in the water column (Goldberg and Arrhenius, 1958; Bishop, 1988; Bernstein et al., 1992, 1998, Griffith et al., 2012). Marine barite precipitation is not limited by the depth factor, showing it can precipitate in a great range of depth in the water column (Van Beek et al., 2007, Griffith et al., 2012).

Biogenic Barite

Another precipitation mechanism of Marine barite that is worth mentioning is Biogenic precipitation of barite. This barite type precipitates from marine organisms, mostly algae and protozoa. It is thought that in order to maintain depth and orientation, they intercellularly produce barite crystals, to change their density (Arrhenius and Bonatti, 1965; Tendal, 1972; Gooday and Nott, 1982; Swinbanks and Shirayama, 1986, Griffith et al., 2012). Even though, there is no detailed research done to provide insight about the amount of barite that is precipitated by living organisms, it is believed that the amount is insignificant. As there is no planktonic organism identified to directly precipitate intercellular barite.

Barite is also possible to precipitate via bacterially activities. Marine bacteria might mediate the precipitation of barite by providing nucleation sites and enhancing crystal growth. Comparing the distribution of barite in the sea and the precipitation of barite by bacterial mediation is showing that they are in equilibrium. This can be explained by the high population of bacteria in organic-rich sinking aggregates. Although, more research needs to be done in the future, due to lack of direct observation, to actually prove this theory (Muñoz-González et al.,2003, Griffith et al., 2012).

3.4 Hydrothermal Barite

Ba-rich hydrothermal fluids, related with submarine volcanic activity, can produce hydrothermal barite, as a product of mixing with sea water, source of sulfate ion. Leaching, of rich in Ba oceanic or continental rocks can identify as the source of Ba for the hydrothermal fluids (Hanor, 2000, Ehya et al., 2017). Another possible source is hydrothermal leaching of pelagic sediments with high Ba content (Murchey et al., 1987, Griffith et al., 2012). The hydrothermal fluid will rise to the ocean floor through extensional faults and fractures, as they create a path for it due to differences in density. Decreasing in both pressure and temperature (T<100 °C) lowers the solubility of barite and thus enabling further the precipitation of barite during hydrothermal activities (Hanor, 2000, Griffith et al., 2012). The type and the concentration of the host volcanic rock or the sediments of the ocean floor are the key factor that will determine the composition and geochemistry of the hydrothermal fluid and eventually the occurrence of the barite. Another factor that influences the formation of barite is the temperature of the hydrothermal fluid. Barite can precipitate in low temperatures (T<120 °C) around warm springs on the sea floor. But it can also precipitate in intermediate temperatures (T; 150-250 °C) in continental margin forging either hydrothermal chimneys or mounds or within sediments as dispersed crystals in basement fractures at oceanic back-arc basin spreading centers, fracture zones and volcanic arcs. All these temperature dependent occurrences of barite show that there a lot of different hydrothermal environments in which barite can precipitate (Hein et al., 2007, Griffith et al., 2012).

3.5 Cold Seeps Barite

This barite type precipitates from the expulsion at the water-sediment interface and is related to the fluid flow. During lateral compressive tectonic processes or in high sedimentations rates, fluids in the pores of the sediments tend to move vertically. In the case of Ba-rich sediments, fluids with high Ba concentrations will be released. Finally, these fluids will reach the sea floor and will interact with the SO_4^--rich sea water and eventually precipitate barite. Usually, the tectonic setting that favors the

formation of Cold seeps barite is along transform faults in both active and passive margins. It can also be associated with salt tectonics, as they also regulate fluid emission (Gontharet et al., 2007, Griffith et al., 2012). The amount and the mineralogy of Barite that precipitates from Cold seeps depend on seepage rate and the geochemistry of the extracted fluids. In particular at low seepage rates (< ca 5 cm a^{-1}) barite precipitates only on the few top meters of the sedimentary column, creating microcrystalline phases and concretions. In contrast, at high rates of seepage (> ca 100 cm a^{-1}), barite precipitates vastly through-out the water column creating chimneys. About the chemistry of the fluids, at high Methane to barium levels (>4 to 11), carbonates precipitation is favored. At low Methane to barium levels, barite precipitation will be fostered (Aloisi et al., 2004, Griffith et al., 2012).

3.6 Diagenetic Barite

Another common way for barite to precipitate is after the deposition, through diagenetic processes. Generally, barite can be produced in diagenetic environments through the dissolution of barite by sulfate reduction in sediments succeeded by re-precipitation. In order to accomplish that, Ba-rich pore fluid need to react with pore water at the redox boundaries within the sediments. Barite precipitation within sediments can be achieved by alterations in temperature and pressure of the fluids. If these alterations affect (decrease) the solubility, barite can precipitate (Hanor, 2000, Griffith et al., 2012). Moreover, tectonic advection can cause over-pressured sediments and rock units to release fluids rich in Ba and SO_4^- and therefore induce barite precipitation (Hein et al., 2007). Barite has also been observed inside plankton tests, through diagenetic processes. Decomposition of organic matter within sediments can lead to Barite precipitation inside the tests (Stamatakis and Hein, 1993, Griffith et al., 2012). In anoxic conditions SO_4^- reduction rates are faster than the rate of SO_4- replenishment in the pore fluids. This will create a SO_4^- deficiency, which will not allow barite to precipitate. The residual Ba will concentrate in high volumes in the pore water. Further interaction between Ba and SO_4^- will induce barite precipitation within the sedimentary column, at the oxic-anoxic boundary (Bolze et al., 1974; Dean and Schreiber, 1977; Brumsack and Gieskes, 1983; Cecile et al., 1983; Breheret and Brumsack, 2000, Griffith et al., 2012). Dissolution of other minerals and mainly Anhydrite ($CaSO_4^-$) has an important impact in barite diagenesis. Dissolution of Anhydrite will contribute SO_4^- in the pore fluids of the sediments, which will interact with the Ba content in them, inducing barite precipitation (Monnin et al., 2003, Griffith et al., 2012).

3.7 Crystallography of Barite

Barite's crystallographic structure consists of BaO_6 octahedra and SO_4 tetrahedra and it is considered a member of the orthorhombic crystal group. The Ba cations are in [12]-coordination forming irregular coordination polyhedral, such as orthorhombic and dipyramidal. The Ba coordination, taking into account only the six nearest O neighbor atoms, can be represented by a distorted octahedron and the structure as built from chains of edge-sharing octahedra linked by SO_4 groups into sheets. These sheets are linked into a framework by corner-sharing between BaO_6 octahedra and SO_4 tetrahedra from adjacent sheets. The existence of these sheets explains the perfect cleavage of barite parallel to (001) (Hawthorne et al., 2000). The solid solution between barite and Celestine appears to be continuous and regular unlike the solid solution between barite and anhydrite that appears incomplete (Griffith et al., 2012).

Substitutions of Ba^{2+} in barite crystals are common. The most typical are Sr^{2+} (strontium), Ca^{2+} (calcium), K^{+} (potassium), Pb^{2+} (lead), REE (Rare Earth Elements). All these substitutions depend on the degree of similarity in charge, ionic radius and electronegativity of the trace cation in comparison to Ba^{2+} (Church, 1979; Guichard et al., 1979; Morgan and Wandless, 1980, Griffith et al., 2012). Rarer Fe^{2+} (iron), Cu^{2+} (copper), Zn^{2+} (zinc), Ag^{2+} (silver), Ni^{2+} (nickel), Hg^{2+} (mercury), V^{2+} (vanadium) have also been observed to substitute for Ba^{2+} in barite crystals (Chang et al., 1996, Griffith et al., 2012).
The great range of P-T conditions barite precipitate in a variety of geological settings has as a result plenty and different crystal morphologies and textures. In combination with solubility and saturation degree, the size of the crystals is also affected (Griffith et al., 2012). This can explain why barite occurs with so many diverse forms. Over seventy crystal morphologies have been observed with the most ordinary being tabular, prismatic, fibrous, rosette-like and granular (Anthony et al., 1990).

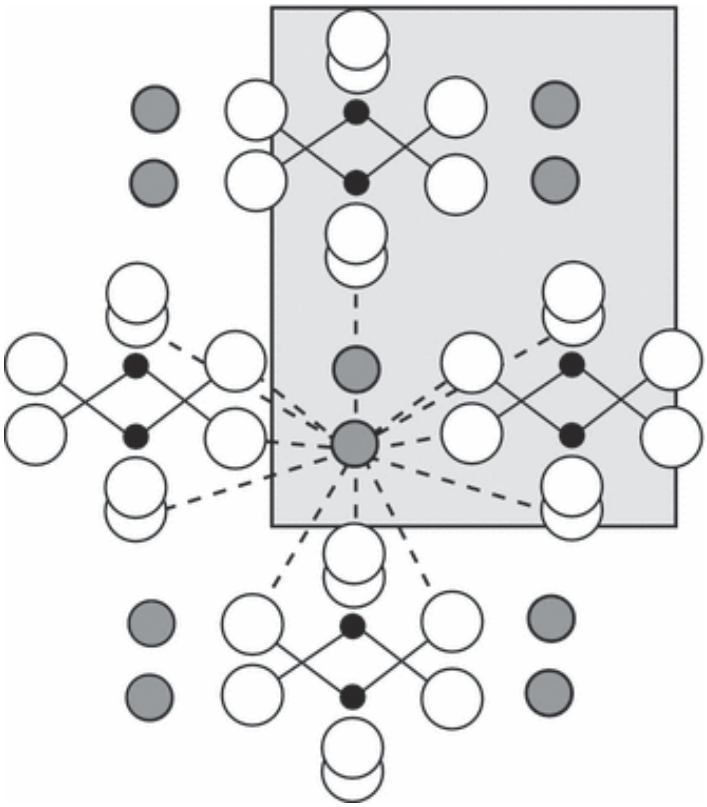

Figure 1: Crystal structure of barite. Gray: Ba atoms, White: Oxygen atoms, Black: Sulfur atoms (Griffith et al., 2012).

3.8 Optical and Physical Properties of Barite

Barite under transmitted light appears transparent to translucent and is usually colorless. Although, it may occur with many different colors such as white, yellow, brown, gray, blue, green and pale shades of red, due to impurities. The fact that it creates a solid solution series with celestine, can explain the existence of zoned barite, with repeatedly changes in Sr-Ba concentrations, as product of phase separation. Another possible explanation is because of the presence of impurities and fluid inclusions. Impurities are common because barite precipitates mainly from aqueous fluids. Exposure to light might cause a change to its color. Regarding its

optical class, barite is a biaxial crystal with weak pleochroism has a perfect cleavage at plane [001] and uneven fracture. It has a hardness of 3 to 3.5 in Mohs scale and brittle tenacity. Its density is estimated around 4.48 $g \cdot cm^{-3}$ which is almost twice the amount of common minerals, making it easy to distinguish. In nature it can occur with a vitreous to resinous luster and not so often pearly. When grind it leaves a streak color of white (Anthony et al., 1990).

3.9 Industrial and economic importance

As of September 2017 EU determined barite a Critical Raw Material (CRM), because of its high economic importance. The EU publishes a list of raw materials believed to be of strategic and critical importance to sustain and evolve the modern society. These materials are the key component to provide new green economies. Barite has a lot of significant applications in today's industry, with the most crucial being its use as weighting agent in oil and gas well drilling fluids or muds. Drilling muds are the fluids pumped into the drilling well to lubricate the bit and drill stem, remove rock chips, prevent collapse of the well and avert blowouts if overpressured strata are encountered (Johnson et al., 2017). The white color barite usually has makes it possible to be used as filler in rubber, plastic, paint and paper industries. Also known to find application in chemical industry as a feedstock. Moreover is suitable for shielding in X-ray and gamma-ray applications. Barite is the main source of Ba which is highly used in ceramic glazes, enamels, optical glass, primers, steel hardeners and welding fluxes (Johnson et al., 2017).

3.10 Scientific importance

Barite's many and diverse styles of precipitation in a variety of geologic environments, along its unique attributes, promote it to a great tool for geoscientists. The high endurance the mineral shows in oxic settings is one of the many attributes that make it special as a research material. Barites as old as 3.6 Ga are preserved unaltered until today, making it a perfect recorder for changes in geological time and helping to unlock the mysteries of the past. It's also suitable for studies of the origin of fluids and past water chemistry, as barite precipitates in the water column. It can help reconstruct past changes in ocean productivity as well. In short is one of the most favorable tools in paleoceanography. The hydrothermal origin of barite can provide information about the circulation of hydrothermal fluids in the crust, alongside their geochemistry and the conditions of crust alteration in the past (Grifftith et al., 2012). Its preservation abilities can also unhide information about how hydrothermal activity controlled the very first steps of primary life forms (Helge Mißbach et al., 2021). In economic geology find applications on how SMS-VMS deposit types are formed, show insight on the composition of the fluids that transferred the ore and lastly unlock the secrets of the ore's different styles of mineralization.

4. Modern Seafloor Massive Sulfide (SMS) deposits

4.1 Distribution and tectonic settings

Seafloor Massive Sulfide are precious and base metal carrying deposits that form on and below the seabed from the interaction of heated hydrothermal fluids with the Earth's crust. They are also considered to be the modern analogue of Volcanogenic Massive Sulfide deposits (VMS), which have been exploited for thousands of years

on the land (Petersen et al., 2018). The high demand for raw materials has intrigued the interest of both scientists and industries on the research and discovery of SMS deposits. Resulting in the detection of over 600 submarine hydrothermal systems over the last 40 years of searching (Beaulieu et a., 2013). It is known that SMS deposits are formed as the outcome of seawater circulation into and out of hot oceanic crust beneath the seabed (Petersen et al., 2018). Occurrence of hydrothermal venting sites and therefore, formation of SMS deposits have been observed in variety of geological settings with the majority of them being at plate boundaries ranging from mid-ocean ridges, to volcanic arcs and back-arc basins (de Ronde et al., 2005, Hannington et al., 2005, 2011). The common characteristic of these environments is they form at spreading and extension tectonic settings. A more detailed classification can be seen as the follow:

Mid-ocean ridges

i) Ultraslow-spreading ridges with spreading rates being less than 20mm/yr, such as the Arctic mid-ocean ridge segments (Edmonds et al., 2003, Pedersen et al., 2010a, b) and the Mid-Cayman spreading Centre (Connelly et al., 2012).

ii) Slow-spreading ridges with spreading rates estimated between 20 and 40 mm/yr, such as the Mid-Atlantic ridge (Fouquet et al., 1994, Krasnov et al., 1995) and the Central Indian ridge (Plüger et al., 1990).

iii) Intermediate-spreading ridges with spreading rates estimated between 40 and 60 mm/yr as seen in the Juan de Fuca ridge (Jamieson et al., 2014a) and at the Central Indian Ridge (Nakamura et al., 2012).

iv) Fast-spreading ridges with spreading rates exceeding 60 mm/yr such as the East Pacific Rise (Spiess et al., 1980).

Arc-related settings

i) Mature back-arc spreading centers such as the Marianna and Manus Basins, the East Scotia ridge (Martinez and Taylor 2003) and the Lau Basin (Fouquet et al., 1993).

ii) Intra-oceanic arcs such as the Izu-Ogasawara arc (Lizasa et al., 1999) and the Kermadec arc (Monecke et al., 2016).

iii) Transitional arcs such as the Aeolian arc (Monecke et al., 2016) and the Sanghie arc (Butterfield et al., 2010).

iv) Rifted arcs as seen at the Jade site, the largest hydrothermal venting field in the Okinawa (Halbach et al., 1993) and the Iheya North Knoll hydrothermal vent field (Ueno et al., 2003).

v) Continental Margin Volcanic arcs with the only known SMS deposit in this geological setting associated with thinned continental crust is located in the Hellenic Volcanic Arc (HVA), in the Kolumbo arc-volcano, granting it unique status among the other deposits of this type. (Kilias et al., 2013).

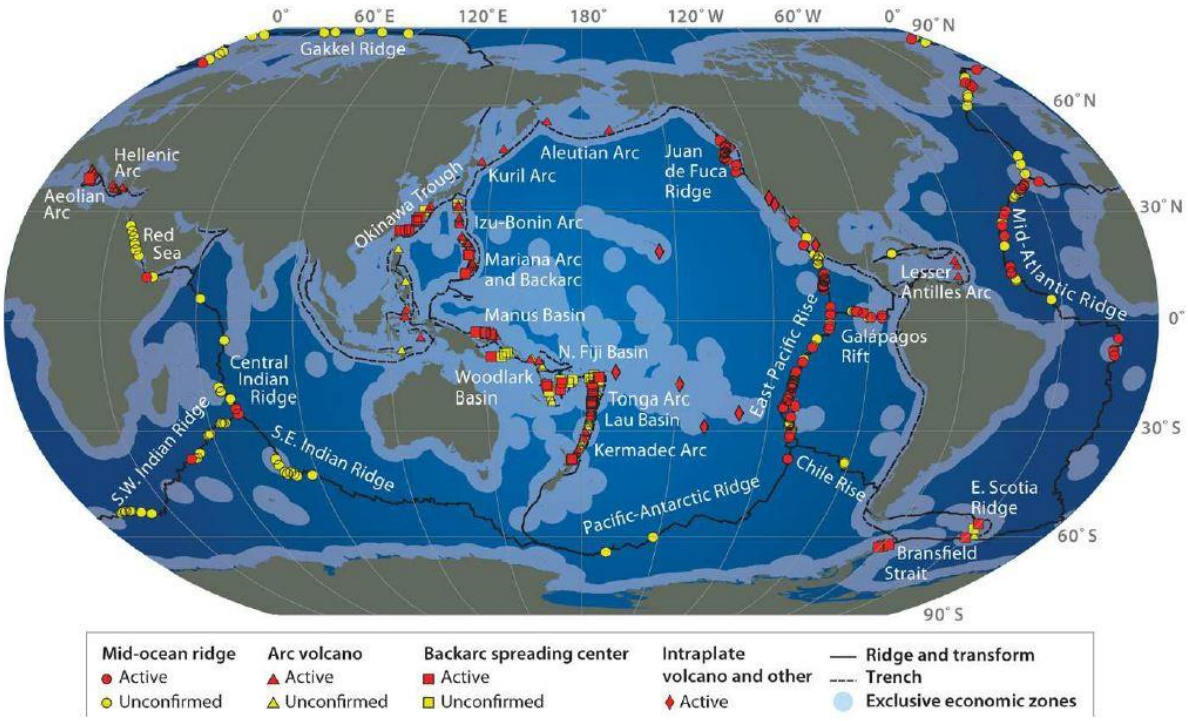

Figure 2: Global distribution of active and inactive hydrothermal vent fields (Hannington 2011).

4.2 Ore forming processes in Seafloor Massive Sulfide deposits

Understanding the way hydrothermal vent fields evolve and the ore forming processes that rule them over is the key to future exploration and exploitation. The diversity and extreme complexity they display make it difficult to decipher how they form (Petersen et al., 2018). However, the most fundamental principles that regulate them are known.

Ore forming processes at Mid-ocean ridges settings

The majority of hydrothermal systems and their related SMS deposits are located at MOR (Mid-ocean ridges) accommodating 65 % of the world's total SMS deposits (Hannington 2011). The composition and the volume of those deposits are controlled by a number of physical and geochemical processes on the oceanic crust. Cold seawater infiltrates permeable oceanic crust through cracks in the seafloor to reach depths the scale of kilometers where it will be heated over 400 °C. Regional tectonics play a major role in these processes as it controls the structure of the crust and creates the paths the seawater will follow through fault zones and cracks. In combination with the underlying heat source, they are the two most important parameters that will affect the extent of the fluid circulation within the crust and therefore the pressure and temperature conditions the seawater will reach. The seawater during this progress will interact with the primary mafic-ultramafic magma and the oceanic crust's rocks. This will cause it to chemically and physically change into a hot caustic fluid that is slightly acidic and chemically reduced (Hannington et al., 2014, Patten et al., 2016, Petersen et al., 2018). The deeper the seawater infiltrates the oceanic crust the more its heated, causing a series of hydrothermal temperature dependent alteration zones from its interaction with the surrounding rocks. At the upper parts of the ocean crust where the Temperature of the fluids is relatively low (50-180 °C) new zeolitic phases will be formed. While at greater depths

its temperature will exceed 300 °C reaching greenschist-amphibolitc condition phases (Alt et al., 2010). As it leaches the surrounding rocks it will get greatly enriched in dissolved metals and sulfur. The lower density it has will force it to rise from the seafloor into the overlying water through hydrothermal vents. Most of the dissolved metals, the hot (~350 °C) hydrothermal fluid carried will mix with the cold seawater and precipitate in sulfide and sulfate phases creating often black and white smokers and diffuser chimneys. These very chimneys are associated with the formation of massive sulfide deposits. In particular, they often reach heights ranging from 40cm to above 40m. As time passes they cool down and collapse forming a mixture of sulfide debris that will eventually turn into sulfide mounts with high metal concentrations on top of the seabed. These metal-rich mounts in combination with the underneath hydrothermally altered host rocks that were enriched by dissolution-reprecipitation mechanisms will form the massive sulfide deposits. While a great number of the metals from the metal-bearing fluids will precipitate as metalliferous sediments on the seabed. The remaining metals that did not precipitate in any form will get carried away by the sea currents (Hannington 2014, Patten 2017 et al., Petersen et al., 2018).

Ore forming processes at arc-related settings

The ore forming processes that take place at arc-related SMS deposits are differ in many aspects than those at Mid-ocean ridges resulting in divergences in their geochemistry and mineralogy (Hannington et al., 2005). These observed differences can be explained by variances in the thickness of the crust, the water depth, the magma compositions and the heat flow regimes. Although a significant amount of SMS deposits is found at back-arc spreading centers and at volcanic arcs, estimated around 22% and 12% respectably, their understanding is not yet complete, as they are not very well studied (Hannington et al., 2011, Petersen et al., 2018). In contrast with the MOR-SMS deposits the source of heat comes from the partial melting of the mantle due to the addition of water as a result of dehydration reactions that occur in the water-rich sediments of the subducted ocean crust at the mantle wedge (Schmidt and Poli, 1998). This process will also trigger the release of other volatiles from the subducting plate and the arc-mantle leading to the oxidation of the arc-magma. The oxidation of magmas causes the destruction of sulfides in the magma source and therefore increases the initial chalcophile elements concentrations (Sun et al., 2004). Extensive degassing of arc-magmas contributes volatiles such as H_2O, HF, HCl, CO_2, SO_2, CO^- etc. to the seawater. This addition can explain the more acidic state (pH 1-3) of the hydrothermal fluids in arc-related settings than those at MOR settings (pH ~4) (Fouquet et al 1993). The leaching of continental crust's rocks in subduction-related environments might be the reason for the enrichment in trace elements such as Bi, Ga, Cd, Ge, Tl and In in comparison with the MOR-related deposits (Hein et al., 2013, Monecke et al., 2016).

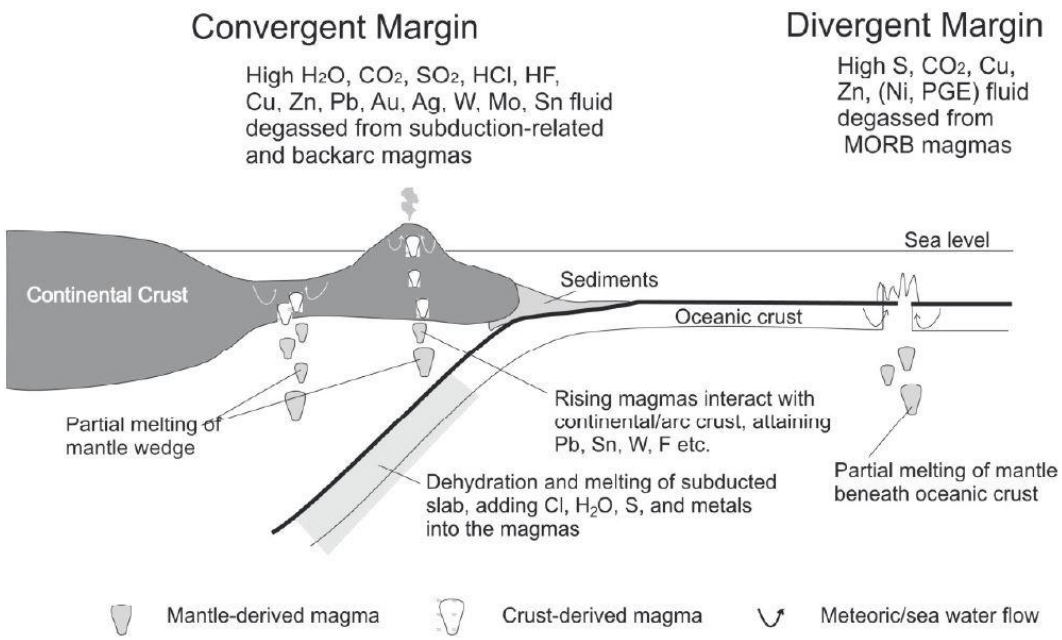

Figure 3: Schematic figure showing the formation of SMS deposits both at Mid-ocean ridges and arc-related geological settings (Yang and Scott 2006).

5. Kolumbo shallow-submarine arc-volcano, Hellenic Volcanic Arc (HVA)

5.1 Geological and geodynamic setting of the HVA

Also known as Aegean Volcanic Arc, HVA developed the last 5 Ma years at the pre-Alpine to Quaternary thinned continental crust of the Hellenic Subduction System (HSS). Its formation is the outcome of the northward subduction of the last remnant of the African plate's oceanic crust beneath the southern edge of the active margin of the European plate's continental crust (Kilias et al., 2013). Observations on Tertiary volcanic rocks of the north Aegean area prove volcanism occurred in late Eocene. The present day active volcanic arc located at the southern margin of the Cycladitic platform and the Cretan back-arc basin indicates a total southward migration of volcanism approximately at 400 km (Bellon et al., 1979; Fytikas et al., 1984; Papanikolaou 1993, Nomikou et al., 2012). The rate of migration is estimated at around 10 km/Myr (Royden and Papanikolaou, 2011, Nomikou et al., 2012).

The HSS is not the typical example of volcanic and hydrothermal activity in convergent settings. What makes it differ from the classic examples of the Pacific region is the fact that the Hellenic Sedimentary Arc (HAS) (Peloponnesus, Crete, Rhodes) is separated from the HVA (Methana, Milos, Santorini, Nisyros) by the Cretan basin (Middle-late Miocene-Quaternary age), which is a back-arc mollasic basin that lies behind the HSA and in front of the HVA (Kilias et al., 2013). This can be explained by the fact that north of Crete island the tectonic settings are characterized by regional extension, while the Hellenic trench and the fore-arc basin of the HSS south of Crete are dominated by compression settings (Le Pichon and Angelier, 1979; Nomikou et al., 2012). This leads to the conclusion that the rate of subduction is greater than the rate of convergent (Burchifiel et al., 2018).

According to geohronological studies of volcanic rocks the modern HVA (Methana, Milos, Santorini, Nisyros, Kos) has been active since early Pliocene until the present day, with intense activity during the Quaternary (Pe-Piper and Piper, 2002). The main centers in which volcanic and hydrothermal activity occurred can be divided into four groups: Methana group at the western edge of the volcanic arc in Western Saronikos Gulf, Milos and Santorini groups in the central part and Nisyros Group at the eastern edge near the Turkish coast (Nomikou et al., 2012). Although, this classification was based on onshore observation, the last forty years of submarine research resulted in the discovery of new volcanic and hydrothermal activity related to the HVA. Until then the only known submarine volcano was that of Kolumbo located several kilometers northeast of Santorini (Fouque 1879, Nomikou et al., 2012). Some of the most significant new discoveries include the Paphsanias submarine volcano (Methana group), three volcanic domes to the east of Antimilos Volcano and hydrothermal activity in southeast Milos in the Milos group, three volcanic domes east of Christiana and a chain of about twenty volcanic domes and craters in the Kolumbo zone northeast of Santorini in the Santorini group and several volcanic domes and a volcanic caldera together with very deep slopes of several volcanic islands in the Nisyros group (Nomikou et al., 2012).

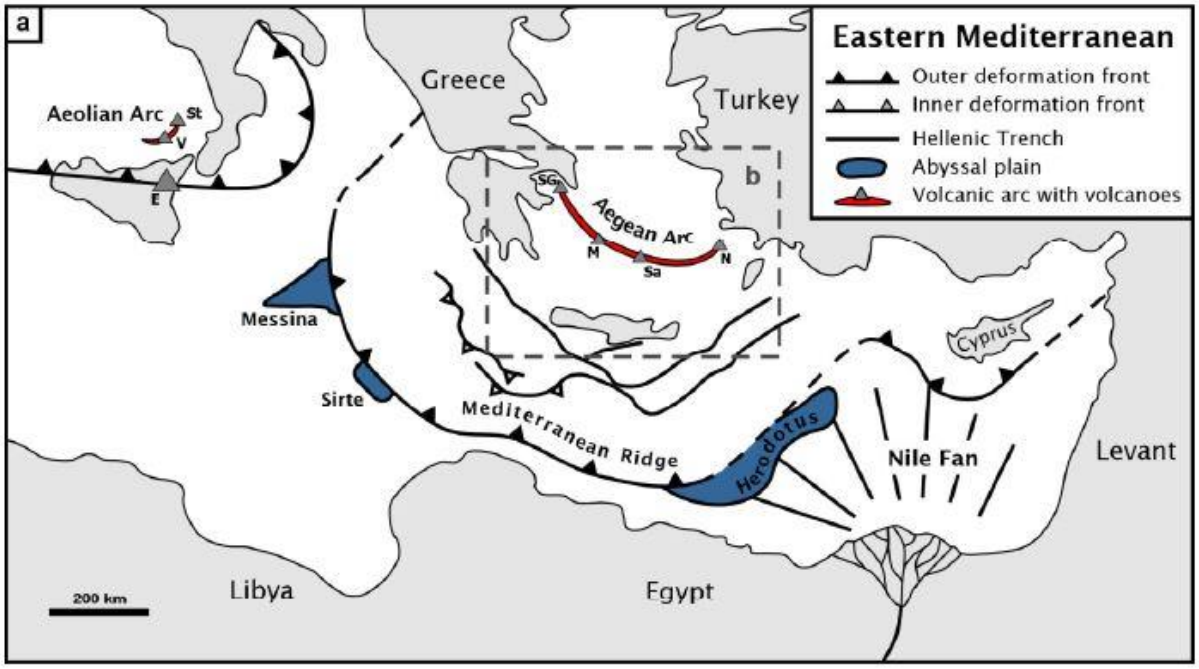

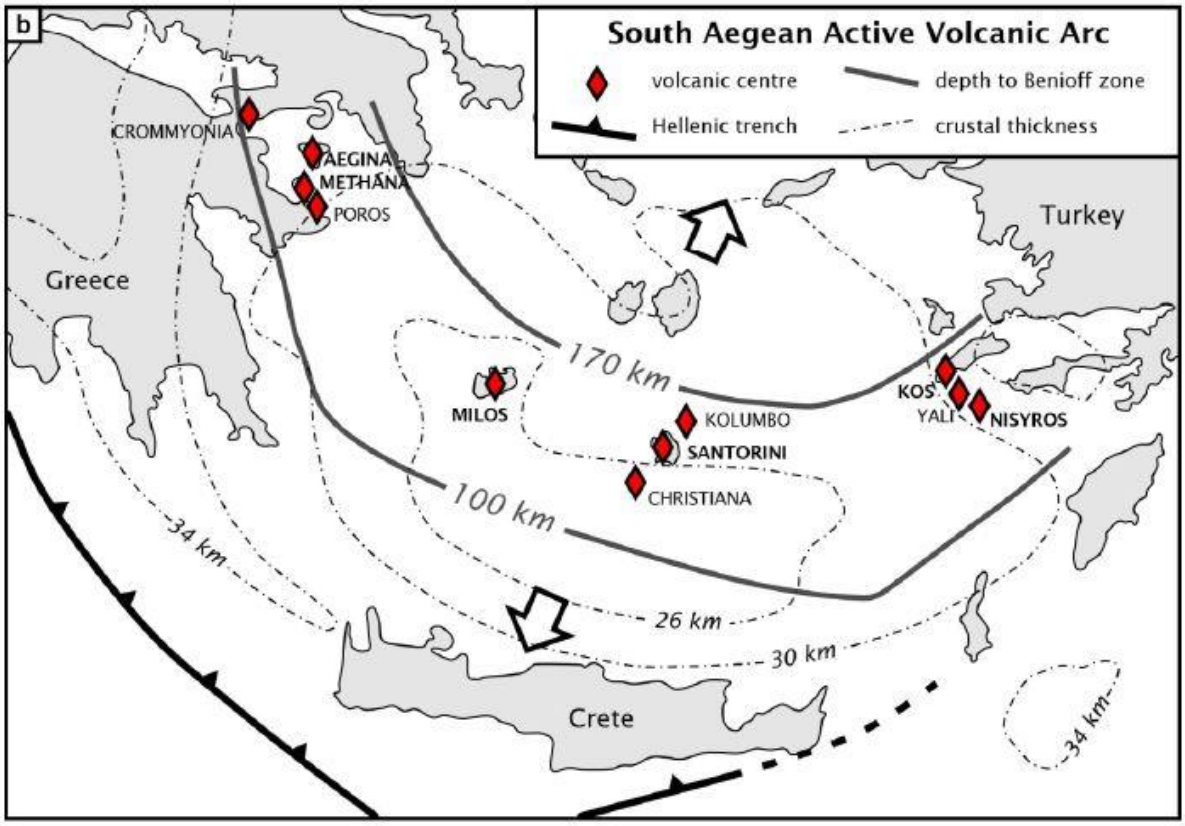

Figure 4: a) Map of the Eastern Mediterranean Sea highlighting the main structural features (modified from Klaver et al., 2015); b) Map of the Aegean arc with the location of the Pliocene-Quaternary volcanic centers. Contours display slab depth and crustal thickness (Ahmad Q. et al., 2018).

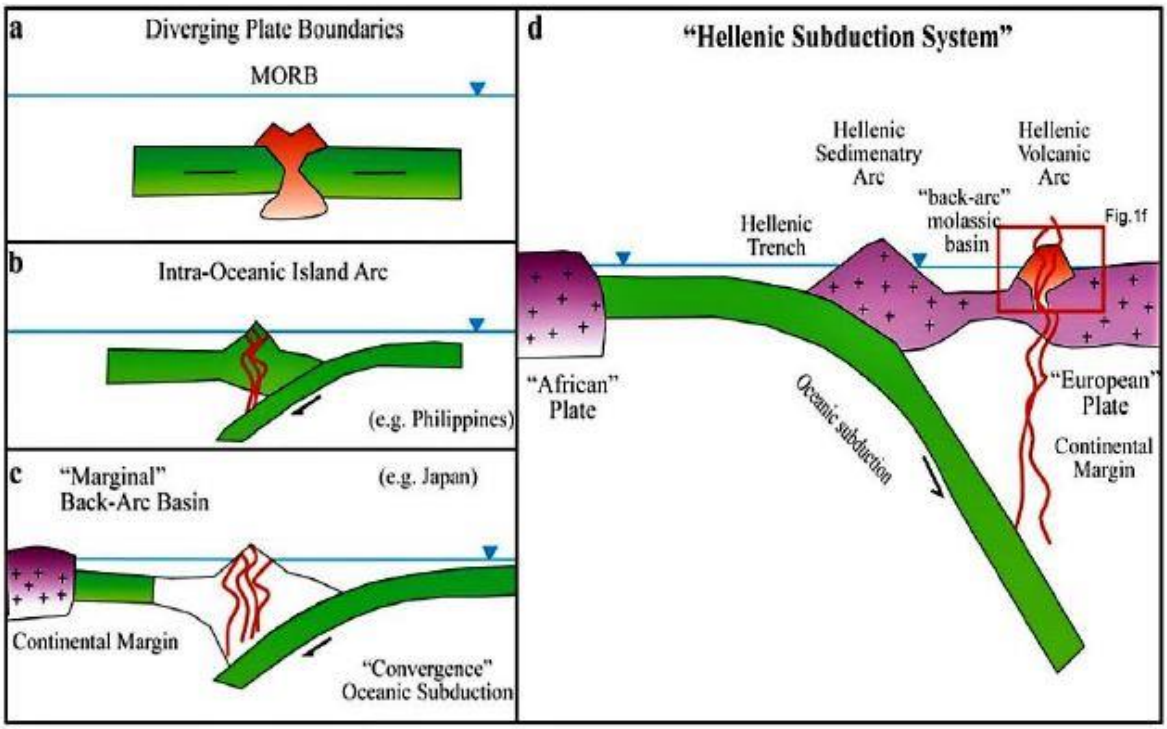

Figure 5: Geodynamic-geological setting of the Santorini-Kolumbo volcanic field. (a–d) Schematic depictions of different geodynamic environments where seafloor hydrothermal vents occur. a) Mid-Ocean Ridges along divergent plates. b) Intra-Oceanic Arcs within convergent boundaries (e.g. Philippines). c) Marginal back-arc basins and island arcs along active continental margins with oceanic subduction (e.g. Japan). d) ''Hellenic Subduction System''. The

''Hellenic Volcanic Arc'', within active continental margin, developed behind the molassic back-arc basin, hosted over thinned continental crust (Kilias et al., 2013).

5.2 The Kolumbo volcano and hydrothermal system

Kolumbo belongs to the Santorini volcanic group that is located at the center of the HVA and its comprised by three distinct volcanic structures along a linear NE-SW direction. Starting from the NE to SW with the Christiana islets, next in the center part with Santorini and ending with Kolumbo. This linear volcano-tectonic structure that is characterized by extreme tectonism, volcanism and hydrothermal activity is known as Christiana-Santorini-Kolumbo (CSK) line as it provides pathways for subduction-generated magmas to reach the surface (Nomikou et al., 2012, Kilias et al., 2013).

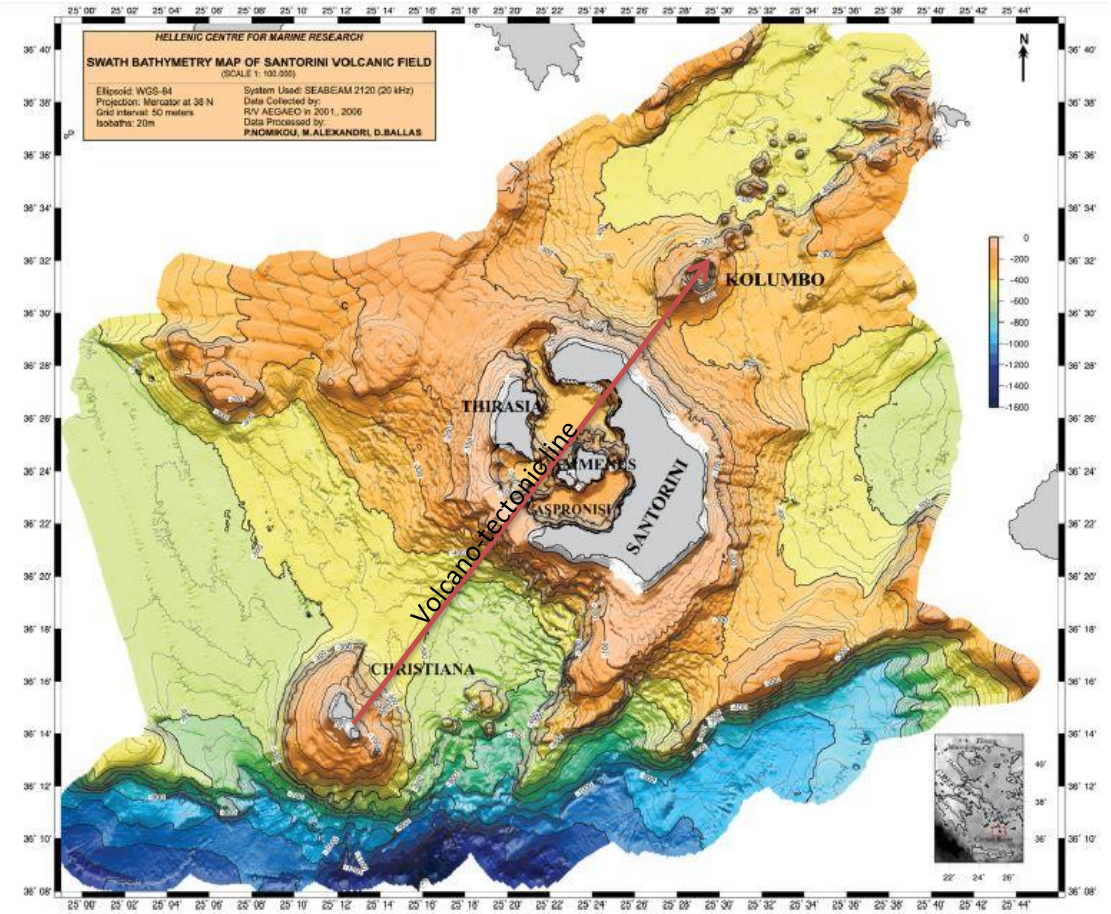

Figure 6: Bathymetric map showing the Christianna-Santorini-Kolumbo volcanic field (CSK) developed along a volcano-tectonic line (red line) (Nomikou et al., 2012).

5.3 Kolumbo morphology and volcanic field

The Kolumbo volcanic field consists of over 20 submarine cones of varying sizes and it extends up to 20 km northeast of the main island of Thera of the Santorini volcanic group. The crater of Kolumbo is thought to be the biggest of this linear assemblage of volcanic cones and its located only 7 km northeast of Thera. Its main cone with a diameter of around 7 km lies at a depth of 505 and it can reach as swallow as 18 m and its crater's width is approximately around 1700 m (Perissoratis, 1993; Sigurdsson et al., 2006, Kilias 2013). The generally trend shows that domes northern of Kolumbo are smaller in size indicating that volcanic activity deceases with increasing distance from the Kolumbo (Nomikou et al., 2012).

Kolumbo formed on the thinned (10-15 km) pre-Alpine continental basement of the Cyclades which is composed of a core of Carboniferous granites (ortho-gneisses) and a sequence of garnet-mica schists as the outcome of the Paleozoic Metamorphic basement cropping out on Ios Island. Over the pre-Alpine basement are found blueschists and overlying nappes both metamorphosed (Late Cretaceous) greenschist, marble, metaophiolite and metagranite, and unmetamorpshosed Mesozoic carbonate and Tertiary flysch (Kilias et al., 2013). During Eocene-Miocene extensional exhumation occurred resulting to outcropping of deep crustal rocks on the Islands of Santorini, Ios and Anafi, neighboring Kolumbo sub-sea volcano, making it possible to study the basement Kolumbo built (Kilias et al., 2013, Mizera and Behrmann, 2016; Peillod et al., 2017). The stratigraphy of the continental crust of the Aegean which Kolumbo intrudes can be assumed based on onshore observations of these neighboring Islands:

Santorini: The metamorphic basement below the volcanic rocks gets exposed in two different localities. At Cape Athinios, where it consists of blueschist facies metapelite with minor metavolcanic rocks and marble and at Saint Profitis Ilias where its characterized by weakly metamorphosed marble and limestone of Triassic age (Pasqualon et al., 2016).

Ios: The general geology of the Island can be described by the occurrence of a mantle gneiss dome in the core which is being overlaid by a marble-schist series. The core shows variably deformed pre-Variscan metagranite augen-gneiss interleaved with Variscan metasedimentay garnet-mica schist (~300 Ma) while the marble-schist series comprises calcite-dolomite, metapelite and metabasalt interpreted as a high-pressure metamorphosed ophiolitic and carbonate platform mélange (Mizera and Behrmann, 2016).

Anafi: There are four main tectonically stacked lithological units at Anafi Island. From the base of the structure to the upper parts they are distinguished as: i) an Eocene flysch formation, ii) a MORB-like Paleocene greenschist series, iii) a tectonic mélange of HT-LP formed of amphibolite, marble, granite and serpentinised ultramafic rocks and iv) late Miocene to Pleistocene molasse-like sedimentary rocks (Martha et al., 2016, Patten et al., 2018).

Kolumbo's crater walls are composed of stratified pumiceous deposits at a water depth of 270-250 m that continues to 150 m above, which the deposits are obscured by loose talus and bacterial overgrowths (Carey et al., 2011; Kilias et al., 2013). Petrological analyses of those pumices show that they are rich-K rhyolites with a high pre-eruption volatile content of 6-7%. The pre-eruptive storage of the magma is considered to be at 5 km depths and reaching temperatures as high as 750 °C (Cantner et al., 2011).

After a year of strong seismic activity at 1650 AD, Kolumbo erupted, causing over 70 human casualties from toxic gas in the near Island of Santorini. It also generated a tsunami wave that caused significant damage to the east coast of Thera. Until today this remains the biggest explosive known event of the volcano (Fouque, 1879, Nomikou et al., 2012). This event was followed by a four month period of subaerial and submarine hydrothermal activity according to Cantner (et al., 2014). The today's oval-shaped crater of Kolumbo is the product of at least four eruptive cycles, as evidence from seismic profiles suggested (Hóbscher et al., 2015). The base of the volcanic cone is composed of layered massive lavas, while the upper part is represented by the tephra deposits produced during the 1650 AD eruptive phase (Nomikou et al., 2013, Cantner et al., 2014). Although Kolumbo is very close (7 km)

to the main volcano of Santorini it has its own different magmatic chamber. Geochemical and petrological studies further support this claim showing differences between the two volcanos. More specifically, volcanic rocks from Santorini show more anhydrous mineral phases, in comparison with the biotite and amphibole phases that occur at Kolumbo's samples. Moreover, the strong geochemical signature of amphibole fractionation and the assimilation of lower crustal basement in the petrogenesis of the Kolumbo magmas evidence that Kolumbo and Santorini underwent different crustal differentiation histories and that their crustal magmatic systems are distinc. Lastly the high Nb/Yb (>3) and low **206**Pb/**204**Pb (<18.82) ratios in the Kolumbo rocks show that it derived from a more enriched mantle source in contrast with Santorini that do not display the same ratios (Klaver et al., 2016).

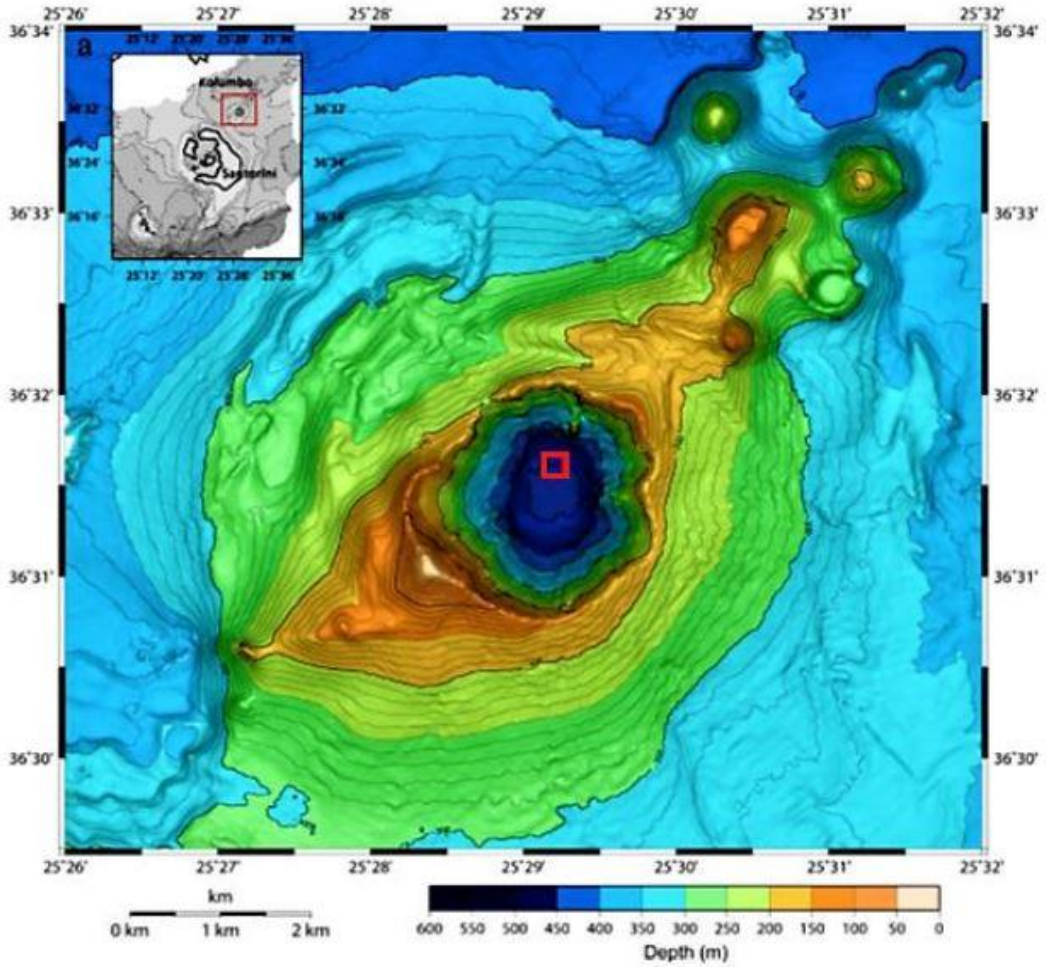

Figure 7: Detailed bathymetric map of Kolumbo volcano (modified after Nomikou et al., 2012). (The red square represents the area of which a detailed bathymetric map of Kolumbo hydrothermal vent field is given in Figure. 14.1).

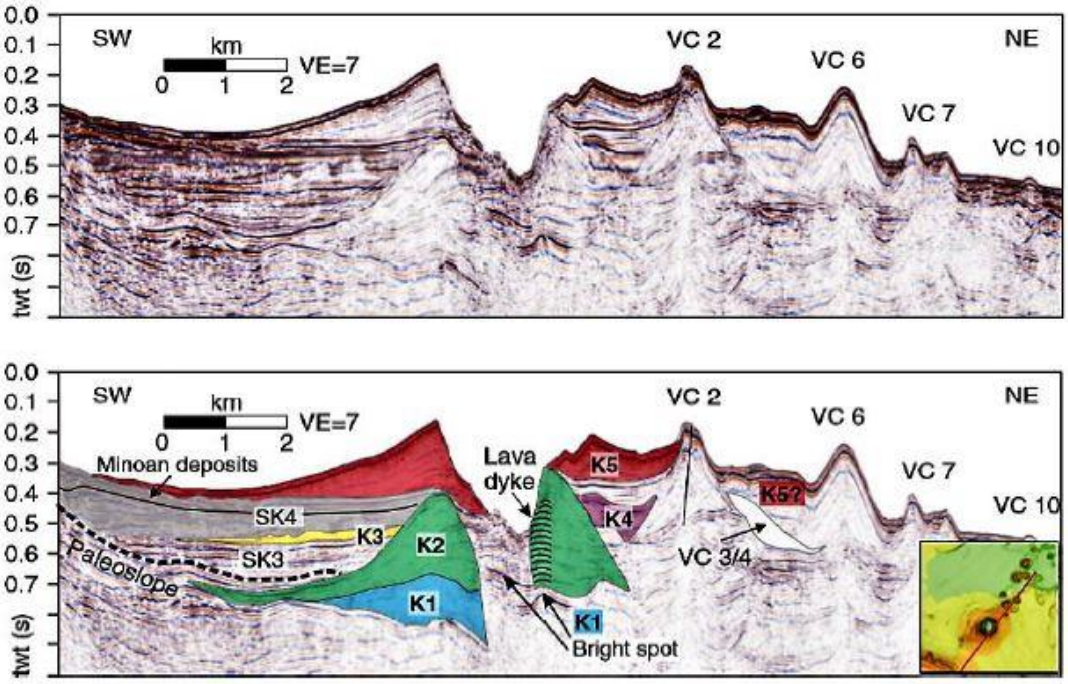

Figure 8: SW-NE striking multi-channel reflection seismic profile across Kolumbo. The upper part displays seismic data whereas lower the part displays data interpretation. Grey shaded area marks pyroclastic flows or mass transport deposit. K1-K5: the five circular stratigraphic units labeled bottom-up. SK3 and SK4 refer to intercalated units. VC: Volcanic Cone. VC numbers according to Nomikou et al. (2013), (Hübscher et al., 2015).

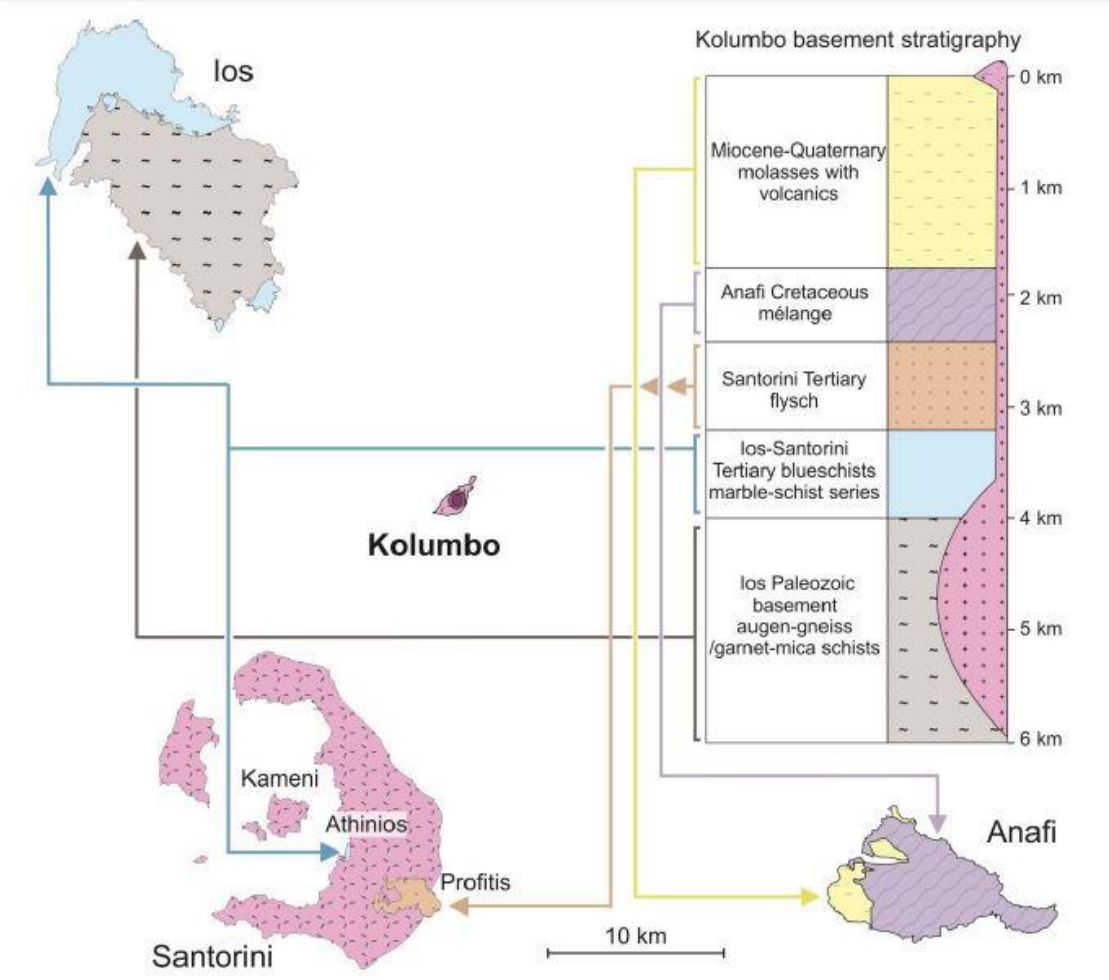

Figure 9: Regional geology and basement stratigraphy of the Kolumbo volcano (DFG project 2018, Patten et al., 2018).

5.4 Kolumbo Hydrothermal Vent Field (KHVF)

Kolumbo's extensive diffuse-flow hydrothermal vent field was first identified at 2006 via Remotely Operated Vehicle (ROV) explorations, at depths of between 492 and 504 m (Sigurdsson et al., 2006). Sediments only a few cm in thickness are covering the entire crater floor, consisting of Fe-encrusted flocculent microbial mats and as well as amorphous Fe-oxyhydroxide precipitates. The high Fe-content gives this smooth sediment an orange to brown color (Carey et al., 2010, Kilias et al., 2013) and measurements in Temperature show a small variation between 16.2 °C and 17 °C. Beneath the Fe-microbial mats, occur small pockmark-like craters that discharge clear, low temperature fluids (≤70 °C) alongside CO_2 gas bubbles. This hydrothermal activity might be supporting microbiological productivity on Kolumbo's crater may be related to the Fe-mat formation (Edwards et al., 2011). At greater depths (~490m) on the base of the northern wall streaks of white microbial mats appear, most likely as the result colonization of low-temperature probably dense-fluid seeps. These microbial mats contribute orange-brown and white particles to the seawater column making it appear strongly clouded at depths > 250m (Kilias et al., 2013). Active and inactive sulfide-sulfate structures in the form of vertical spires and pinnacles, mounds and flanges emerge through the microbial mats (Nomikou et al., 2012). These vents are formed along NE-SW trend, sub-parallel to the CSK line. One of the most characteristic examples of diffuser flow is the Politeia Vent Complex. It consists of short (<3 m tall), slender, intermediate-temperature diffusely-venting, isolated and/or merged, sulfide-sulfate spires or diffusers covering a total area of 5x5 m (Fouquet 1993, Tivey et al., 2007, Kilias et al., 2013). These hydrothermal spires tend to discharge clear shimmering fluids, from which sulfide minerals have precipitated prior to discharge (Hannington et al., 2005). They are similar to the shallow water-boiling vents observed at the Tonga arc (Stoffers et al., 2006) and the Mid-Atlantic Ridge near the region of Iceland (Hannington et al., 2001). They differ with the classic black-smokers in the way that they do not display a typical axial conduit and also lack the beehive structure (Hannington et al., 2005). Microbial biofilms of grayish color are surrounding the exterior part of the vents (Kilias et al., 2013). Champagne Vent Complex and the Diffuser II Vent Complex are located at the center of KHF. They consist of smooth-sided sulfide-sulfate mounds without spire structures and are covered by orange to brown Fe-mats. Through cracks and small holes on the base and their side bubble streams mainly of CO_2 are emitted. The CO_2 gas will dissolute, creating that way a stable-stratified CO_2 rich-water inside Kolumbo's crater and the accumulation of acidic water with a pH value of around 5 for approximately 10-15 m above the vents (Carey et al., 2013, Kilias et al., 2013). The biggest vent in height reaches 4 m and was observed at the Poet's Candle at the northern crater slope and did not display clear evidence of shimmering fluids. Measurements of the fluids temperature show a max value of 210 °C (Kilias et al., 2013). During ROV explorations two massive sulfide spires and four sulfate and sulfide mounds from the Politeia Vent Complex was collected along with three mounds from Champagne and one from the Diffuser II complex.

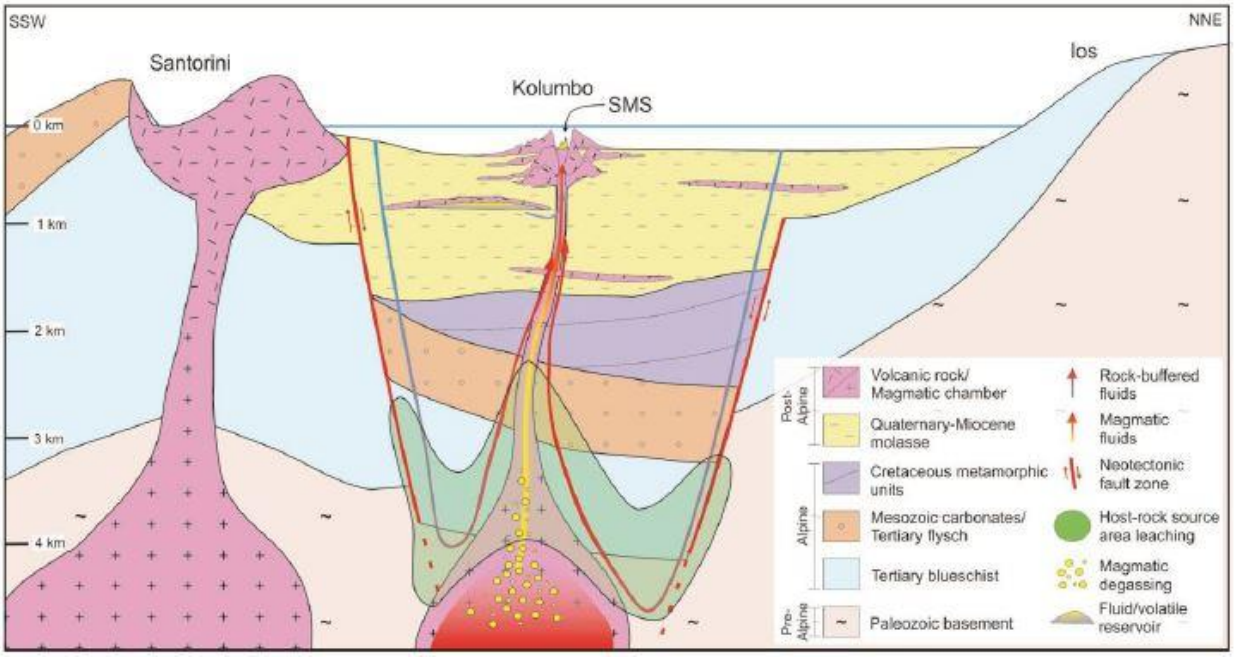

Figure 10: Crust section below the Kolumbo volcano with the possible source areas for the metal trapped in the Kolumbo polymetallic SMS. The metals can either be mobilized during magmatic degassing or from the crust during circulation of seawater-derived hydrothermal fluids. (Modified from Kilias et al. 2013, Patten et al., 2018).

5.5 Boiling zone at the Kolumbo seafloor

The KHVF formation and evolution is strongly controlled by a boiling zone (Kilias et al., 2013). Kolumbo formed on a shallow-water depth and is characterized by an epithermal-style geochemical enrichment with high and wide ranges in gold-to-base-metal ratios calculated for the different vent complexes. The CO_2-rich hydrothermal fluid they emit reaches low to intermediate temperatures approximately 220 °C on the seawater boiling curve and the hydrothermal spires are usually barite dominated. All of these observations further provide evidence that Kolumbo indeed has a boiling zone (Tivey, 2007; Monecke et al., 2014, Hannington et al., 2005).

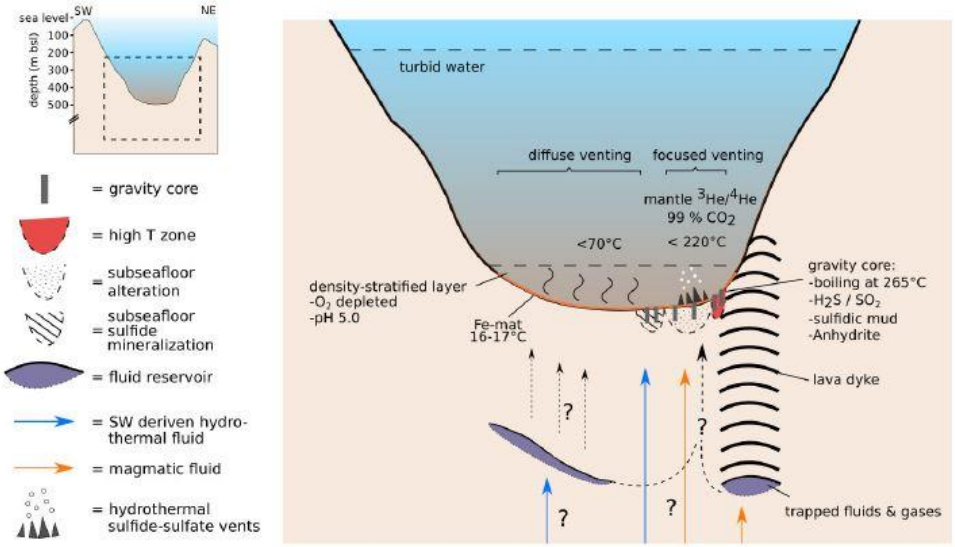

Figure 11: Schematic cross section of the Kolumbo crater showing distinct features of the Kolumbo Hydrothermal (Carey et al., (2013), Kilias et al., (2013), Hóbscher et al., (2015), Rizzo et al., (2016); Hannington (2017), Patten et al., 2018).

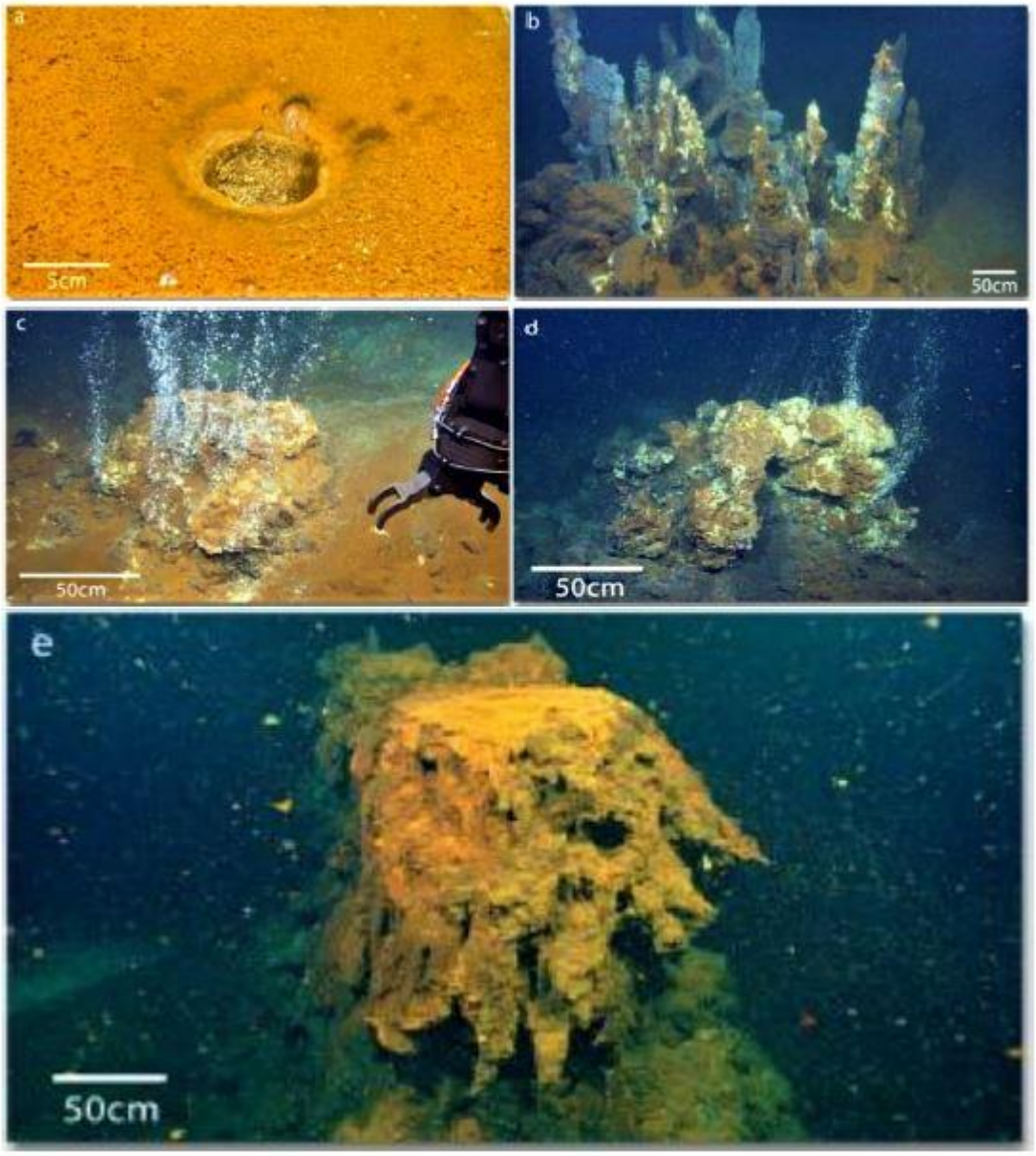

Figure 12: Submarine photographs taken by co-Chief Scientists Steven Carey, Katherine Croff Bell, Paraskevi Nomikou onboard E/V Nautilus during oceanographic cruises NA007-NA014. a) Small pockmark–like crater discharging low-temperature (70°C) fluids. b) Politeia Vent Complex ("Politeia"): Field of multiple inactive and active sulfide/sulfate, spires up to 2 m high on top of a hydrothermal mound with spire fragments draped by Fe-bearing bacterial mats. Clear fluids vent from active spires (not visible). c) Diffuser II Vent Complex ("Diffuser"): Vent with bacterial covering and gas bubbling. d) Champagne Vent Complex ("Champagne"): Active high-temperature (220°C) vent discharging both gases (>99 % CO2) and fluids. e) Poet's Candle: The largest observed (height ~ 4m) inactive vent with bacterial covering (Kilias et al., 2013).

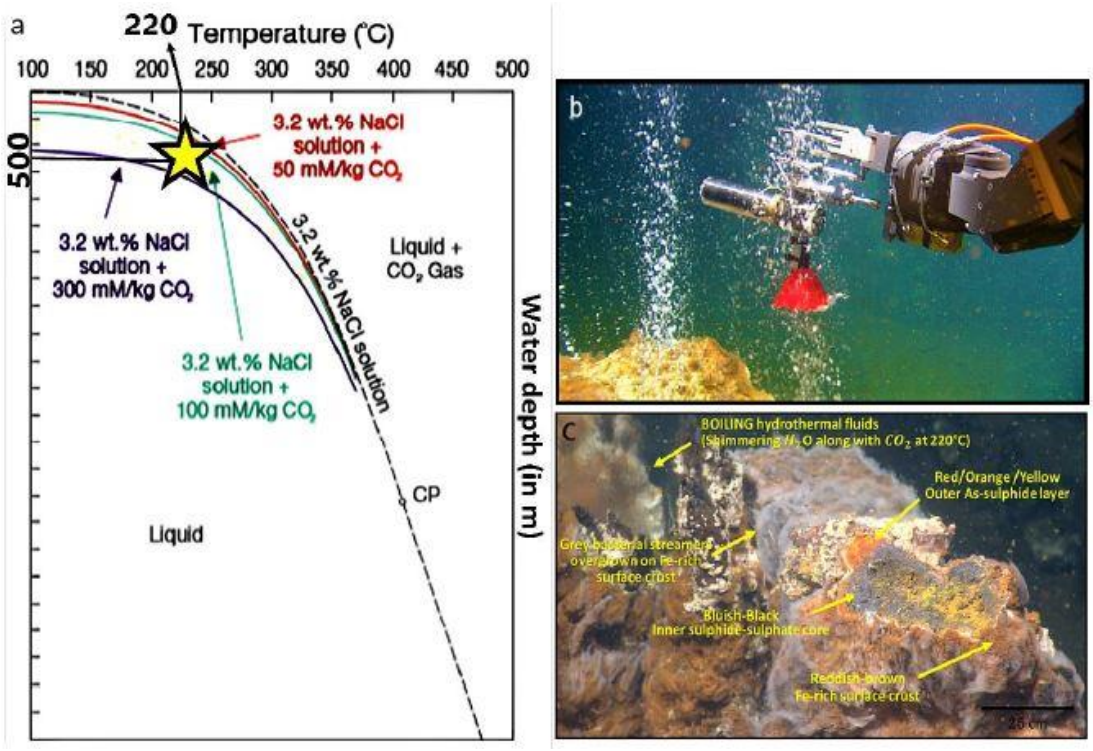

Figure 13: a) Seawater boiling curve containing 0 mM/kg CO2 (dashed line) compared to boiling curves containing 50, 100, and 300 mM/kg CO2 in a 3.2 wt% NaCl solution. The plot shows that the physical behavior of hydrothermal fluids is deeply affected by the gas content and that increasing CO2 concentrations shift the two-phase boundary toward higher pressures (or deeper water depths) (Monecke et al., 2014). Vent temperature (220°C) of Kolumbo shallow (500m) hydrothermal system (yellow star) suggests that phase separation occurs in this hydrothermal system. b) Seafloor degassing of boiling nearly pure CO2 fluids in Kolumbo hydrothermal vent field. c) Active high-temperature (220°C) vents discharging shimmering H2O along with CO2 (Zegkinoglou 2020).

5.5 Enrichment of metals and metalloids in Kolumbo

The unique geological settings Kolumbo is built in, is imprinted in its geochemistry as well. The hydrothermal chimneys that are found in its crater consist of an inner sulfide-sulfate core (barite, pyrite, galena, sphalerite, marcasite, chalcopyrite, Sb-Pb sulfosalts, stibnite) which is mantled by a thin outer layer of As-sulfides which in turn is covered by a by ferrihydrite-like Fe-(oxyhydro-)oxide crust (Kilias et al., 2013). Studies based on the textures of pyrite and sphalerite revealed that fluid-mediated coupled-dissolution repricipitation reactions are controlling the concentration of metals and metalloids indicating a complex evolution of hydrothermal fluid circulation. This might led to zone refinement and upgrading processes of certain metals content. More precisely, Kolumbo is characterized by low base metal concentrations such as Zn, Cu, Pb but shows an enrichment in Au, As, Sb, Tl, Hg content. Bulk analyses revealed an average grade of 9ppm Au with a max value of 32 ppm in samples from the chimneys, while the values of the other metals and metalloids are the follow; Cu (av. 1640 ppm, max. 3761 ppm), Pb (av. 3.5 wt. %, max. 6.71 wt.%), Sb (av. 0.83 wt.%, max. 2.24 wt.%), Ag (av. 871 ppm, max. 1910ppm), Hg (av. 397 ppm, max. 1070 ppm), Tl (av. 389 ppm, max. 868 ppm) (Kilias et al., 2013). Kolumbo mineralization style is classified as an auriferous SMS deposit as the grade of Au to base metal ratio over unity (Au/Zn+Cu+Pb) is calculated to 1.9 (Mercier-Langevin et al., 2011).

6. Scope of thesis

The current thesis consist an introduction to the world of the hydrothermal submarine ore deposits and a better understanding of the basic principles of the ore formation processes for a graduate level student. In particular, it aims to explain the distribution of barite's diverse textural growth inside the hydrothermal chimneys and its relationship with the other sulfide minerals. Barite is usually the first mineral that precipitates in these hydrothermal systems, therefore it's the mineral that controls and constructs the formation of the chimney. So the geochemical composition, the metals participation and the volume of the deposit are all dependent on how well and at what extent barite precipitates. Also because of barite's early entry in the system along its great preservation abilities, make it a great recorder for the chemical and physical attributes of the primary hydrothermal fluids. Although barite is a key component in the development of the chimneys little is known about it, as not a lot of studies focuses on that matter. In the Kolumbo hydrothermal vent field, barite is the main sulfate mineral compromising the matrix among the different sulfide-sulfate phases. So a very detailed petrographic study of the barite textures deemed necessary. The main objectives of this thesis can be summarized as:

- The description of the various barite textures and where they take place both in the paragenetic sequence and spatial.
- The role of barite in the development of the hydrothermal chimneys.

7. Materials and Methods

The samples for this current thesis were collected during oceanographic expeditions. The first one was conducted in September 2011 during the oceanographic expedition with cruise number NA014 ("Hellenic Volcanic Arc and Cretan Basin") of the "New Frontiers in Ocean Exploration 2011" project and Principal Investigator was Robert Ballard (Institute for Exploration and Ocean Exploration Trust, University of Rhode Island URI, USA)(State File No. F2011-049, 2012), while the Chief scientists were Katherine Croff Bell (Ocean Exploration Trust, University of Rhode Island (URI) USA) and Paraskevi Nomikou (National and Kapodistrian University of Athens, Dept. of Geology and Geoenvironment, Greece).
The E/V Nautilus is a 64-meter research vessel, owned and operated by the Institute for Exploration, Ocean Exploration Trust and University of Rhode Island (URI) Center for Ocean Exploration and is equipped with the remotely operated vehicles (ROVs) Hercules and Argus. The Hercules and Argus system is a state-of-the-art deep sea robotic laboratory capable of exploring depths up to 4,000 meters and is equipped with a dedicated suite of cameras and sensors that receive electrical power from the surface through a fiber-optic cable, which also transmits data and video. The ROV Hercules is equipped with a number of tools, including a suction sampler, sampling boxes, and sediment coring equipment, a suite of mapping instruments that enable detailed visual and acoustic sea-floor surveys.
The second one was conducted from 2 to 10 September 2013, and the samples were collected on the 3rd of September 2013 during the EU-funded oceanographic expedition "2-BIOTECH SAMPLING EVENT" of the "SeaBioTech" EU-FP7 project (Grant Number 311932) {http://spider.science.strath.ac.uk/seabiotech/index.php}. The Chief scientist of the expedition was Dr Paraskevi Polymenakou (Hellenic Centre Marine Research (HCMR)). The survey was conducted with the (ROV) Max Rover onboard oceanographic vessel Aegaeo of the HCMR.

7.1 Sampling

A detailed description of the sampling campaign alongside the methods for the first oceanographic expedition can be found in in Institute for Exploration, Ocean Exploration Trust and URI Center for Ocean Exploration-State File No. F2011-049 (2012) and also at Kilias et al. (2013) and as for the second expedition, in HCMR's "SeaBioTech Report 2013". The location of the recovered samples of hydrothermal vents that were examined in this present thesis is shown in figures 13.1, 13.2, 13.3, 13.4, 13.,5 respectively.

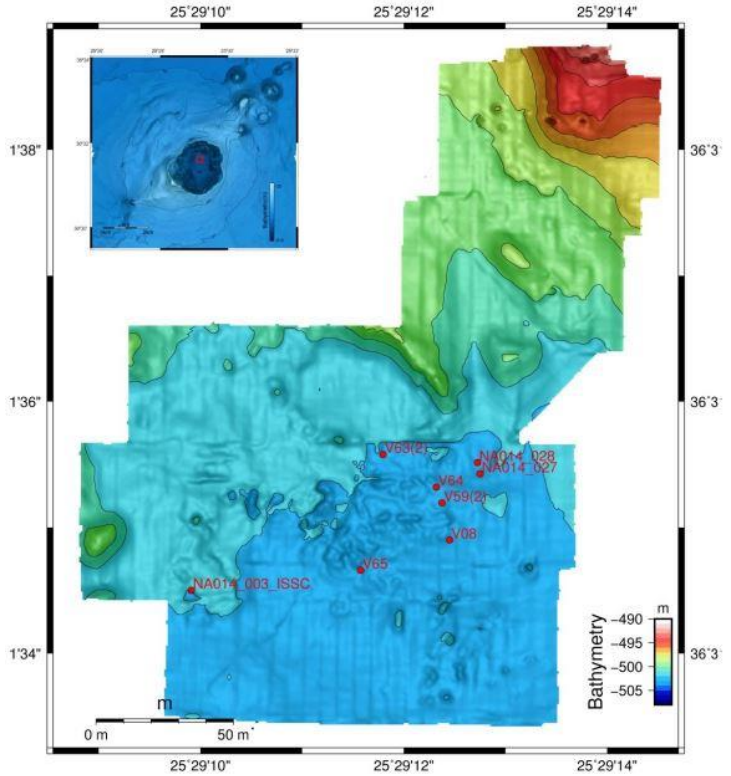

Figure 14.1: Detailed bathymetric map of Kolumbo hydrothermal vents with the location of the samples studied (modified from Nomikou et al., 2013; Kilias et al., 2013)

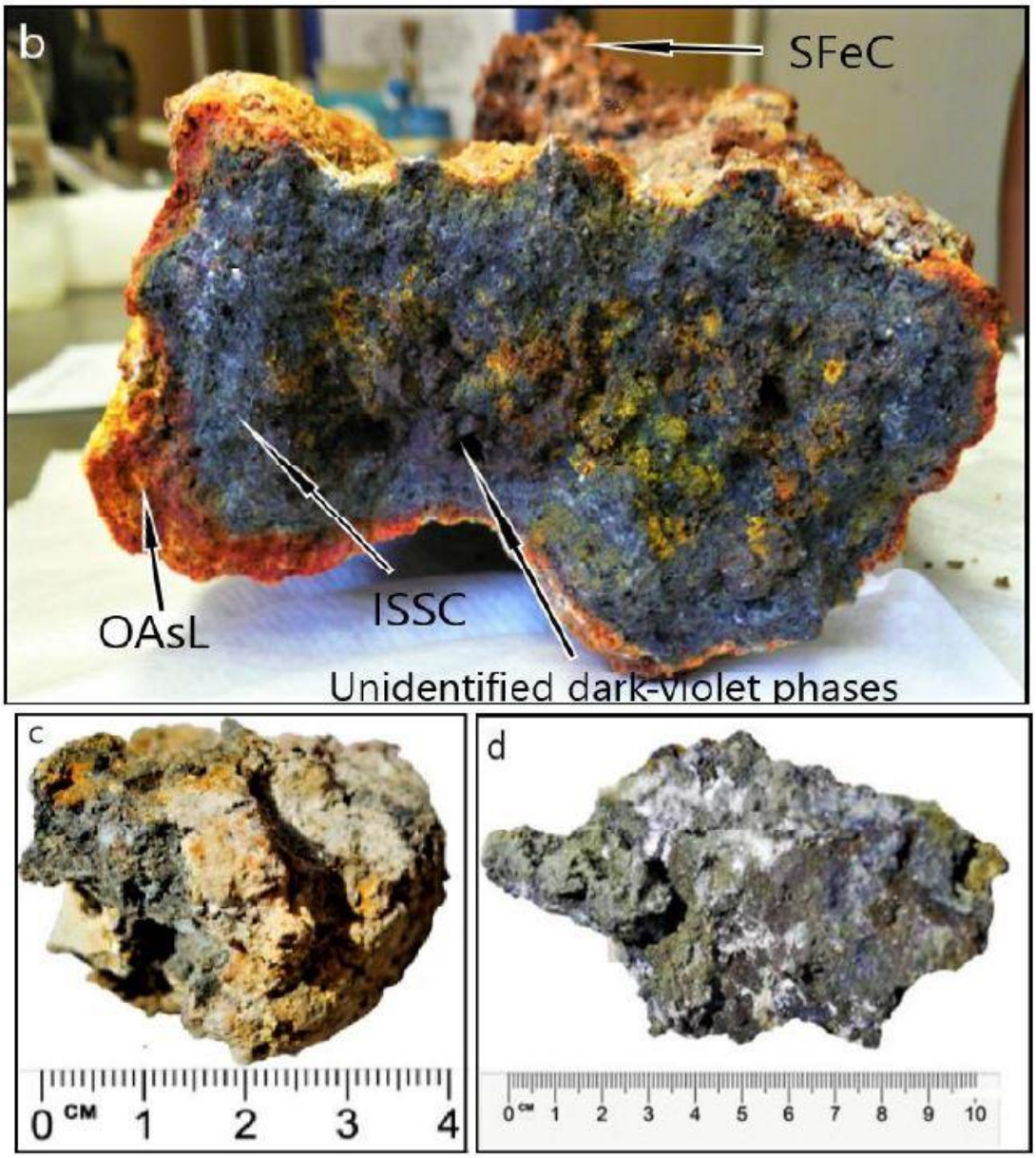
b
SFeC
OAsL
ISSC
Unidentified dark-violet phases
c
0 CM 1 2 3 4
d
0 CM 1 2 3 4 5 6 7 8 9 10

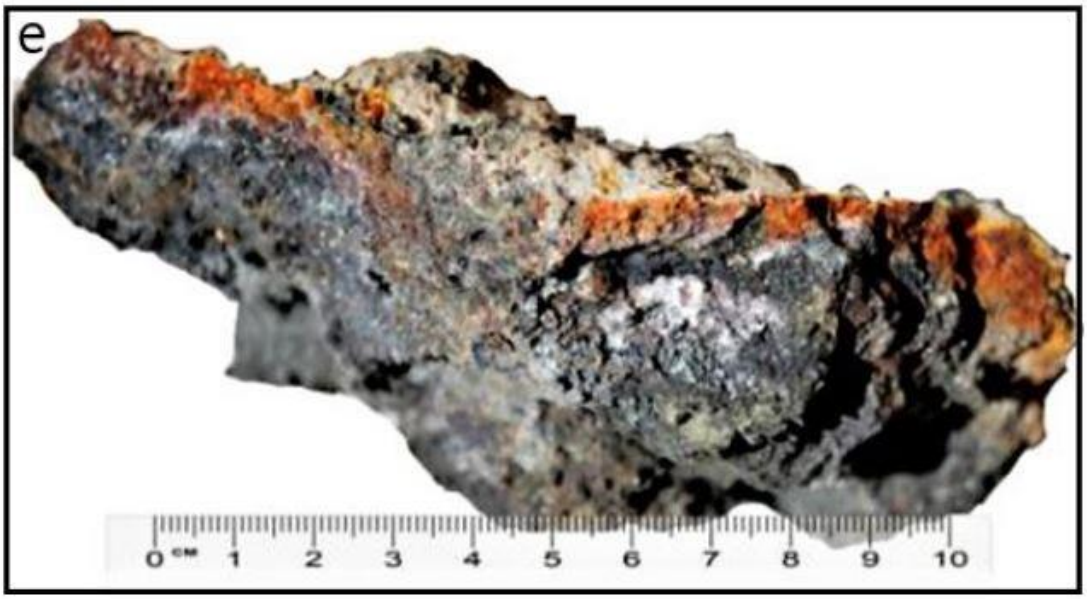

Figure 14.2: Ex-situ photographs of solid hydrothermal chimney samples from cruise ‘‘NA014’’. a) Sulfide-sulfate spire sample NA014-003 (Politeia Vent Complex). b) The base of sample NA014-003 revealing four textural zones: i) ’’Inner sulfide-sulfate core’’ (ISSC), ii) thin orange-yellow ‘‘outer As-sulfide layer’’ (OAsL), iii) ‘‘surface Fe-rich crust’’ (SFeC) and iv) dark violet metallic aggregates of unidentified PXRD-amorphous Sb-Zn-S phases c) NA014-027 (Champagne vent complex), d-e) sample NA014-028 (Champagne vent complex).

Figure 14.3: Ex-situ photographs of solid hydrothermal chimney samples collected from the “SeaBioTech” EU-FP7 project. a) Broken off and/or sectioned parts (SB-3-D, SB-3-E, SB-3-F) of sample SB-3 with marked bottom-up growth orientation. Samples SB-3-D and SB-3-E represent the ISSC zone and sample SB-3-F is the top part of this hydrothermal chimney. The brown exterior surface of the samples represents the OAsL zone. b) Sectioned chimney sample SB-7-A representing the ISSC zone. c,d) Ex-situ photographs of the hydrothermal spire sample SB-9 showing the whole sample which is covered by the OAsL zone (c) while its interior represents the ISSC zone; (d) the massive sulfide (ISSC)-dominated basal part of the spire.

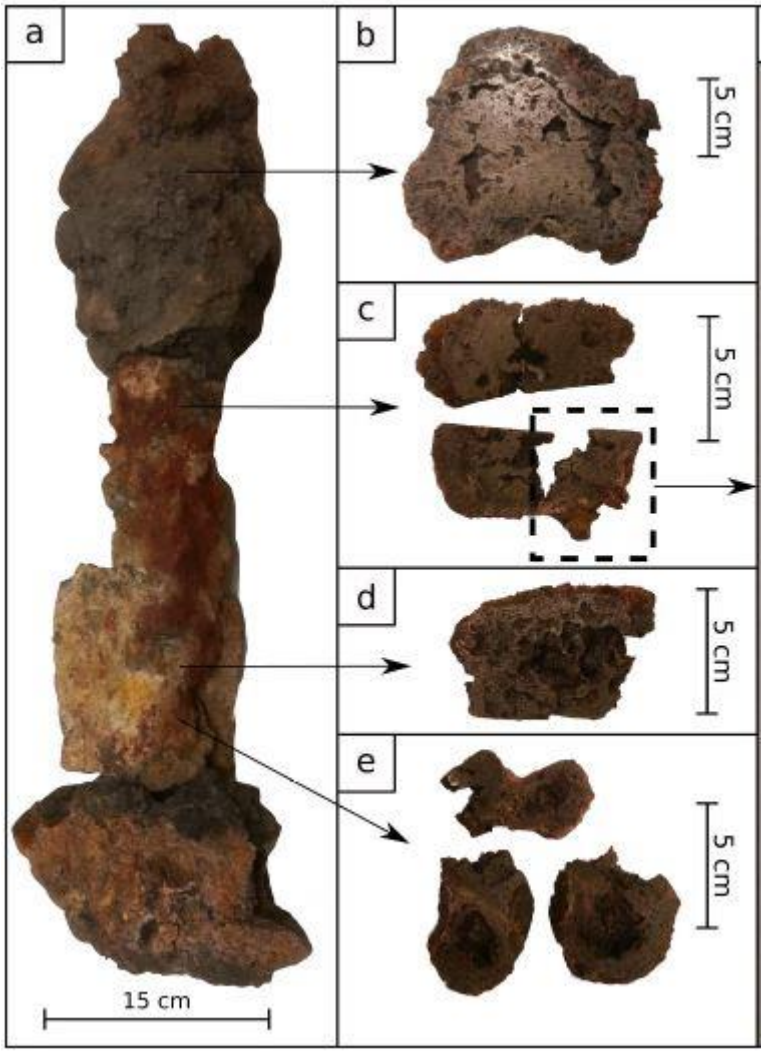

Figure 15: Ex-situ photograph of hydrothermal chimney sample divided into four sections for petrographic studies.

7.2 Samples preparation

The studied samples had already been prepared and used for previous M.Sc. theses by former M.Sc. students Maria Gousgouni (Gousgouni, 2014), Maria-Despoina Chrysafeni (Chrysafeni, 2016), Evangelia Zygouri (Zygouri, 2017) and Nikolaos Zegkinoglou (Zegkinoglou, 2020). A total of 28 polished thin sections and 17 polished blocks were made at Institute of Geology and Mineral Exploration (IGME), Attiki, Greece. In addition, seven (7) double-polished thick-thin sections were prepared at Karlsruhe Institute of Technology (KIT). The first five of them are from a hydrothermal chimney, while the other two are from a sulfate mound from the same. All the samples were examined for mineralogical characterization under both reflected and transmitted light. The samples were extremely brittle making impossible to obtain entire sections or blocks of the outer yellow-orange layers of the OAsL zone, so in this study only small parts of the OAsL zone were examined.

7.3 Analytical technics

The analytical technics uses for this present research are listed as below:

- Optical Microscopy.
- Scanning Electron Microscopy (SEM).
- Energy Dispersive Spectroscopy (EDS) for major and minor element analysis.

7.3.1 Optical Microscopy

Mineralogy as well as textural variation of the mineral assemblages from twenty-eight (28) polished thin sections seventeen (17) polished blocks and seven (7) double-polished thick-thin sections have been observed using Optical Microscope in both transmitted and reflected light at the Department of Geology and Geoenvironment, National and Kapodistrian University of Athens.

7.3.2 Scanning Electron Microscopy coupled with Energy Dispersive Spectroscopy

A total of three polished thin blocks and two polished thin sections were selected for SEM analyses in order to determine the geochemical composition of barite crystals as well as for better understanding the variety of their textures. All the analyses were carried at the Department of Geology and Geoenvironment National and Kapodistrian University of Athens.

8 Results

8.1 Mineral assemblages-paragenesis

The total of the prepared polished thin sections and blocks alongside the wafers were examined explicitly, in order to carefully describe the mineralogical texture variations of the different sulfides-sulfates phases, but mainly focusing on barite. These petrographic studies made it possible to understand the paragenetic sequence and help decipher the hydrothermal chimneys grow.

The studied diffuser-style chimneys are dominated by a conduits network, from which the hydrothermal fluid passed and they are compromising from three different zones. The Inner Sulfide-Sulfate Core (ISSC) consisting of barite, pyrite, marcasite, sphalerite, galena, Pb-Sb sulfosalts, minor anglesite and minor chalcopyrite. The Outer Arsenic Layer (OAsL) covers ISSC and it consists of barite, pyrite, sphalerite, galena, Pb-Sb sulfosalts, stibnite, As-Pb-Sb sulfosalts and amorphous realgar- and orpiment-like As-rich sulfides. In turn, OAsL is covered by a gelatinous orange to brown Surface of Fe-rich Microbial Crust (SFeMC) with the most typical minerals being amorphous Fe-(hydrated)-oxyhydroxides (Kilias et al., 2013).

This study's main objective is to identify and describe in detail the different petrographic types of barite and their distribution respectably inside the chimneys. The majority of the samples come from the ISSC and the OAsL, as samples from the SFeMC couldn't be obtained as they were very brittle.

8.2.1 Barite in the ISSC

Barite stage

Optical microscopy observations have revealed that the dominant sulfate mineral is barite. Barite is the only mineral present in all of the chimneys zones from the first stages of mineralization until the late stages and it comprises the matrix among the different sulfide-sulfate phases. At this point it's worth mentioning the minor presence of Anhydrite, as it plays a major role in the precipitation of barite. The small amount of Anhydrite can explain the barite domination in the system, as they have reversed solubility, meaning that the primary Anhydrite that precipitated dissolute, making it possible for large quantities of barite to form. Barite exhibits a great variety of textures, showing changes in the physico-chemical conditions of the fluids, during the chimney grow. In the ISSC barite, is associated as intergrowths with pyrite, sphalerite, Pb-Sb-sulfosalts and rarely galena and marcasite. Petrographic study of sulfate mounds near hydrothermal chimneys has revealed that the very first Barite generation consists of large (mm) barite laths and blades aggregates and rarer recrystallized mosaic structures. Big open-space, usually singular, barite blades and laths are thought to be part of the second generation of barite mineralization and they comprise the matrix, making it possible for the other sulfides to precipitate around them. Another generation of barite occurs in the ISSC that is relatively smaller in size and usually forms aggregates, most commonly in the form of rosettes and is the later Barite phase that cross-cut the other sulfides. This third generation is often associated with galena, sphalerite and Pb-Sb-sulfosalts inclusions inside colloform pyrite. The difference in the size and in the style of mineralization indicates changes in the saturation of the fluids, with respect to Barite, and that it required different time to precipitate. The second generation can be characterized by undersaturation but had more time to precipitate, while the second one is characterized by oversaturation and rapid crystallization (Shikazono 1994).

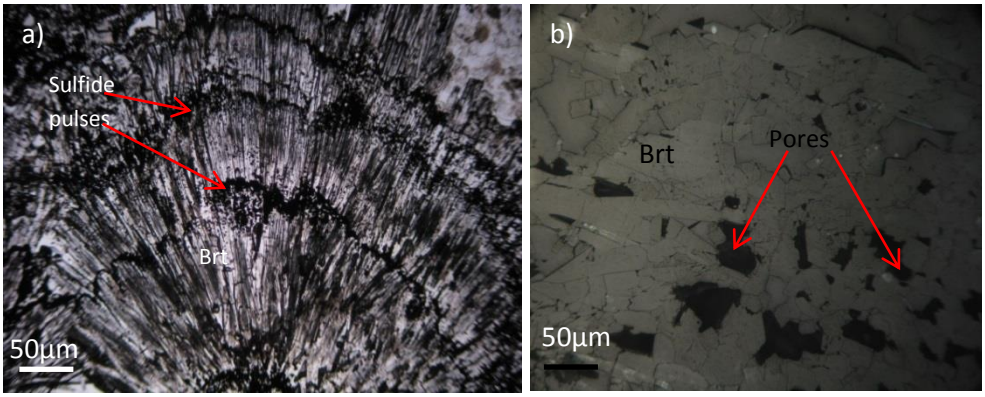

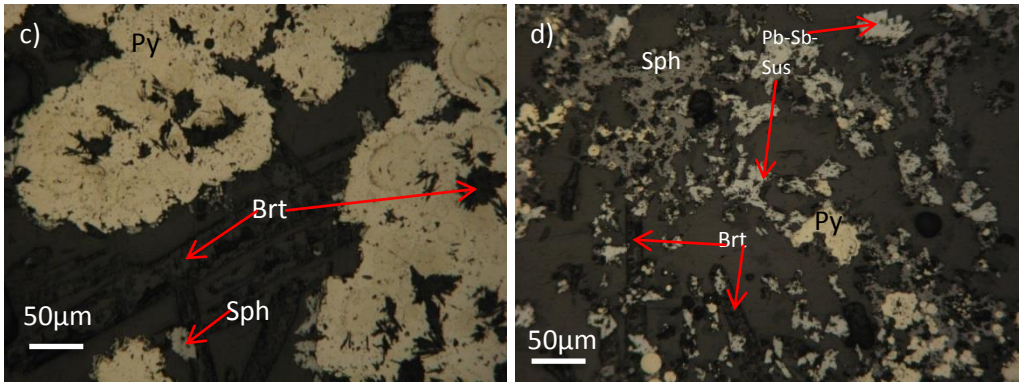

Figure 16: a) First barite generation rosette aggregates of large laths, with repeatedly pulses of sulfides mineralization. b) Recrystallized mosaic textures of barite crystals. c): Typical textures of the ISSC, displaying the two different generations of barite. The big open-space laths and blades that are associated with Pyrite mineralization can be seen in the center of the photomicrograph. While the third smaller generation in the form of rosette and dendritic aggregates cross-cuts Pyrite. d) Typical textures of ISSC showing barite blades to be associated with Sphalerite, Pb-Sb-sulfosalts and colloform Pyrite.

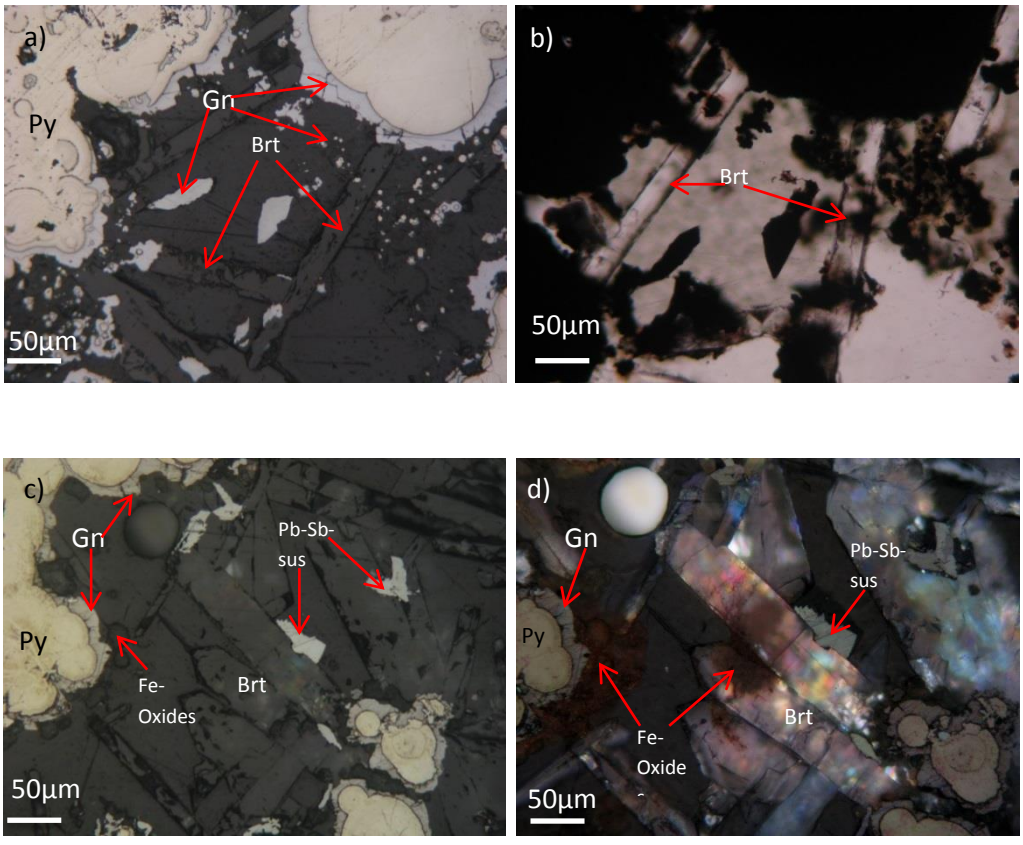

Figure 17: a): Second generation of barite in the form of blades and laths associated with pyrite and galena. Galena appears both as overgrowths around pyrite and as anhedral crystals. b): Same as a) but in transmitted light. c): barite blades and laths associated with pyrite, galena, anhedral Pb-Sb-sulfosalts and Fe-oxides. d): Same with c) but in polarized light, the Fe-oxides can be observed as intergrowths within prismatic barite crystals.

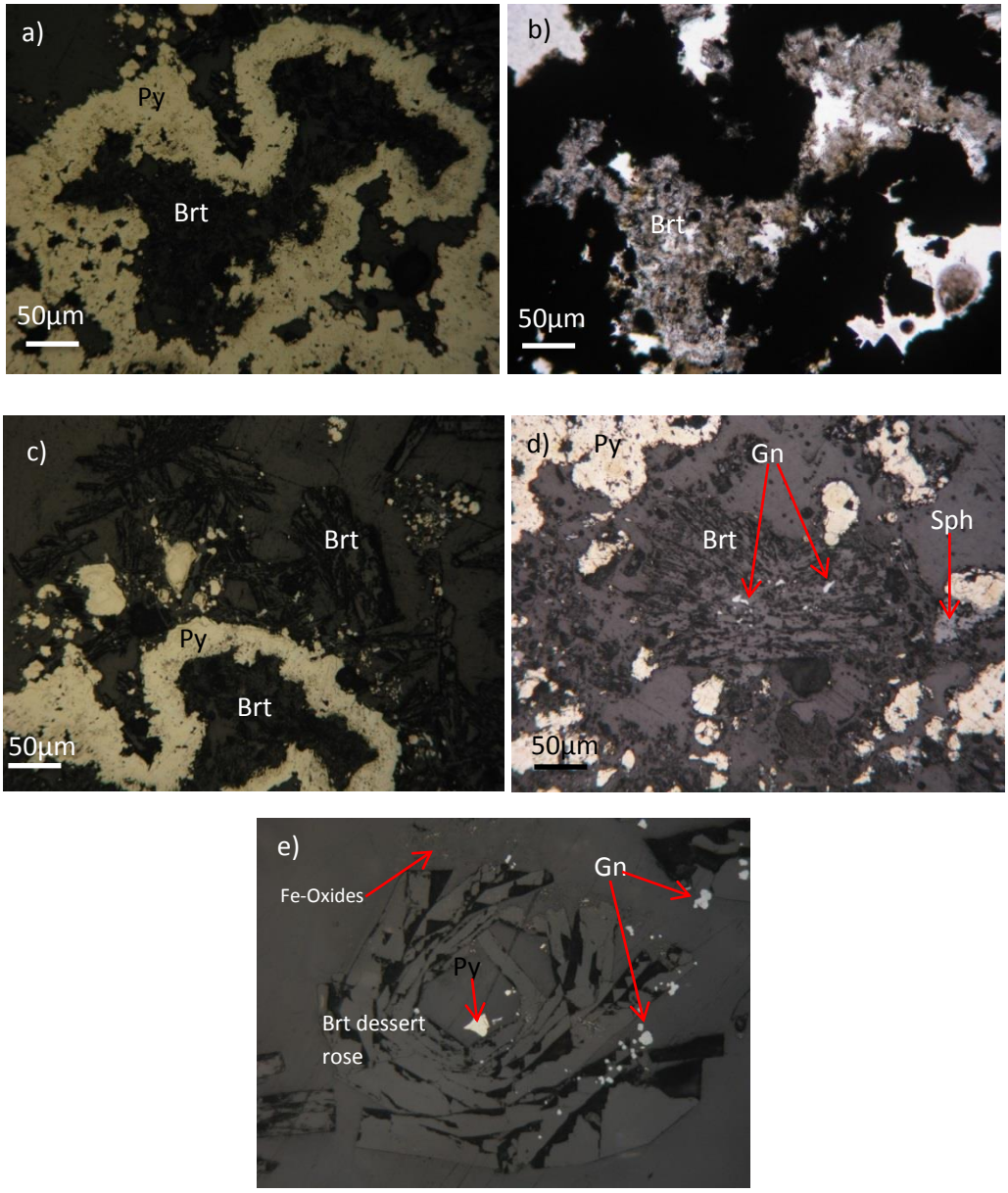

Figure 18: a): Third generation of barite aggregates, mostly rosettes, replacing pyrite. b): Same with a) under transmitted light. c): Second generation barite plumose aggregates are being replaced by pyrite, while the third generation of barite replaces pyrite. d): Example of second generation plumose barite with galena inclusions. e): Rare desert rose-like structure of the second generation of barite, associated with pyrite, galena and Fe-oxides.

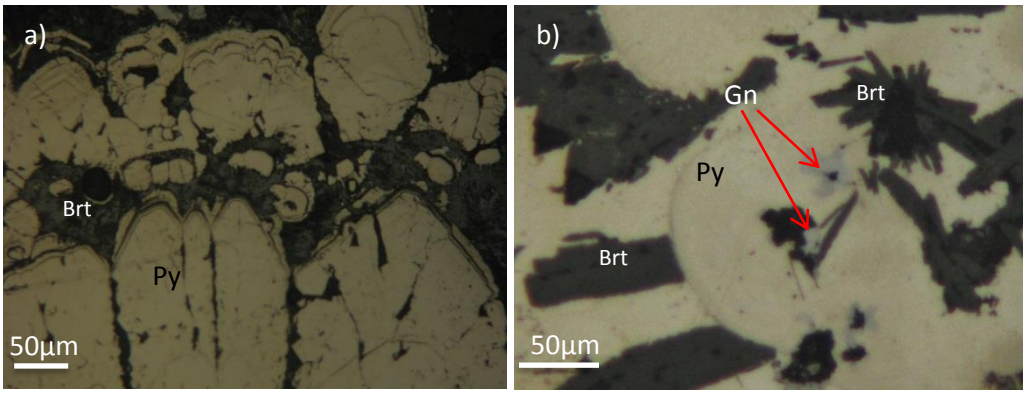

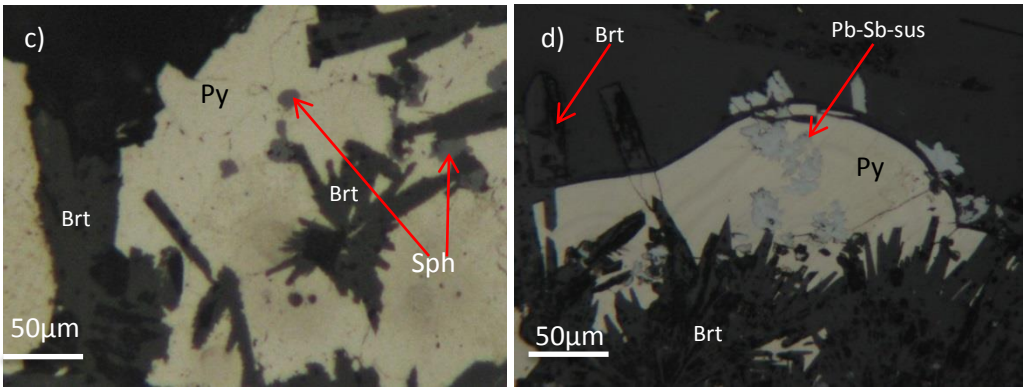

Figure 19: a) Third generation of barite cross-cutting recrystallized euhedral pyrite with nodular colloform pyrite intergrowths. b): barite and galena intergrowths as inclusions inside colloform Pyrite. c) Sphalerite and barite intergrowths as inclusions inside pyrite. d) Barite and Pb-Sb-sulfosalts intergrowths inside collofrom pyrite. The presence of barite as intergrowths with Gn, Sph, Pb-Sb-sulfosalts and Py indicates that barite is present in all the stages of ore mineralization.

Moving to the outer parts of the chimney from the core the concentration of barite increases, while that of the sulfides decreases. This leads to a greater variety and more complex textures of barite mineralization. Barite mainly forms aggregates in the structure of rosettes, plumose and dendritic. Individual crystals in the form of blades and laths often create complex intergrowths. Recrystallized textures such as mosaic have also been observed. Intergrowths with Pb-Sb-sulfosalts and stibnite are also common. Interesting enough, inclusions of metal-minerals follow barite's crystal growth zones, forming that way zonal crystals. The majority of the barite crystals display a rich in fluid inclusions core. The dominant barite generation in these parts of the chimney is the third one.

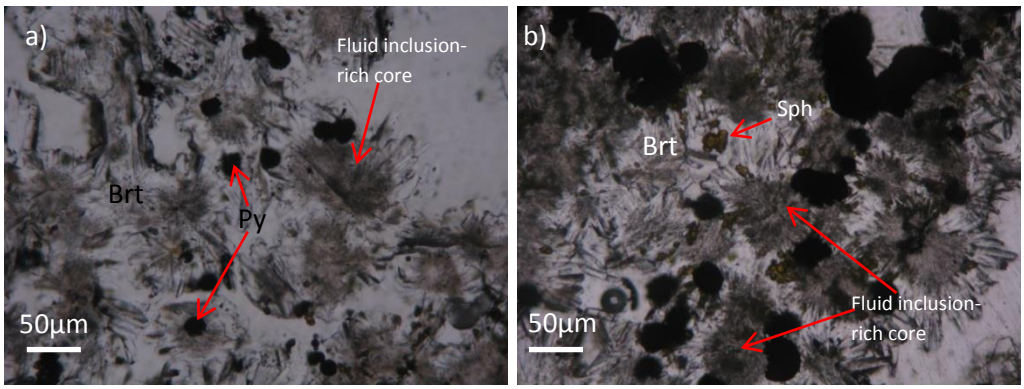

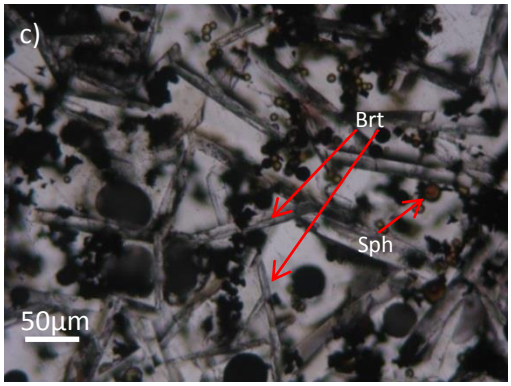
c)
Brt
Sph
50μm

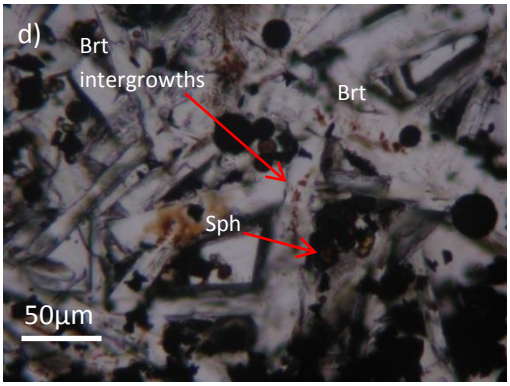
d)
Brt
intergrowths
Brt
Sph
50μm

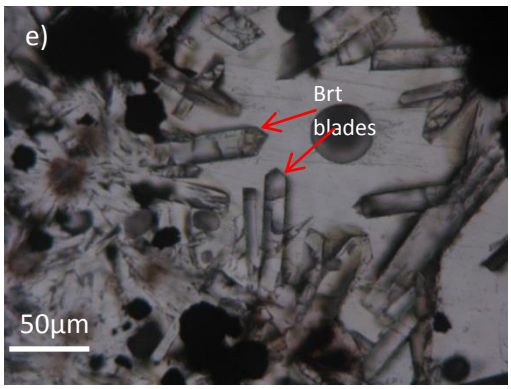
e)
Brt
blades
50μm

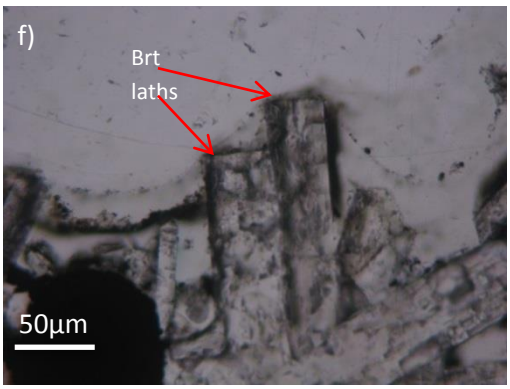
f)
Brt
laths
50μm

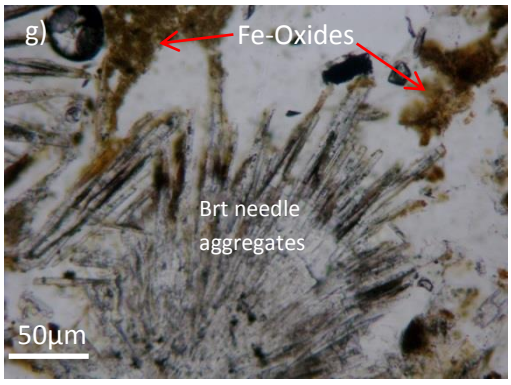
g)
Fe-Oxides
Brt needle
aggregates
50μm

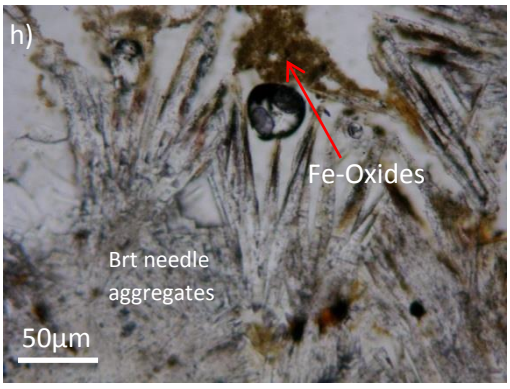
h)
Fe-Oxides
Brt needle
aggregates
50μm

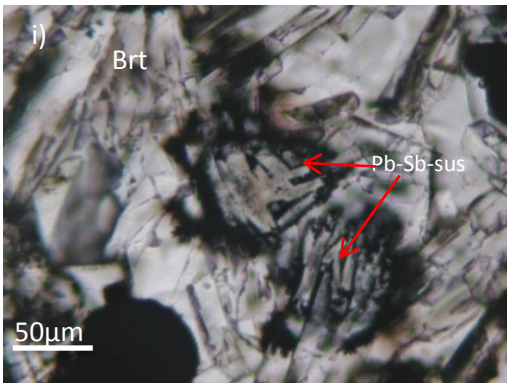
i)
Brt
Pb-Sb-sus
50μm

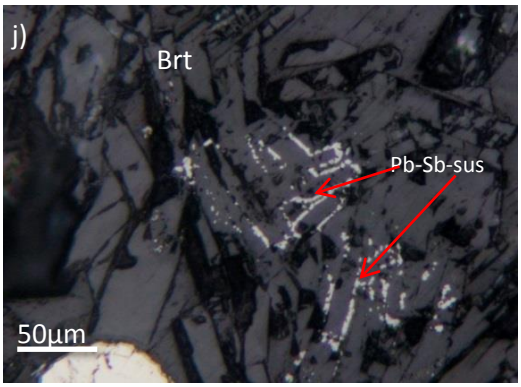
j)
Brt
Pb-Sb-sus
50μm

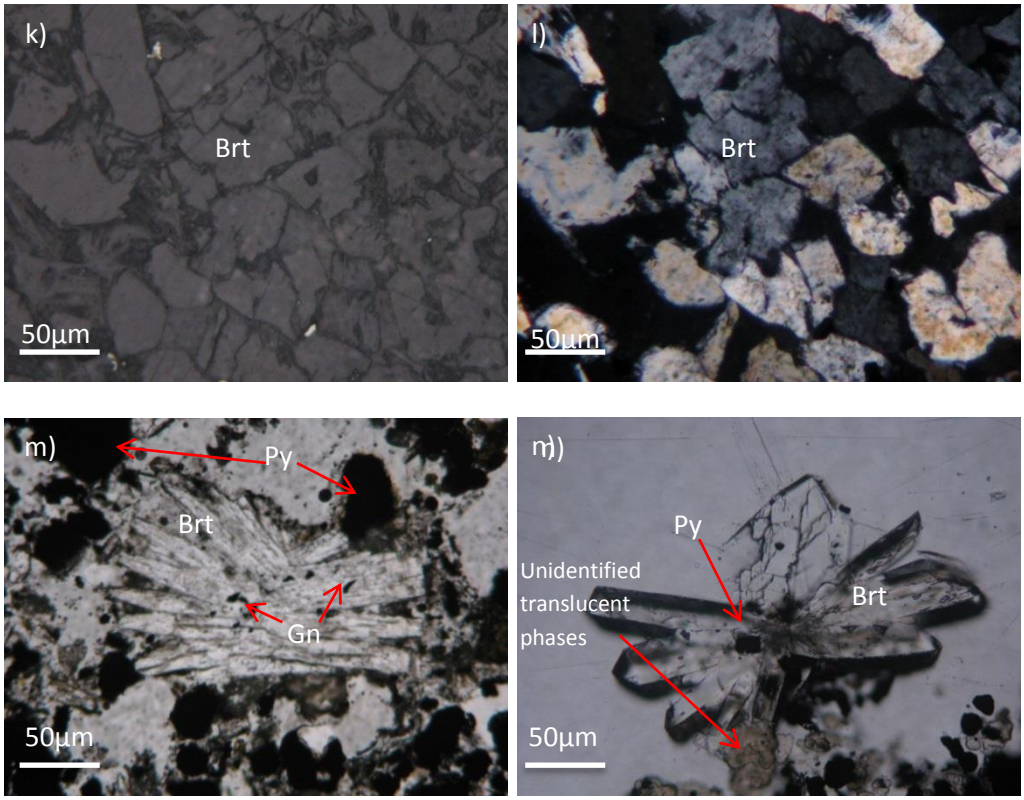

Figure 20: a), b) Typical dendritic rosette aggregates of barite. Note the rich in fluid and solid inclusions core and the absence of sulfides. c), d), e), f) Photomicrograph of barite blades and laths, the most common barite textures, associated with globular pyrite and sphalerite. Notice at d) the barite complex intergrowths as the result of compression of two independent crystals. g), h) Needle-like barite aggregates associated with Fe-Oxides, usually found at the outer parts of the chimney. i) Pseudo-Zonal barite associated with Pb-Sb-sulfosalts. Pb-Sb-sulfosalts precipitated between the cracks of barite crystals leaving the false impression of zonal structures. j) Same with i) but under reflected light. k) Recrystallized mosaic textures of barite aggregates under reflected light. l) Same with k) but under transmitted light with crossed Nichols. m), n) Plumose aggregates barite associated with pyrtie, sphalerite, Pb-Sb sulfosalts and unidentified translucent phases.

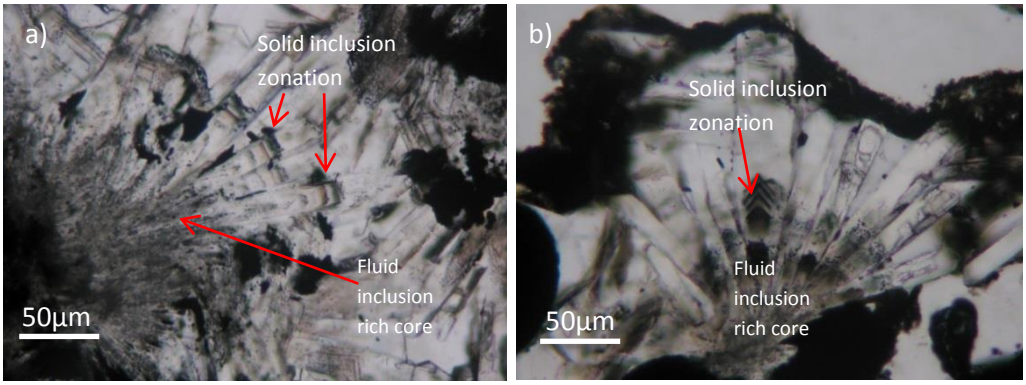

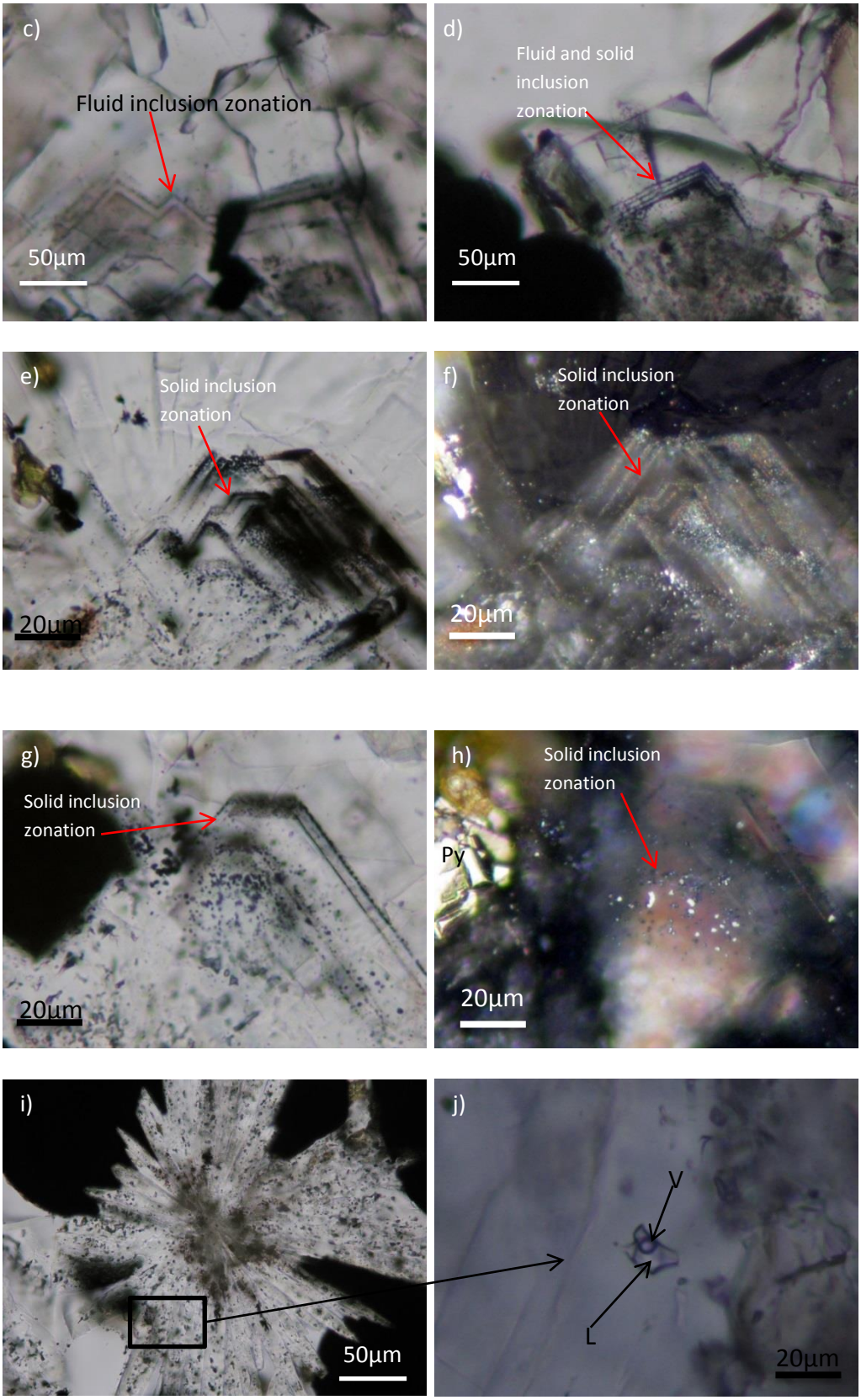
c)
Fluid inclusion zonation
50µm
d)
Fluid and solid inclusion zonation
50µm
e)
Solid inclusion zonation
20µm
f)
Solid inclusion zonation
20µm
g)
Solid inclusion zonation
20µm
h)
Solid inclusion zonation
Py
20µm
i)
50µm
j)
V
L
20µm

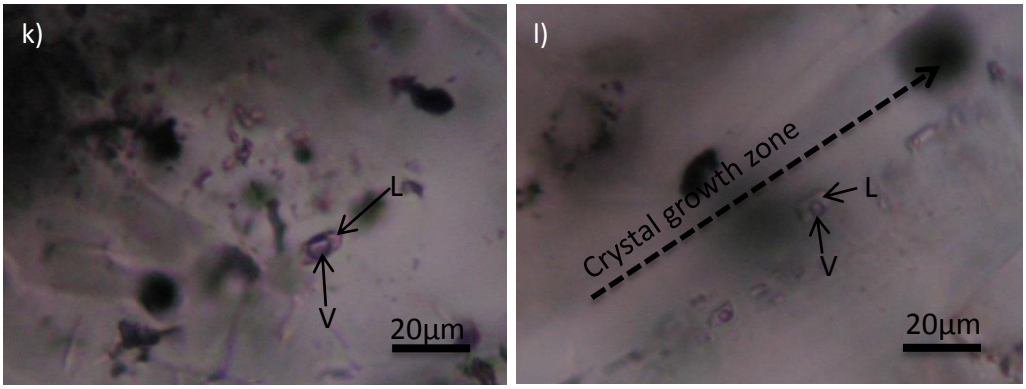

Figure 21: a), b) Zonal barite aggregates related with primary solid inclusions at the edge of the crystals. The inclusions are deemed primary as they present a three-dimensional distribution and they follow the host crystal's growth zones. A rich in fluid inclusions core is also observed. c), d) Primary fluid inclusion rich barite crystals with possible high organic content. e), f), g), h) Co-existence of primary solid and fluid inclusions inside barite crystals. The identification of the sulfide-minerals wasn't possible with only the use of optical microscope due to the small size of the inclusions. i) Rosette barite aggregates containing primary fluid inclusions. j) Zoomed photomicrograph of i) showing primary two-phase liquid rich fluid inclusion. k) Example of primary vapor-rich fluid inclusion in Barite crystal. l) Prismatic primary liquid inclusions assemblage. The inclusions tend to follow the prismatic crystal's shape.

8.2.2 Barite in the OAsL

Barite again in this zone is the dominant sulfate mineral compromising the matrix between the sulfide phases. There has been also identified another fourth generation of barite mineralization in the OAsL. This generation comprises the bed for the As-sulfides to precipitate. The most common occurrence of this generation is in the forms of rosette and plumose aggregates, large open-space blades and laths and rare needle-like structures. Complex intergrowth structures and zoned barite crystals associated with As-sulfides are evidence for co-precipitation of barite with the As-sulfides, showing also that As-sulfides are a product of mixing too.

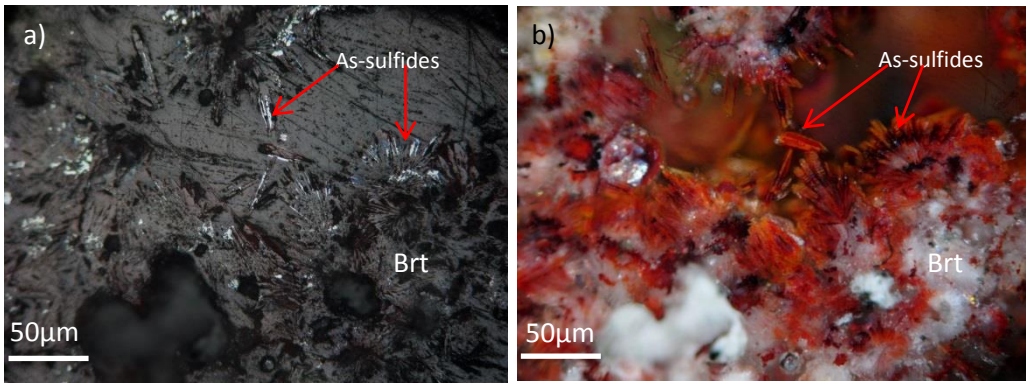

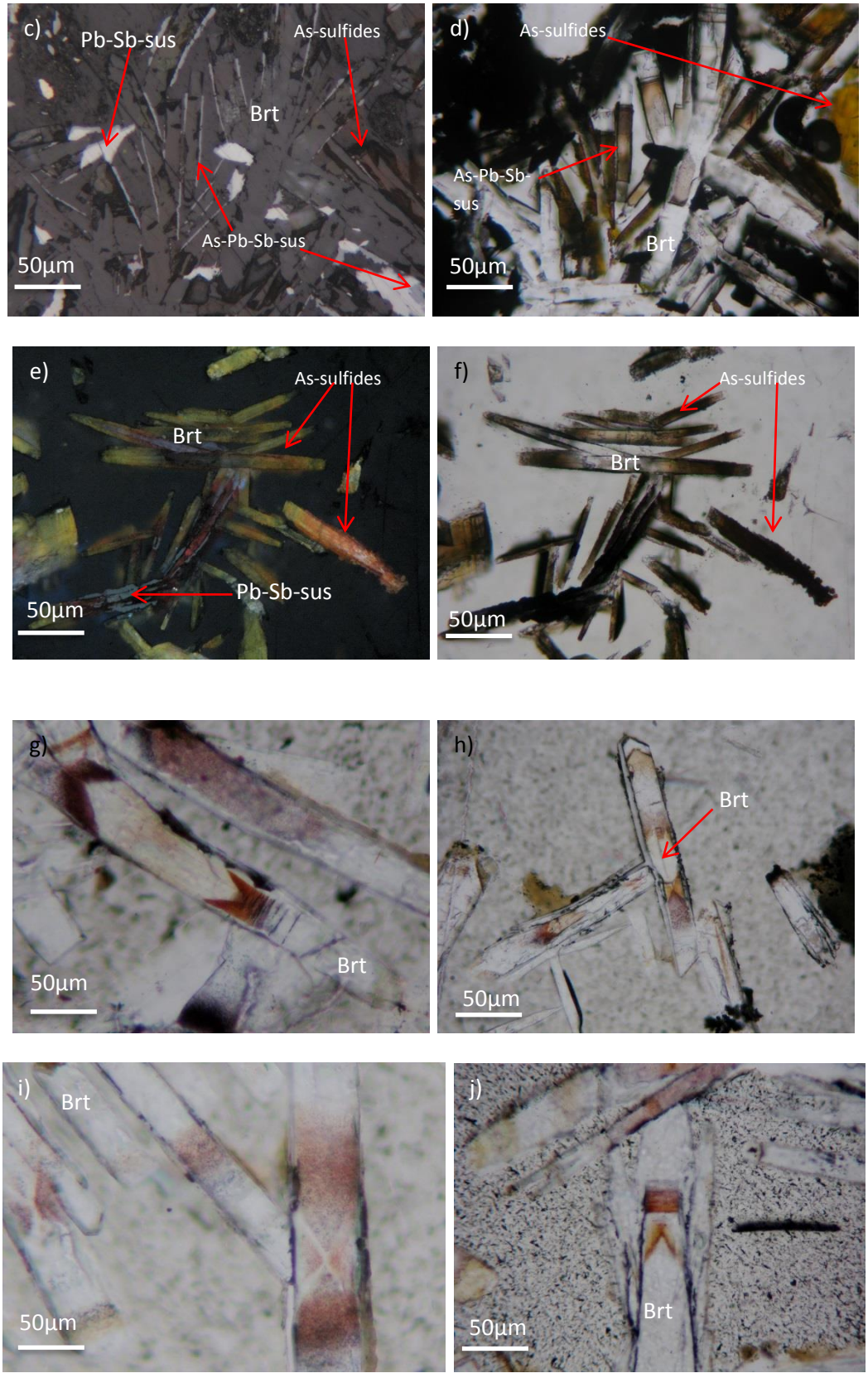
c)
Pb-Sb-sus
As-sulfides
Brt
As-Pb-Sb-sus
50μm
d)
As-sulfides
As-Pb-Sb-sus
Brt
50μm
e)
As-sulfides
Brt
Pb-Sb-sus
50μm
f)
As-sulfides
Brt
50μm
g)
Brt
50μm
h)
Brt
50μm
i)
Brt
50μm
j)
Brt
50μm

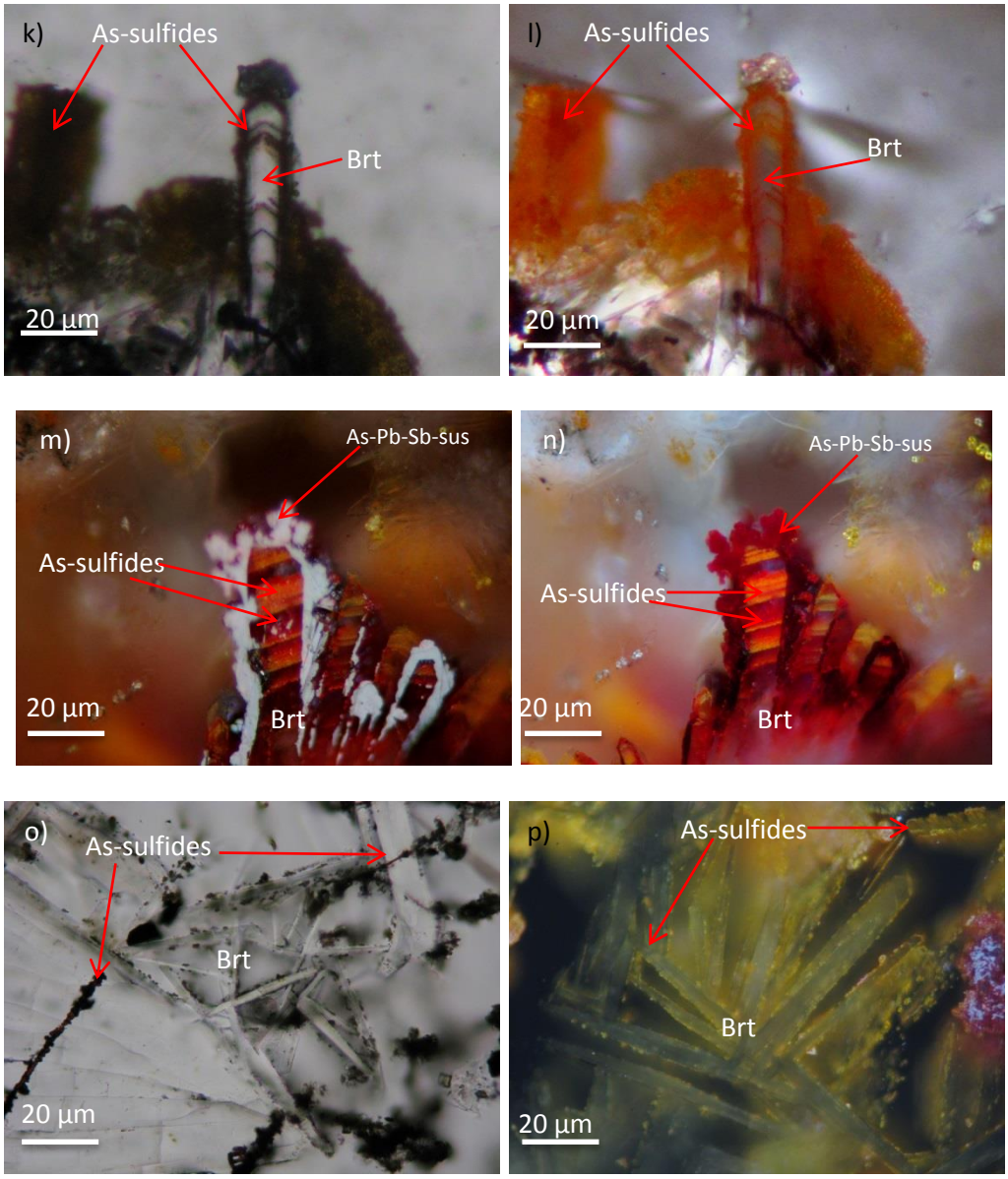

Figure 22: a) Typical textures of the outter barite wall in the form of rosette aggregates with As-sulfide intergrowths (red internal reflections). b) Same with a) but with crossed Nichols under reflected light. Note the strong internal reflections. c) As-sulfides surrounding barite crystals. d) Transmitted light photomicrograph showing barite intergrowths with As-sulfides. e), f) Barite intergrowths with As-sulfides giving barite yellow and red internal reflections. Note the visible zonation in f). g), h), i), j) Complex barite intergrowths with As-sulfides giving barite various colors (yellow, orange, red, pink). These textures might be a result of crystals adhesion trapping that way As concentrations. k) Transmitted light photomicrograph of zoned barite crystal related with As-sulfides. l) Same with k) but with crossed Nichols. Note the orange internal reflections. m) Reflected light photomicrograh of zoned barite crystals. n) Same with m) but with crossed Nichols. Notice the interchanges between the red and oragne coloured banded zonation. o) Needle-like barite crystals related with filamentous As-sulfides. p) Needle-like barite crystals with orange internal reflections due to intergrwoths with As-sulfides under reflected light.

8.2.3 Main sulfate-sulfide-sulfosalts mineral phases and their textures in ISSC

Pyrite stage

Pyrite is the dominant sulfide phase in the ISSC. Previous work on pyrite textures-evolution has shown that there are four petrographic types (Zegkinoglou 2020).

Pyrite 0 (Py0): Py0 appears as euhedral pseudomorphs of recrystallized primary anhydrite and barite. Usually it occurs as the nucleus of Pyrite nodules or overgrown by colloform, microcrystalline or euhedral-zonal Pyrite.

Pyrite 1 (Py1): The most common pyrite type of the system, displaying various textures such as colloform-crustiform banded, oscillatory zoned/ concentrically laminated spheroidal masses and moss. Galena, sphalerite and Pb-Sb sulfosalts are often creating a rim around it or seen as inclusions inside it.

Pyrite 2 (Py2): Pyrite 2 represents a microcrystalline pseudo-bladed texture that in the most occasions overgrows Pyrite 1. The random arrangement of the fine recrystallized micro-crystalline pseudo-blades leave voids among the pyrite crystals giving the false impression of porosity.

Pyrite 3 (Py3): Pyrite 3 occurs either as well formed euhedral crystals or as massive euhedral zonal aggregate crystals. Typically found overgrowing Pyrite 2 or marcasite.

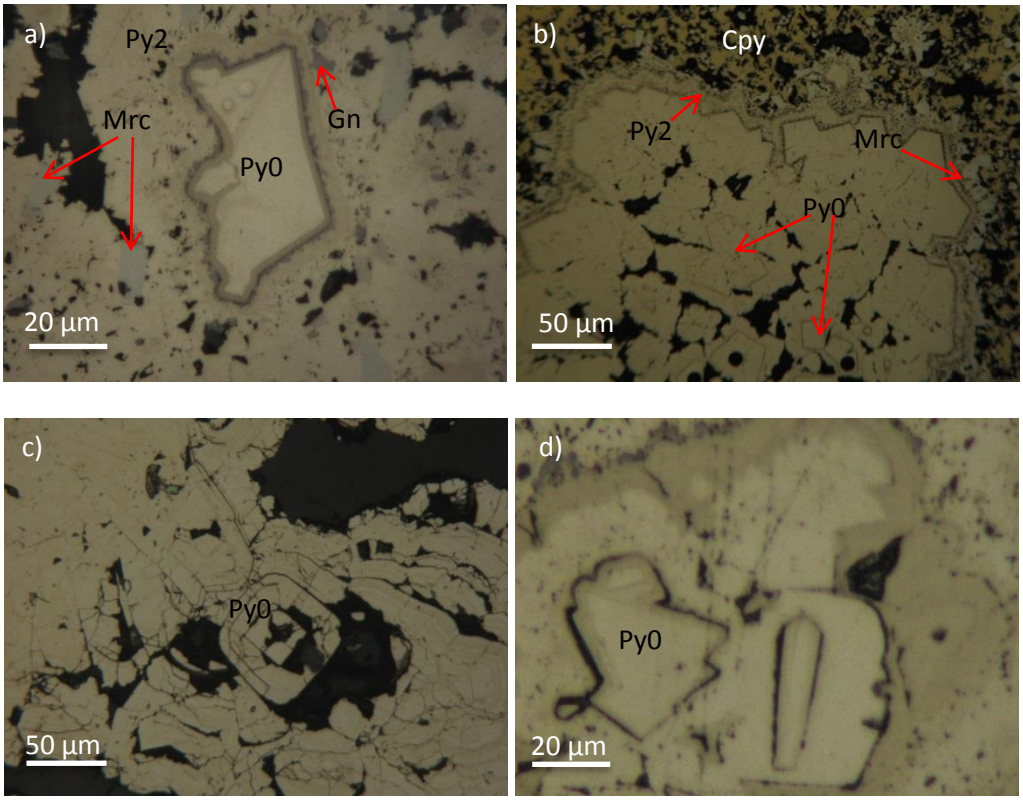

Figure 23: a): Reflected light photomicrograph of psudomorph euhedral Py0 crystal, mantled by galena rim which in turn is covered by colloform and porous pyrite. b) Py0 nucleis of massive and porous pyrite surrounded by marcasite and chalcopyrite intergrowths. c) Euhedral tetragon

Py0 as nuclei of colloform pyrite. d) Reflected light photomicrograph of massive pyrite circulating Py0, note the color difference between the two pyrite generations indicating changes in their geochemistry.

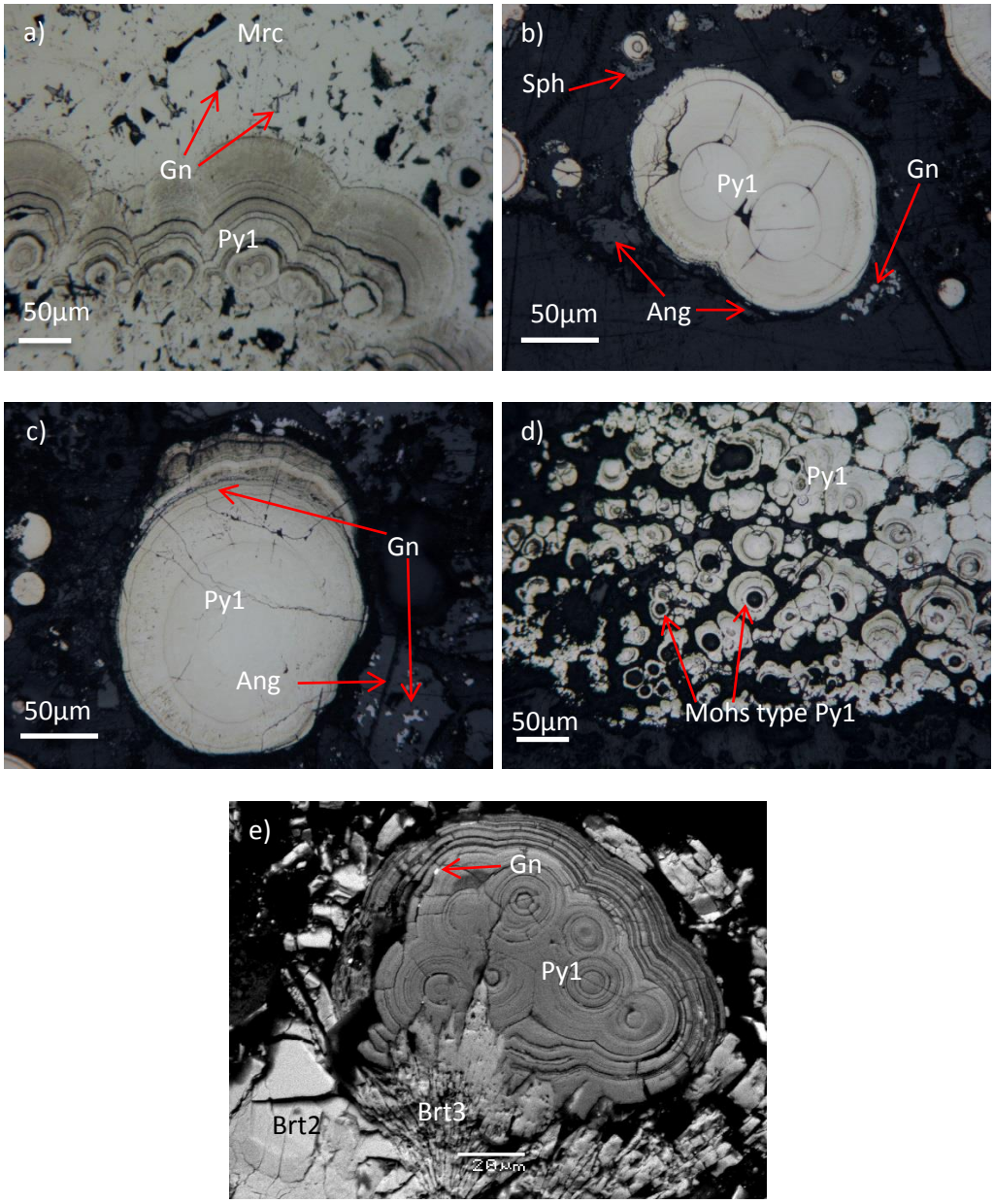

Figure 24: a) Typical colloform textures of Py1. b) Pyrite concentrically laminated microglobules surrounded by anglesite and minor galena and sphalerite. c) Singular concentrically laminated microglobular Pyrite1 with internal galena rim and inclusions. Anhedral anglesite with galena inclusions if also observed. d) Aggregates of concentrically laminated and moss type Pyrite 1. e) Back-scatter image of aggregated concentrically laminated and oscillatory zoned Pyrite 1 spheroids with dendritic barite intergrowths and galena microinclusions. Notice the difference in porosity between the second and the third barite generation.

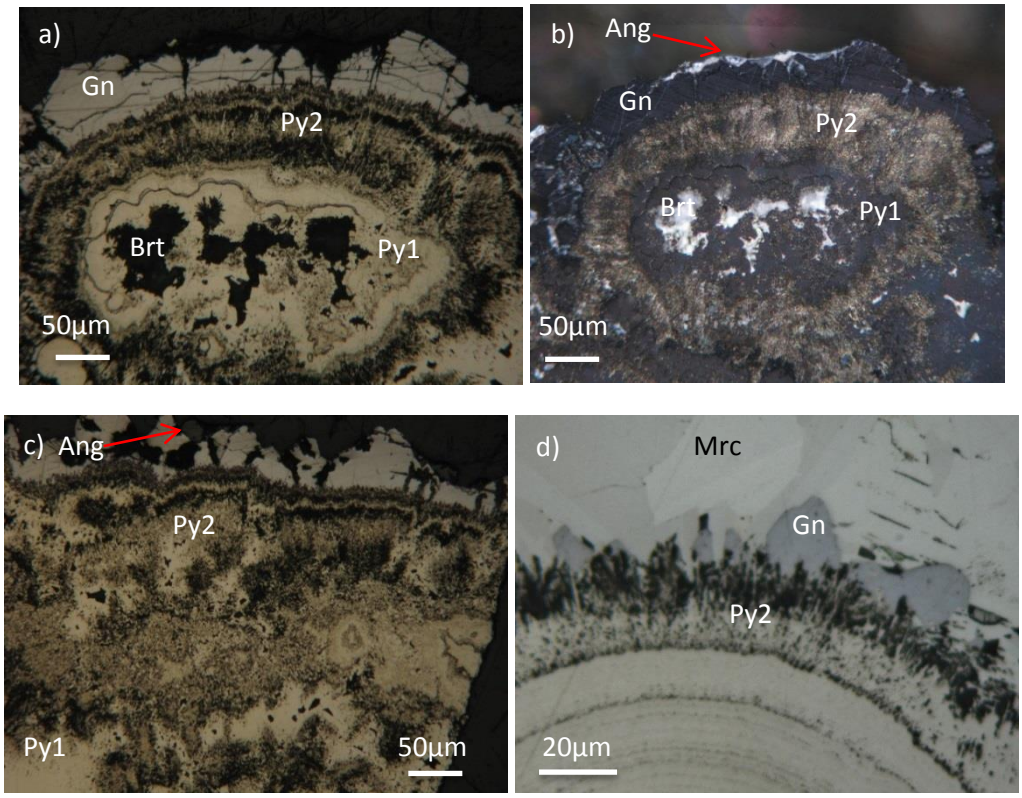

Figure 25: a) Microcrystalline Pyrite 2 overgrowing laminated with galena Pyrite 1 nuclei and in turn galena with minor anglesite overgrows Pyrite 2. Note at the center the barite intergrowths within Pyrite 1. b) Same with a) but in polarized light. The microcrystalline structure of Py2 gives it a golden shade. c) Typical Py2 textures that overgrows Py1 and in turn is overgrown by galena and anglesite. d) Reflected light photomicrograph displaying the textural evolution from Py1 to Py2. Py2 is related with galena inclusions and marcasite intergrowths.

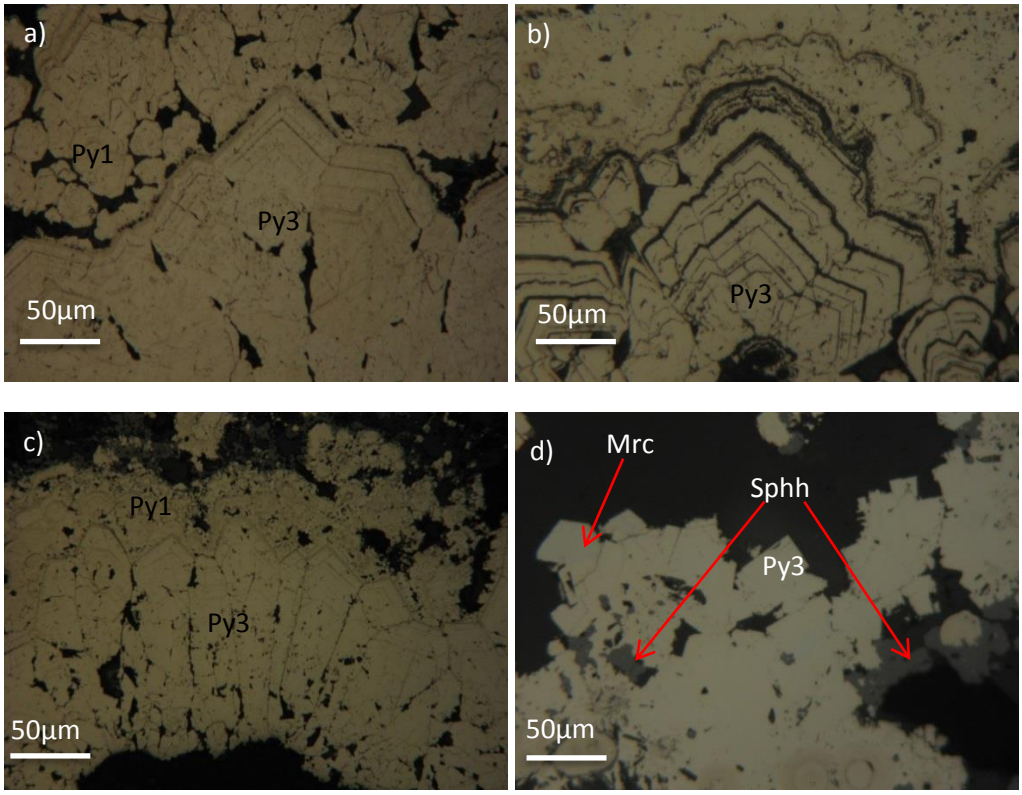

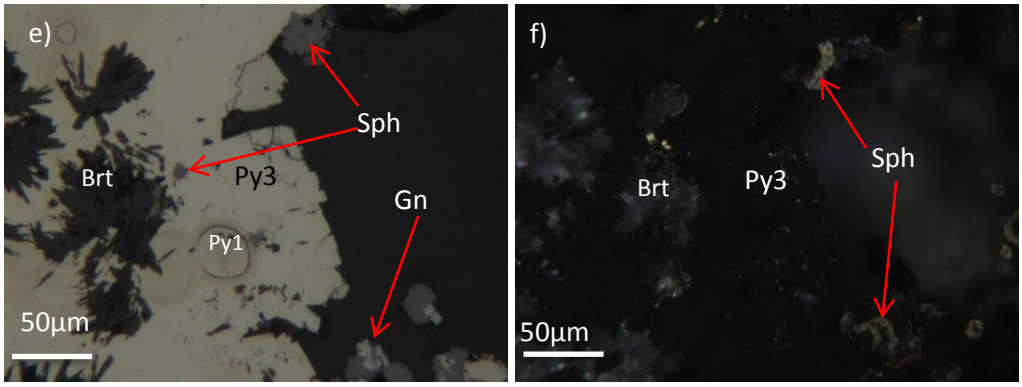

Figure 26: a), b), c) Reflected light photomicrograph of euhedral Py3 crystals with atoll shaped oscillatory zonation overgrown by colloform Py1. d) Euhedral cubic shaped Py3 crystals overgrowing Py1 related with sphalerite and barite intergrowths. Note the more white-crème color of Py3 in contrast with Py1, indicating Py1 has a greater concentration in As. f) Same with e) but in polarized light.

Marcasite (Mrc): Marcasite appears as subhedral to euhedral crystals and as microcrystalline pseudobladed grains. It is often related as intergrowths with Pyrite 3, galena and chalcopyrite or mantling Pyrite 1, generally showing a higher Temperature precipitation than that of pyrite. Under reflected light appears slightly whiter than pyrite making it difficult to distinguish the two, but in polarized light marcasite displays high polarized colors and typical twining.

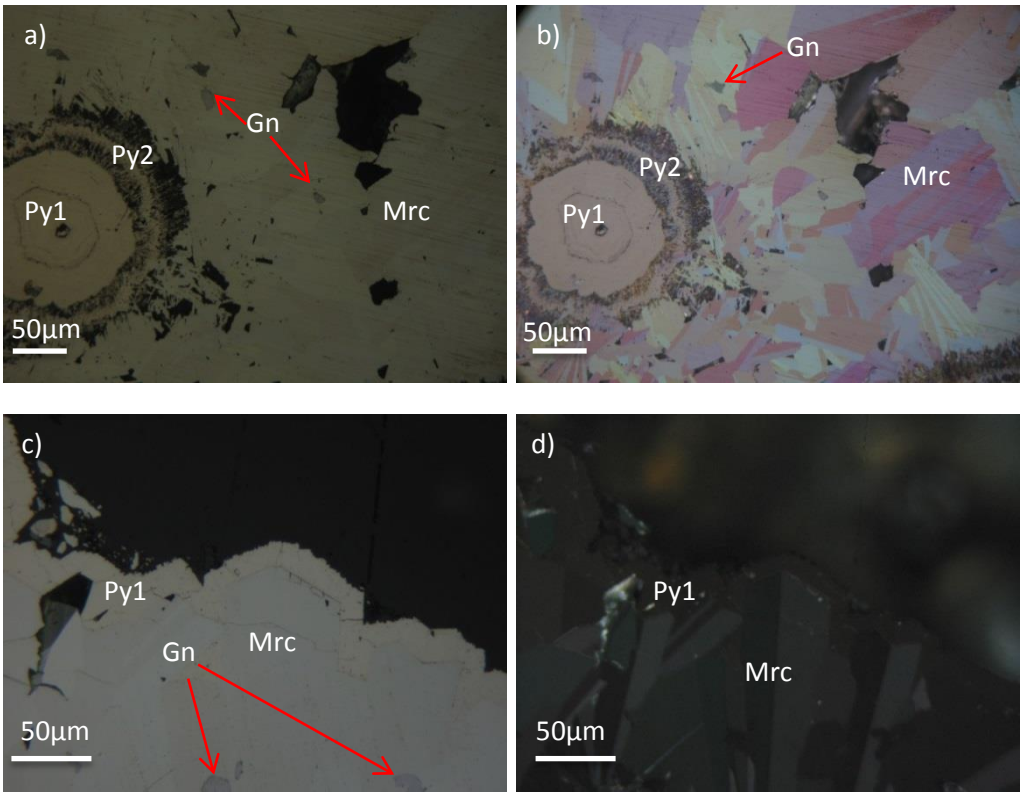

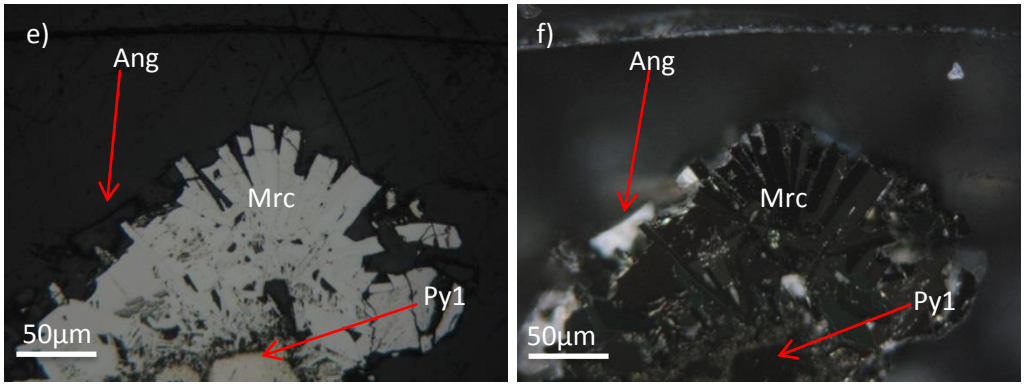

Figure 27: a) Reflected light in parallel Nichols photomicrograph of marcasite overgrowing Py2. b) Same with a) but in crossed Nichols, showing the high polarized colors of marcasite and its distinguishing twining. c) Pseudobladed marcasite (white) mantled by Py1. Note the galena inclusions in pyrite. d) Same with c) but in crossed Nichols. e), f) Pseudobladed rosette-like marcasite overgrowing Py2.

Zn-Pb-Sb-Cu stage

Sphalerite (Sph): Sphalerite under parallel Nichols reflected light can be found either as a dark-greyish massive texture or as a lighter yellow-orange microglobular-colloform banded texture. Under Polaroid light the massive sphalerite exhibits orange internal reflections, probably due to high As-content, while the microglobular one appears translucent. Under transmitted light sphalerite appears with yellow to orange colors, indicating lower Fe-contents.

Galena (Gn): Galena is present in the system with the form of anhedral to euhedral crystals and more commonly as rims overgrowing pyrite and sphalerite and in turn overgrown by sphalerite. Also, it can be observed both as inclusions and as oscillatory zone in colloform pyrite crystals. In addition is closely related with marcasite and chalcopyrite inclusions and less common with Pb-Sb-sulfosalts.

Anglesite (Ang): Anglesite is a minor mineral phase in the system and is usually found around galena as an oxidization product.

Pb-Sb-Sulfosalts (Pb-Sb-Sus): The Pb-Sb-Sulfosalts are a late mineralization stage phases in the ISSC as they cross-cut the other mineral assemblages. In addition they often occur as inclusions inside pyrite and sphalerite and as overgrows of pyrite, sphalerite and galena. Under reflected light they display various textures such as subhedral to euhedral crystals, flamboyant grains, fishbone-like structures and the most common being plumose grains.

Chalcopyrite (Cpy): Chalcopyrite is a minor sulfide phase usually found as intergrowths with marcasite, galena, sphalerite and minor pyrite, in well insulated conduits, where the hydrothermal fluid didn't contact seawater therefore keeping its high temperature. Chalcopyrite also, occurs as space and cavity filling in pyrite and marcasite crystals. In rare occasions it has been observed as inclusions in galena and sphalerite.

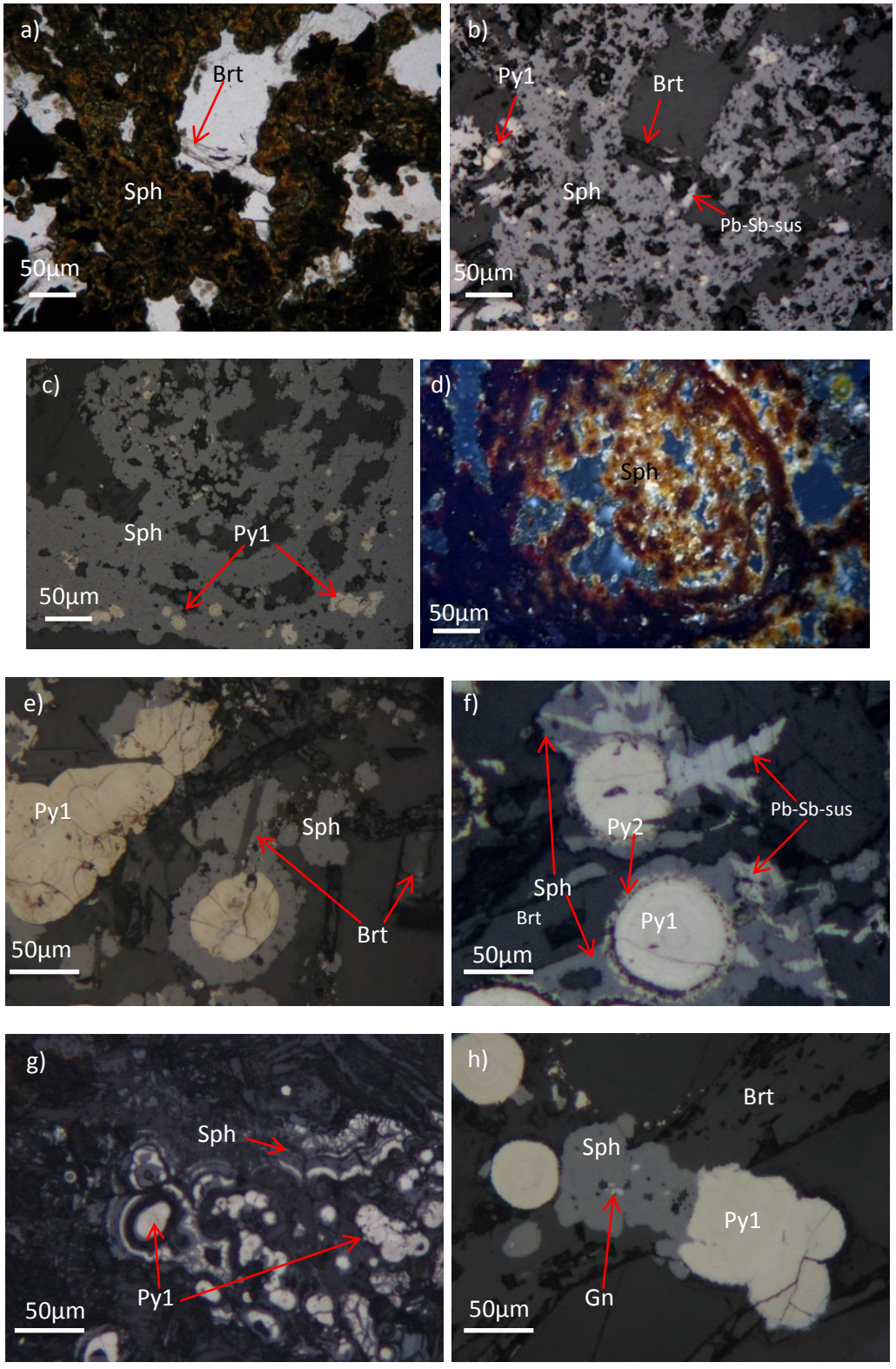
a)
Brt
Sph
50μm
b)
Py1
Brt
Sph
Pb-Sb-sus
50μm
c)
Sph
Py1
50μm
d)
Sph
50μm
e)
Py1
Sph
Brt
50μm
f)
Pb-Sb-sus
Py2
Sph
Brt
Py1
50μm
g)
Sph
Py1
50μm
h)
Brt
Sph
Py1
Gn
50μm

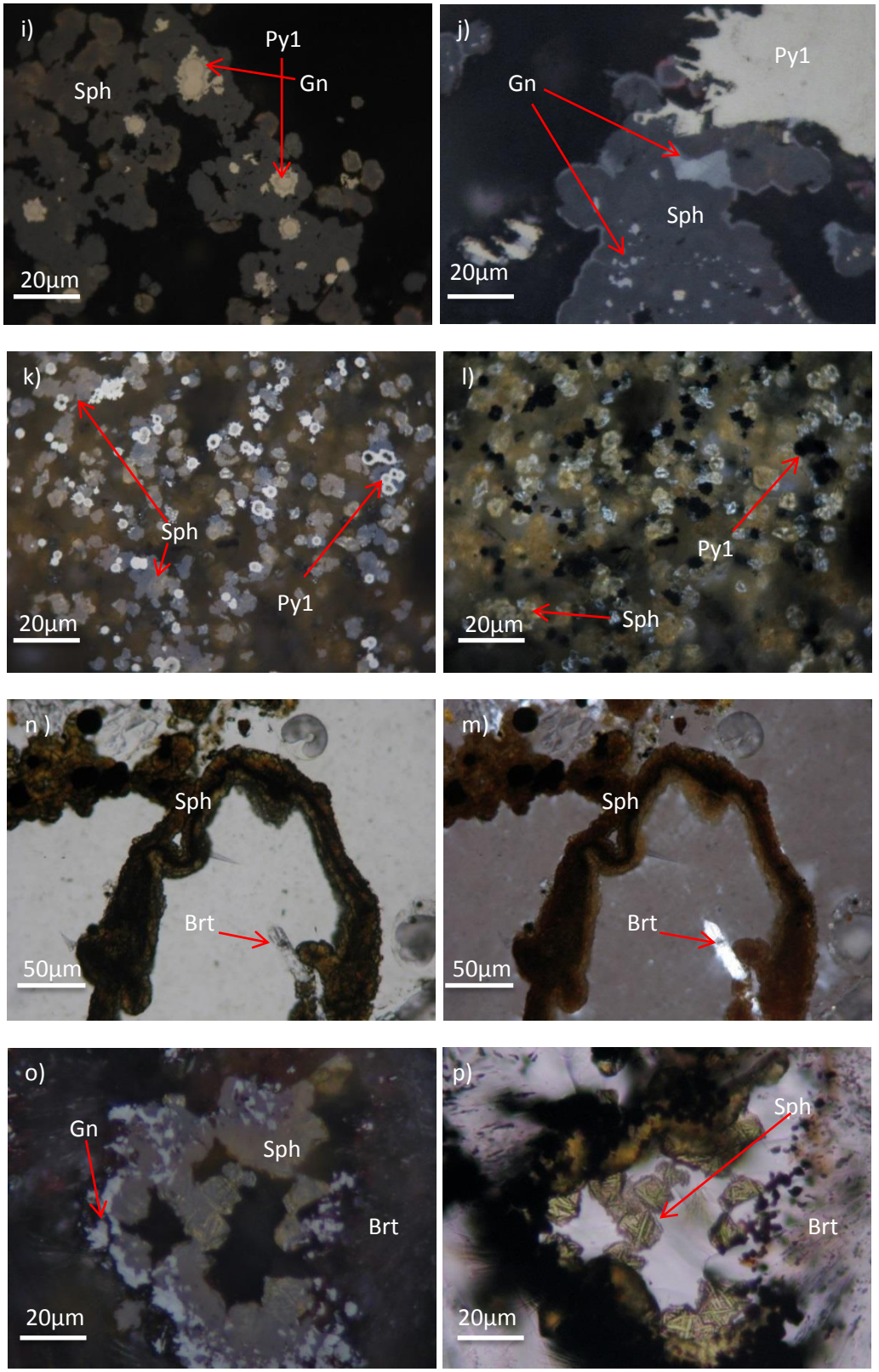

Figure 28: a) Photomicrograph of massive sphalerite appearing with yellow-orange color under transmitted light. b) Same with a) but in reflected light, note the pyrite and Pb-Sb-sulfosalts intergrowths. c) Massive porous sphalerite. d) Same with c) but with crossed Nichols. e), f) sphalerite rim around concentrically laminated Pyrite with Pb-Sb-sus intergrowths. g), h), i), j) Typical example of replacement of colloform laminated pyrite by sphalerite. Note that sphalerite replaces and the galena rim around pyrite, leaving only rare galena inclusions in the porous of sphalerite. Also at i) and j) yellow-orange and red internal reflections can be observed. k)

Reflected photomicrograph of microglobular sphalerite intense yellow internal reflections. l) Microglobular sphalerite under crossed Nichols appears translucent with yellow color. m) Zonal sphalerite under transmitted light with an exterior yellow-green color and an interior brownish shade, showing difference in trace elements concentration. n) Same with m) but under polarized light. o), p) Complex sphalerite microglobular textures with galena intergrowths and yellowish internal reflections consisting of needle-like phases, resembling saccharoidals.

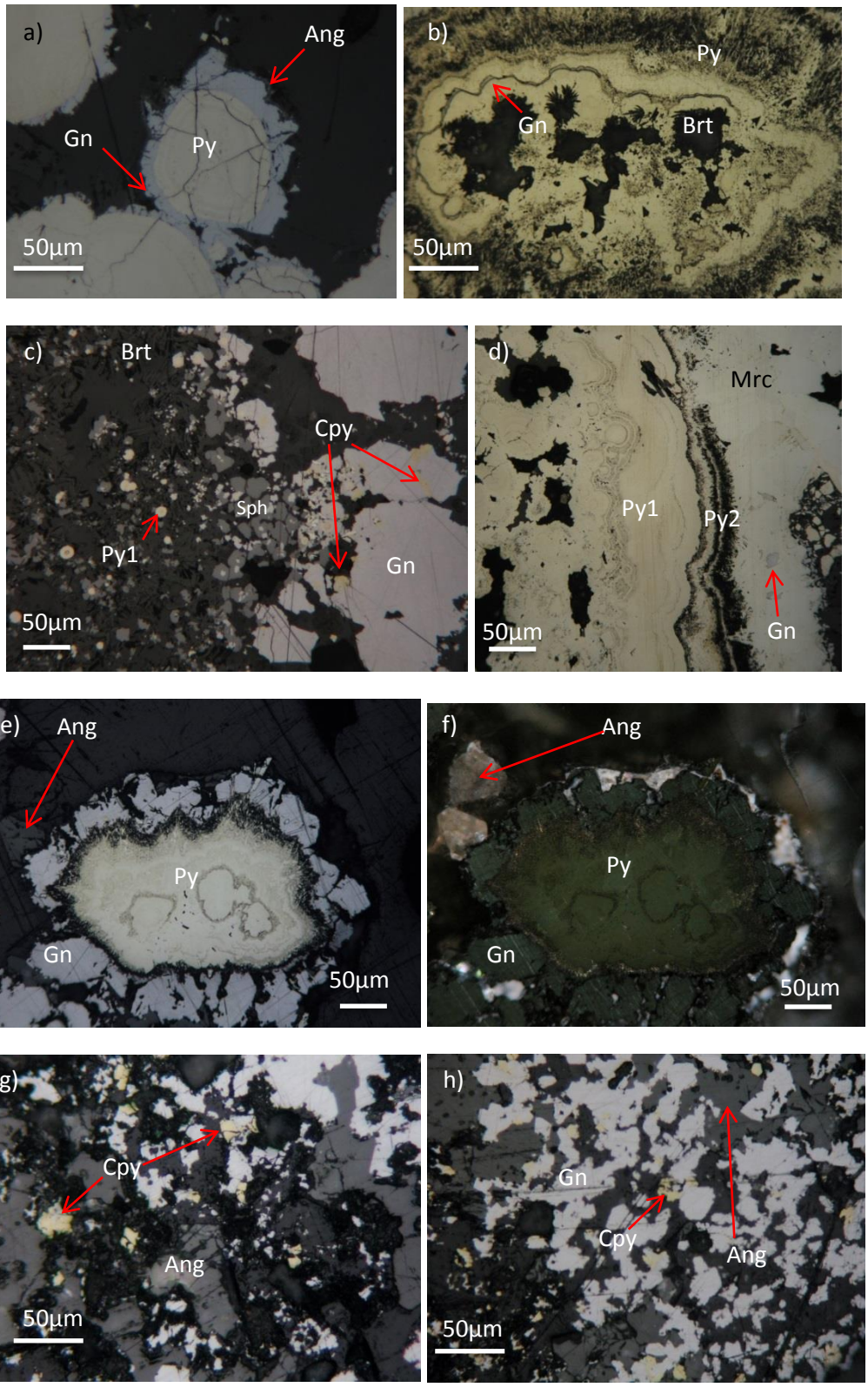

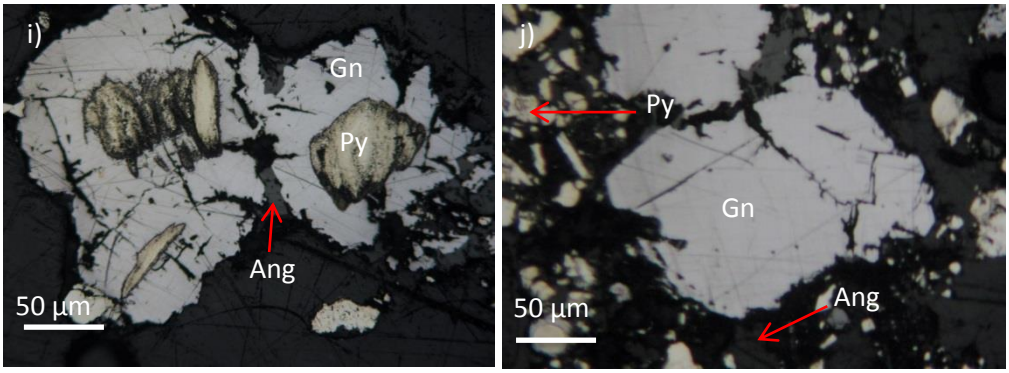

Figure 29: a), e), f) Reflected light photomicrographs of galena rim around pyrite. Note that in a) galena is overgrowing Py1 while at e) and f) is overgrowing Py2. Under polarized light (see f)) euhedral anglesite crystals are identified. b) Galena oscillatory laminated rim in Py1. c) and j) Display subhedral galena crystals. In c) visible chalcopyrite intergrowths are observed. d) Galena inclusions inside massive marcasite. g), h) Chalcopyrite, galena and minor anglesite inclusions. i) Photomicrograph of galena replacing Pyrite 2.

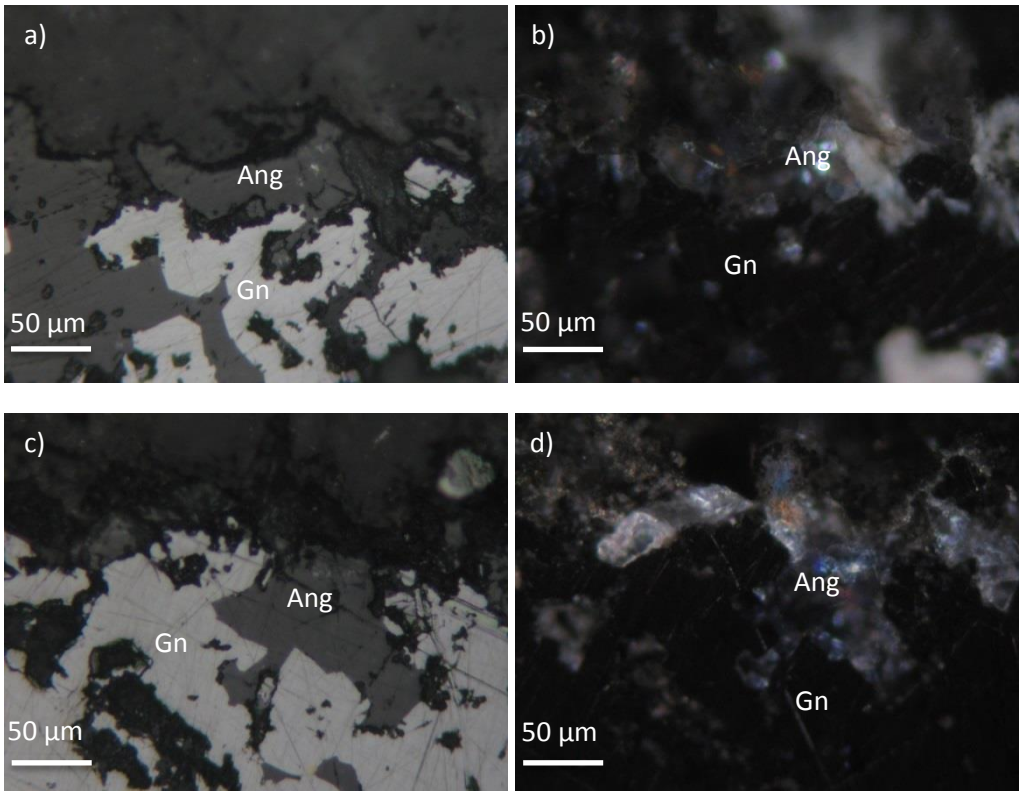

Figure 30: Reflected light photomicrographs of anglesite replacing galena a) and c) in parallel Nichols, b) and d) in crossed Nichols.

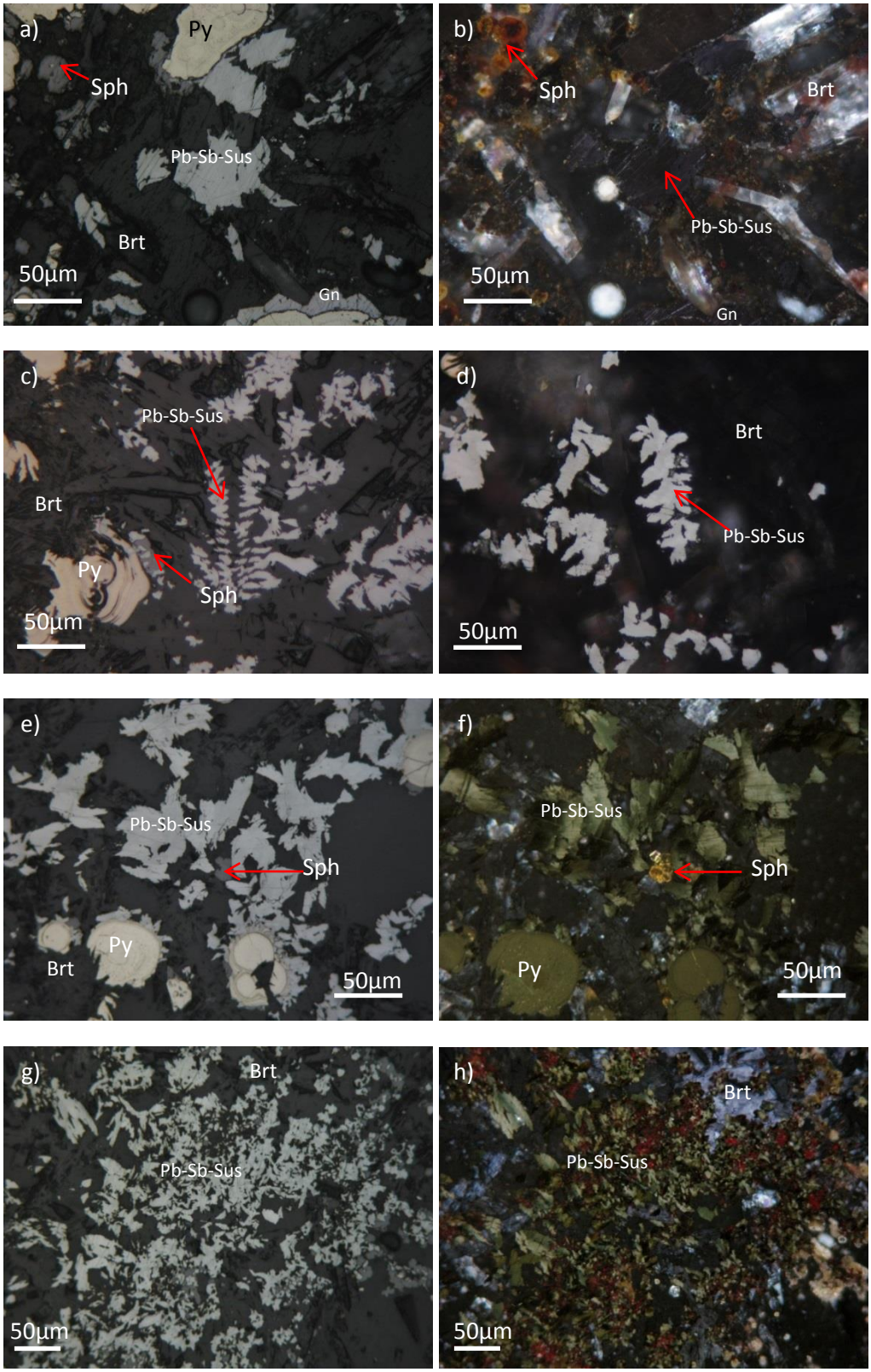
a)
Py
Sph
Pb-Sb-Sus
Brt
50µm
Gn
b)
Sph
Brt
Pb-Sb-Sus
50µm
Gn
c)
Pb-Sb-Sus
Brt
Py
Sph
50µm
d)
Brt
Pb-Sb-Sus
50µm
e)
Pb-Sb-Sus
Sph
Py
Brt
50µm
f)
Pb-Sb-Sus
Sph
Py
50µm
g)
Brt
Pb-Sb-Sus
50µm
h)
Brt
Pb-Sb-Sus
50µm

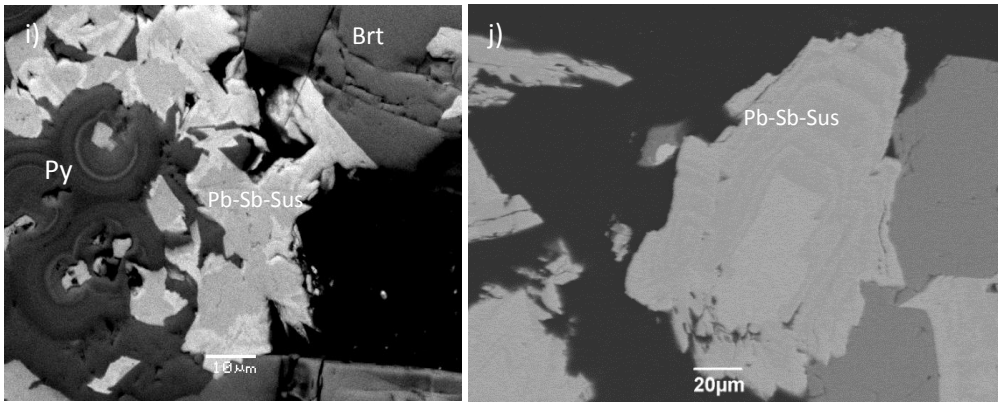

Figure 31: a), b), e), f) Impressive plumose Pb-Sb-sulfosalts textures related with pyrite, sphalerite and barite. Notice the strong anisotropy they exhibit under crossed Nickols in b) and f). c), d) Rare fishbone-like Pb-Sb-sus structures. g) Pb-Sb- sulfosalts aggregates related with minor sphalerite intergrowths. h) Same with g) but with crossed Nichols. Note the red internal reflections caused by Fe-oxides possible. i) Back-scatter image of Pb-Sb-sulfosalts intergrowths with pyrite and barite crystals. Note the difference in brightness the Pb-Sb-sus display, indicating that they are two different phases (one Pb rich and one Sb rich). j) Rare Zonation of Pb-Sb-sulfosalts resembling the magmatic zonation of plagioclase.

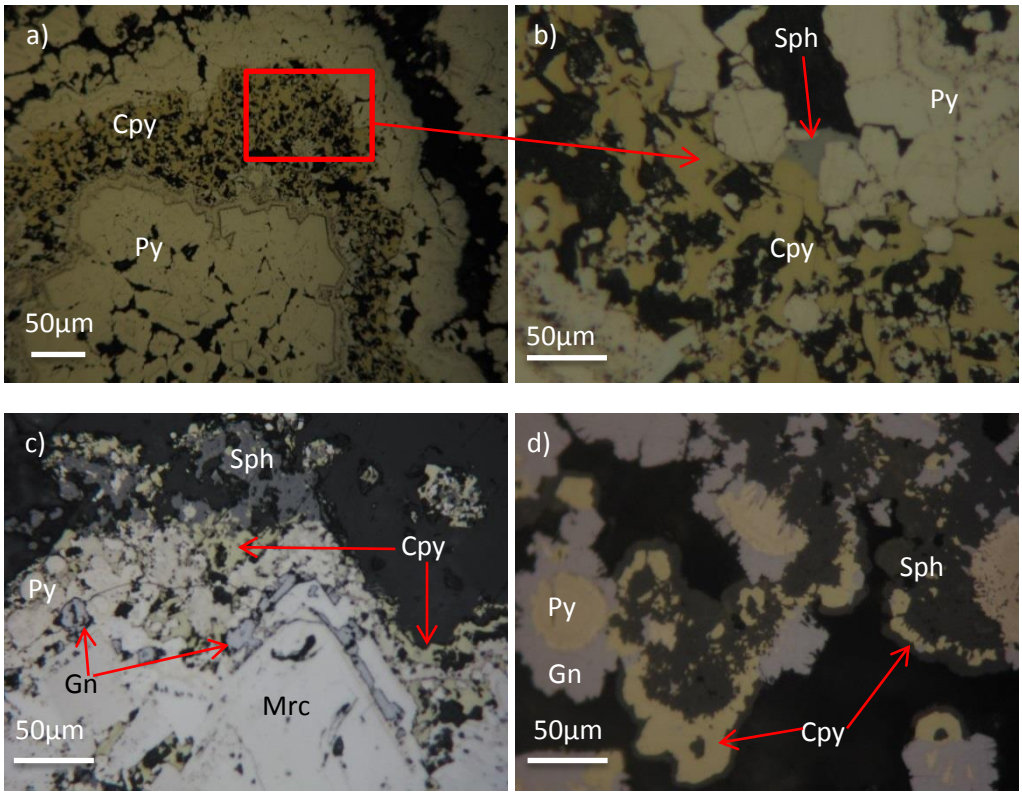

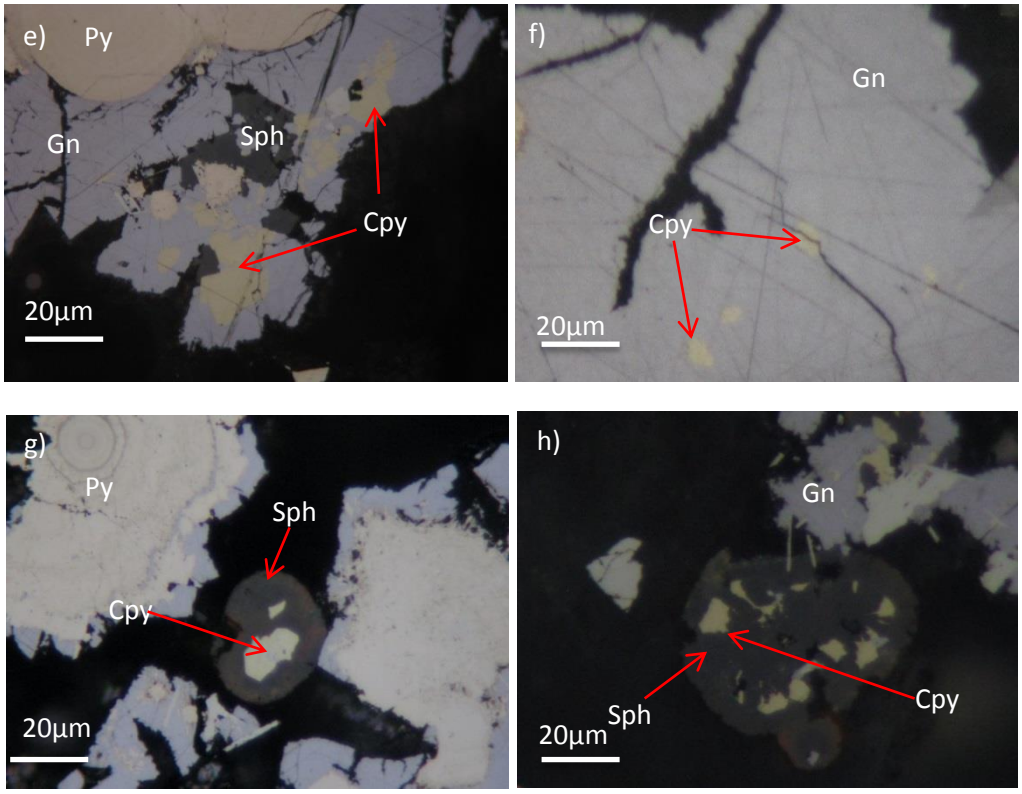

Figure 32: a) Pyrite nodule core containing a chalcopyrite zone. Chalcopyrite precipitates after Pyrite 3 and marcasite. b) Zoomed photomicrograph of a) showing chalcopyrite and sphalerite co-precipitation. c) Pyrite-Marcasite nodule where voids and cavities where filled by late chalcopyrite and galena. d) Chalcopyrite rim around sphalerite, galena and pyrite complex intergrowths. e), f) Chalcopyrite inclusions inside anhedral galena crystals. Notice in f) that the cracks cut the inclusions inside galena meaning chalcopyrite didn't precipitates into cavities. g), h) Chalcopyrite and galena inclusions in sphalerite crystals that have reddish internal reflections.

8.2.4 Main sulfate-sulfide-sulfosalts mineral phases and their textures in OAsL

Anhydrite (Anh): Anhydrite is a minor component in these samples and it usually occurs in the outer parts of the chimneys as the first mineral phase to precipitate before it gets replaced by barite. It typically appears as dissoluted blades and laths and as anhedral-subhedral crystals. Relics of anhydrite have been observed inside barite crystals.

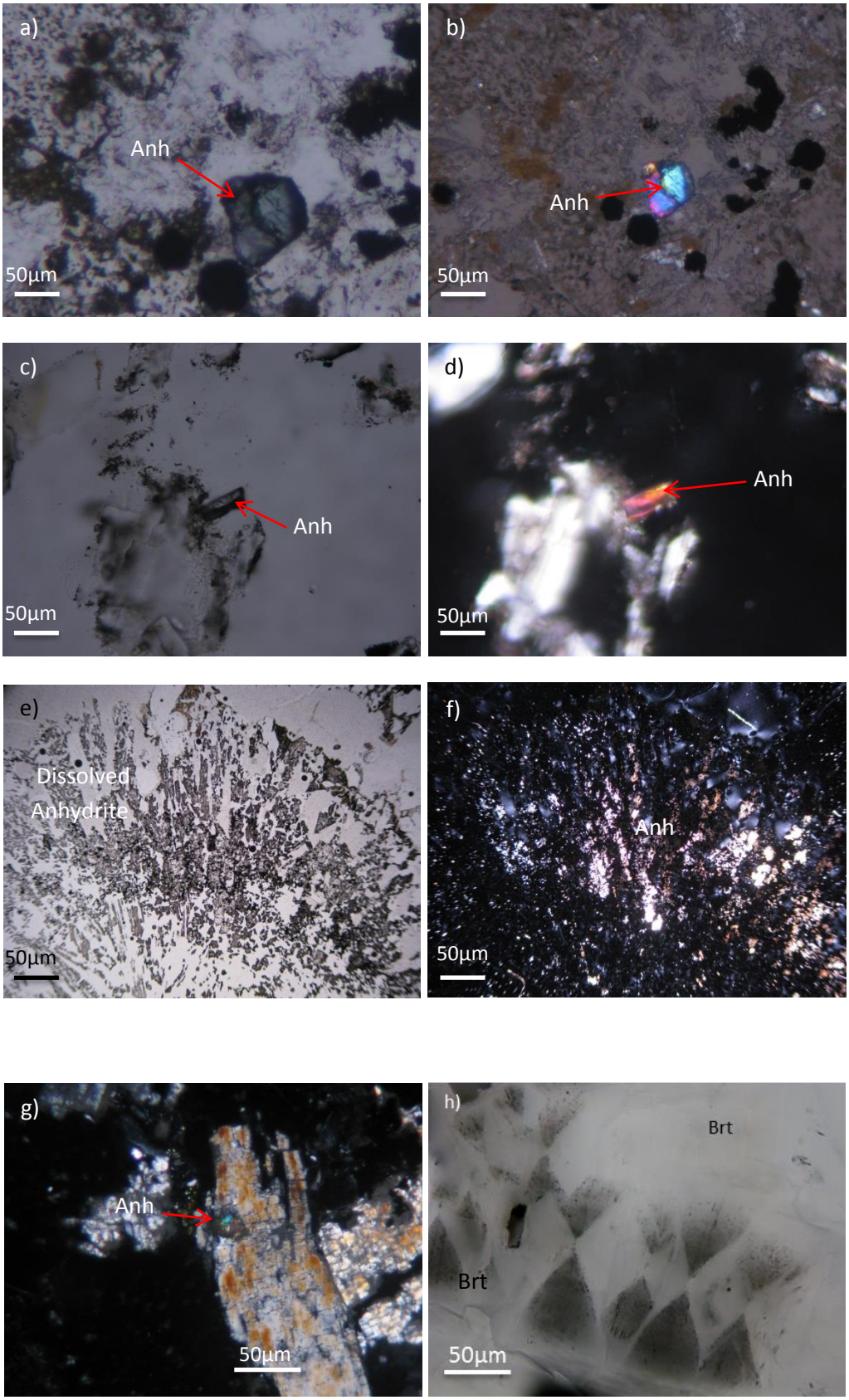
a)
Anh
50µm
b)
Anh
50µm
c)
Anh
50µm
d)
Anh
50µm
e)
Dissolved
Anhydrite
50µm
f)
Anh
50µm
g)
Anh
50µm
h)
Brt
Brt
50µm

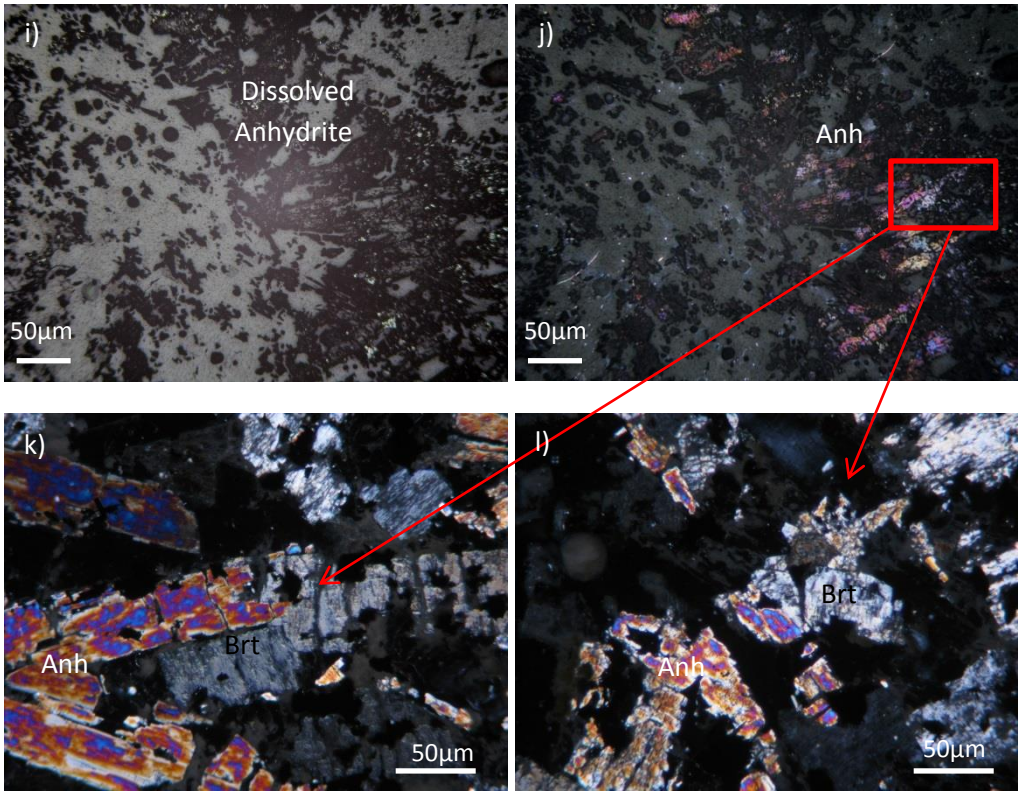

Figure 33: a) anhedral Anhydrite grain under transmitted light. b) Same with a) but with crossed Nichols. Note the high polarized colors anhydrite exhibits. c) Prismatic anhydrite crystal under transmitted light. d) Same with c) but with crossed lights. e), f) Dissoluted primary anhydrite blades under reflected light. g) Anhydrite relics inside barite crystal. h) Rare "hourglass structures resembling the hourglass structures of serpentinized olivine. Might be the product of anhydrite replacement by barite with simultanus trapping of sulfides/oxides. i) Reflected light photomicrograph of anhydrite relics. j) Same with h) but with crossed Nichols. k), l) Zoomed photomicrograph of i) showing barite replacing anhydrite.

Stibnite (Stb): Stibnite occurs usually in the form of needle-like crystals, globular-colloform grains and in rare occasions appears as dendritic crystals, overgrowing pyrite-sphalerite or Pb-Sb-Sulfosalts. Also, it is identified as intergrowths inside Barite crystals, indicating a barite-stibnite co-precipitation. Stibnite in turn is overgrown by As-sulfides.

Kermesite (Krm): Kermesite is the product of Stibnite oxidization and is difficult to distinguish from as they both precipitate in the form of needles. In contrast with stibnite, kermesite displays red internal reflections due to the present of oxygen.

As-Pb-Sb-Sulfosalts (As-Pb-Sb-Sus): As-Pb-Sb-Sulfosalts are thought to be precipitated at the last stage of mineralization as a result of lower temperatures and mixing with seawater. They commonly overgrow Pb-Sb-sulfosalts, pyrite and barite. They also create intergrowths with the Pb-Sb-sulfosalts, revealing a close relationship between the two of them.

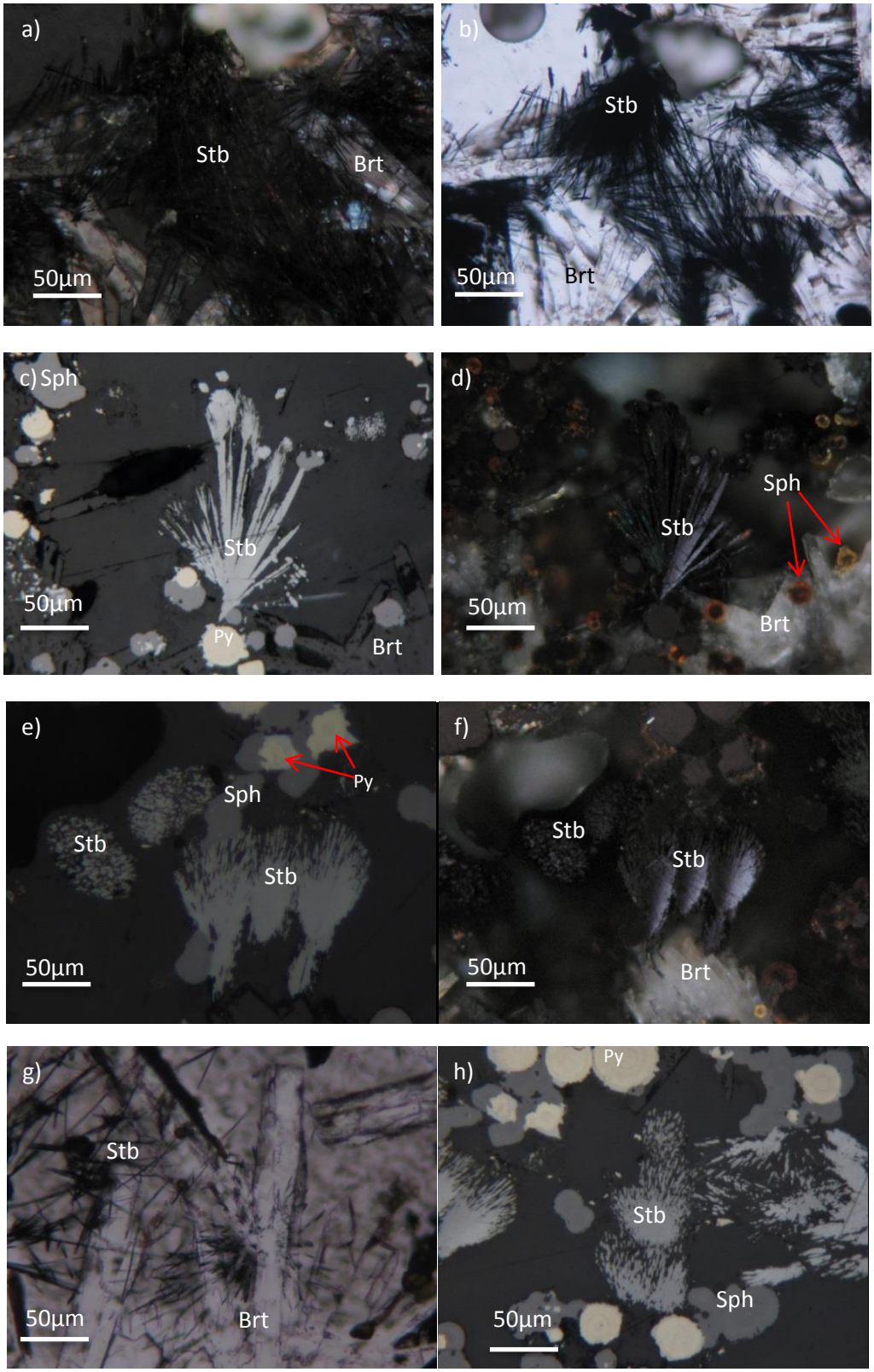
a)
Stb
Brt
50μm
b)
Stb
50μm
Brt
c) Sph
Stb
50μm
Py
Brt
d)
Sph
Stb
50μm
Brt
e)
Py
Sph
Stb
Stb
50μm
f)
Stb
Stb
50μm
Brt
g)
Stb
50μm
Brt
h)
Py
Stb
Sph
50μm

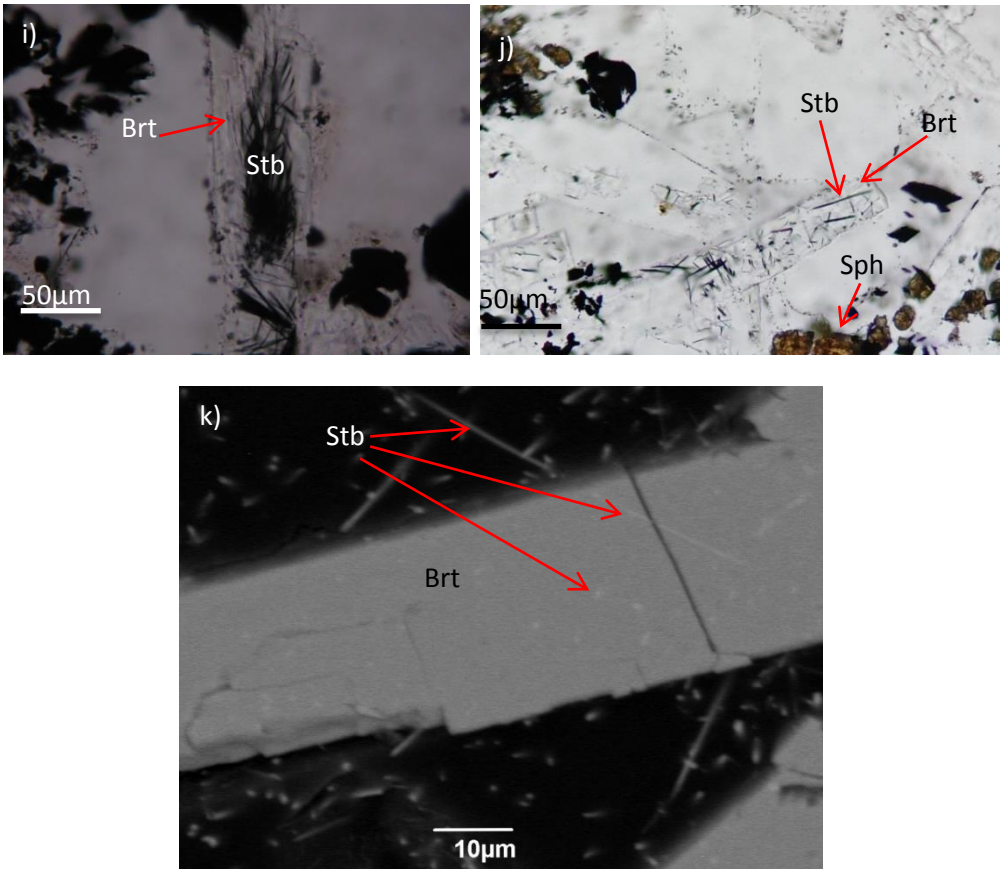

Figure 34: a) Reflected light crossed Nickols photomicrograph of needle-like aggregates of Stibnite in a barite Matrix. b) Same with a) but under transmitted light. c), d), e), f), h) Dendritic Stibnite intergrowths with Pb-Sb-Sulfosalts and microglobular textures. The microglobular textures appear as the result of sheer cross section of the needle-like crystals. g), i), j) Stibnite with barite intergrowths. And especially in j) Stibnite appears to be inside barite as inclusions as it seems it doesn't cut the edges of the host barite crystal. k) Back-scatter image of stibnite intergrowths inside Barite crystals, showing co-precipitation of stibnite and barite.

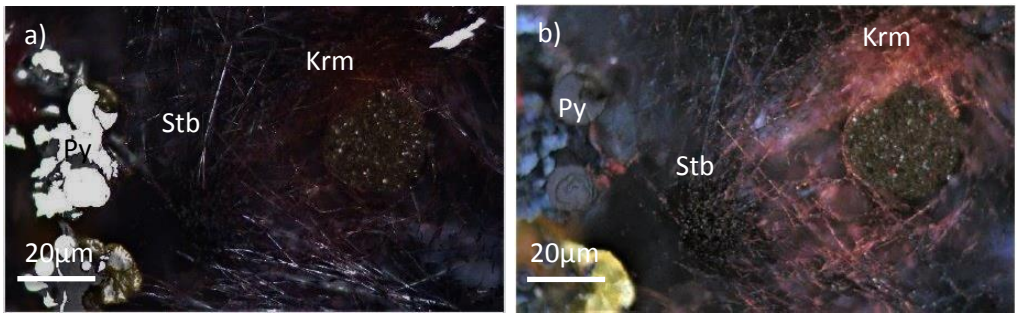

Figure 35: a) Reflected light parallel Nichols photomicrograph of needle-like Stibnite transiting to kermesite. b) Same with a) but in crossed Nichols. Note the intense red internal reflections of kermesite. (Photomicrographs taken from Zigkinoglou 2020).

As-sulfides (As-sus): The As-sulfides in the OAsL approximate the composition of orpiment and realgar phases. They have been identified as globular-colloform, filamentous, massive and as amorphous biomorph-like structures. Under reflected

light with crossed Nichols they display intense orange, yellow and red internal reflections.

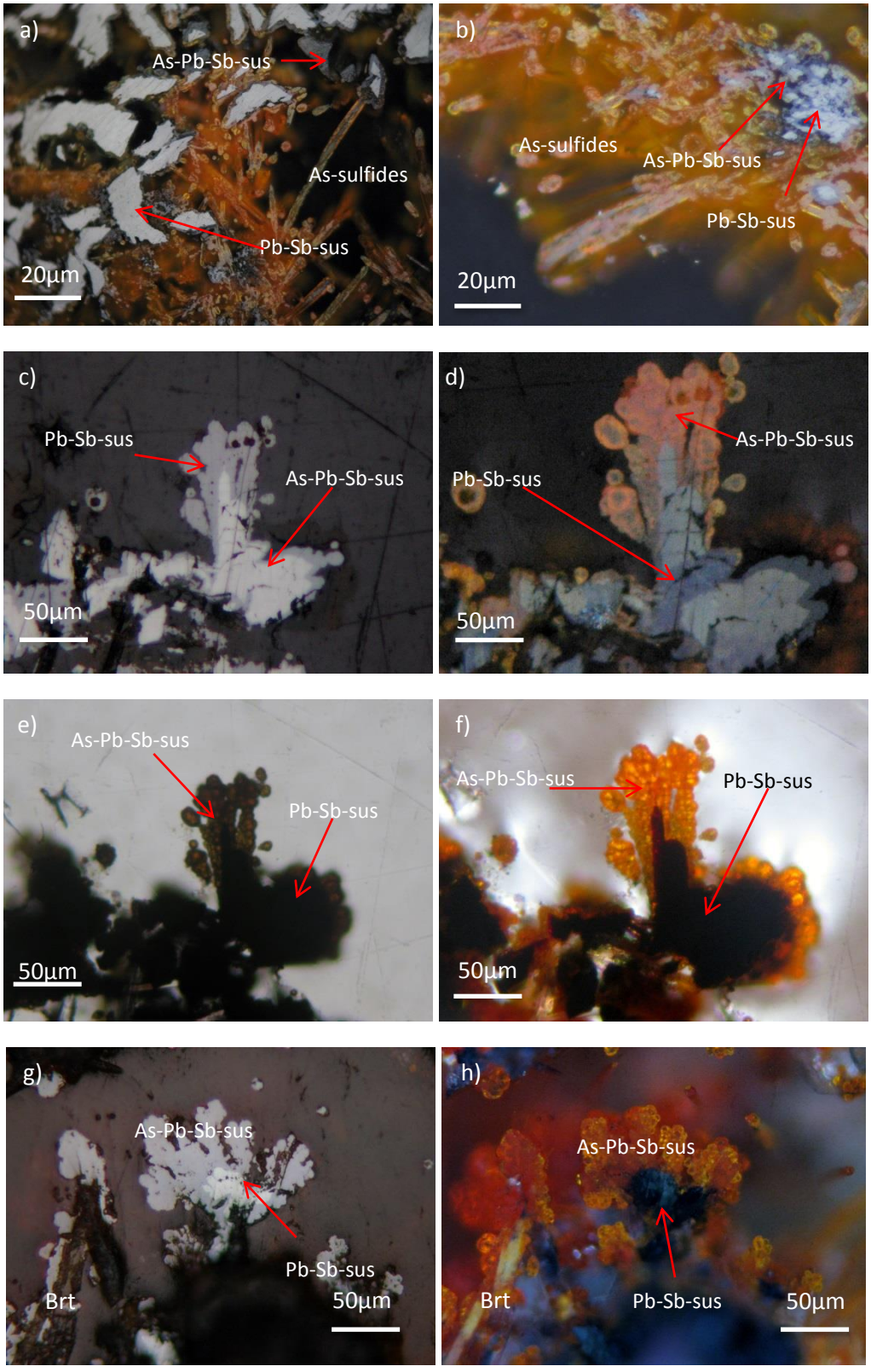

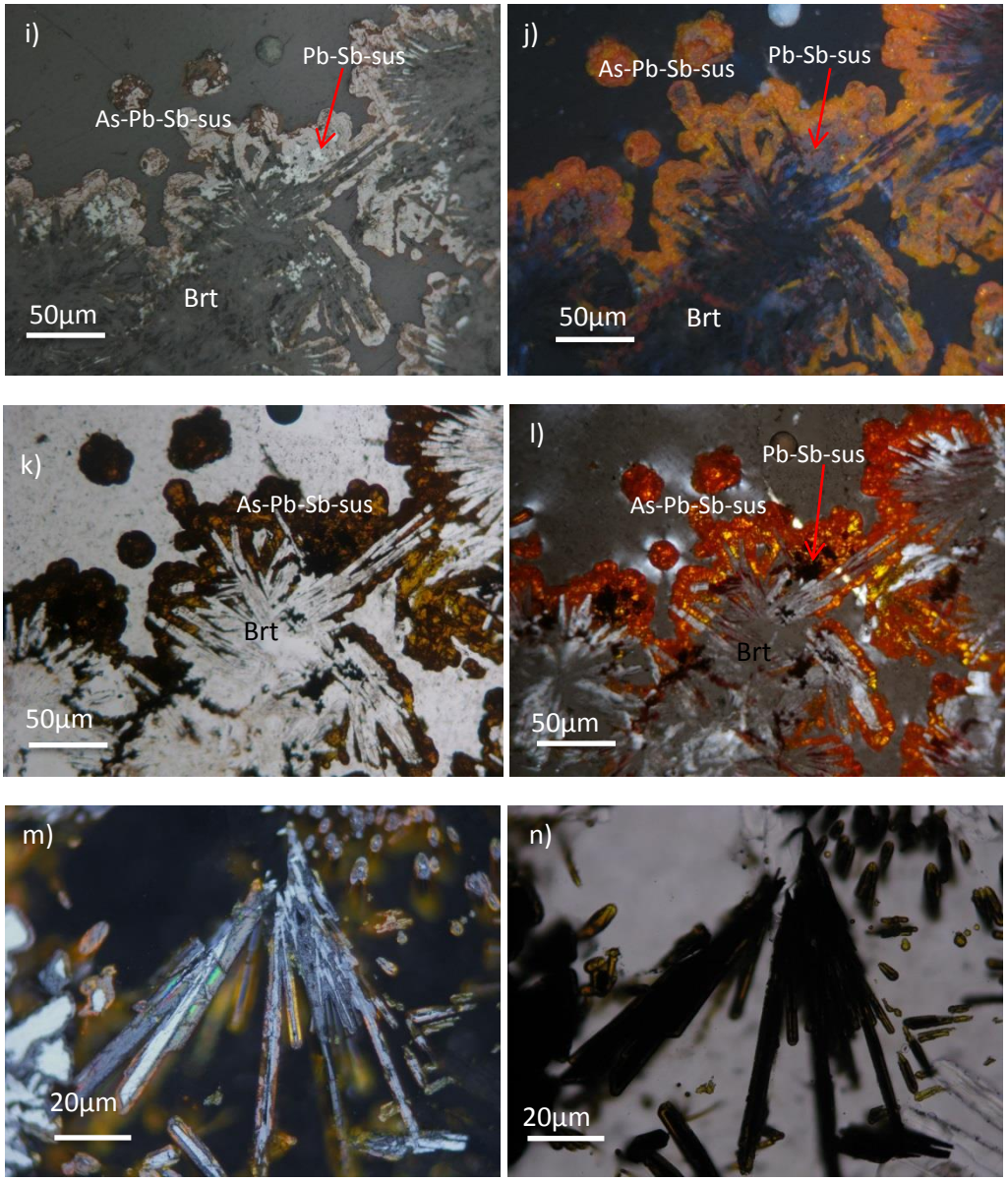

Figure 36: a), b), c), d) Reflected light photomicrographs of As-Pb-Sb- sulfosalts overgrowing Pb-Sb-sulfosalts related with amorphous As-sulfides in a) and b). Note the globular textures with orange internal reflections of the As-Pb-Sb sus in c) and d) and the strong bluish-greyish anisotropy of the Sb-Pb-sus display in d). e), f), g), h) Complex intergrowths of As-Pb-Sb-sus and Sb-Pb-sus overgrowing the outer wall consisting of barite rosettes aggregates (e) and f) under parallel and crossed Nichols reflected light respectively and g), h) under transmitted light; g: parallel Nichols, h: crossed Nichols).

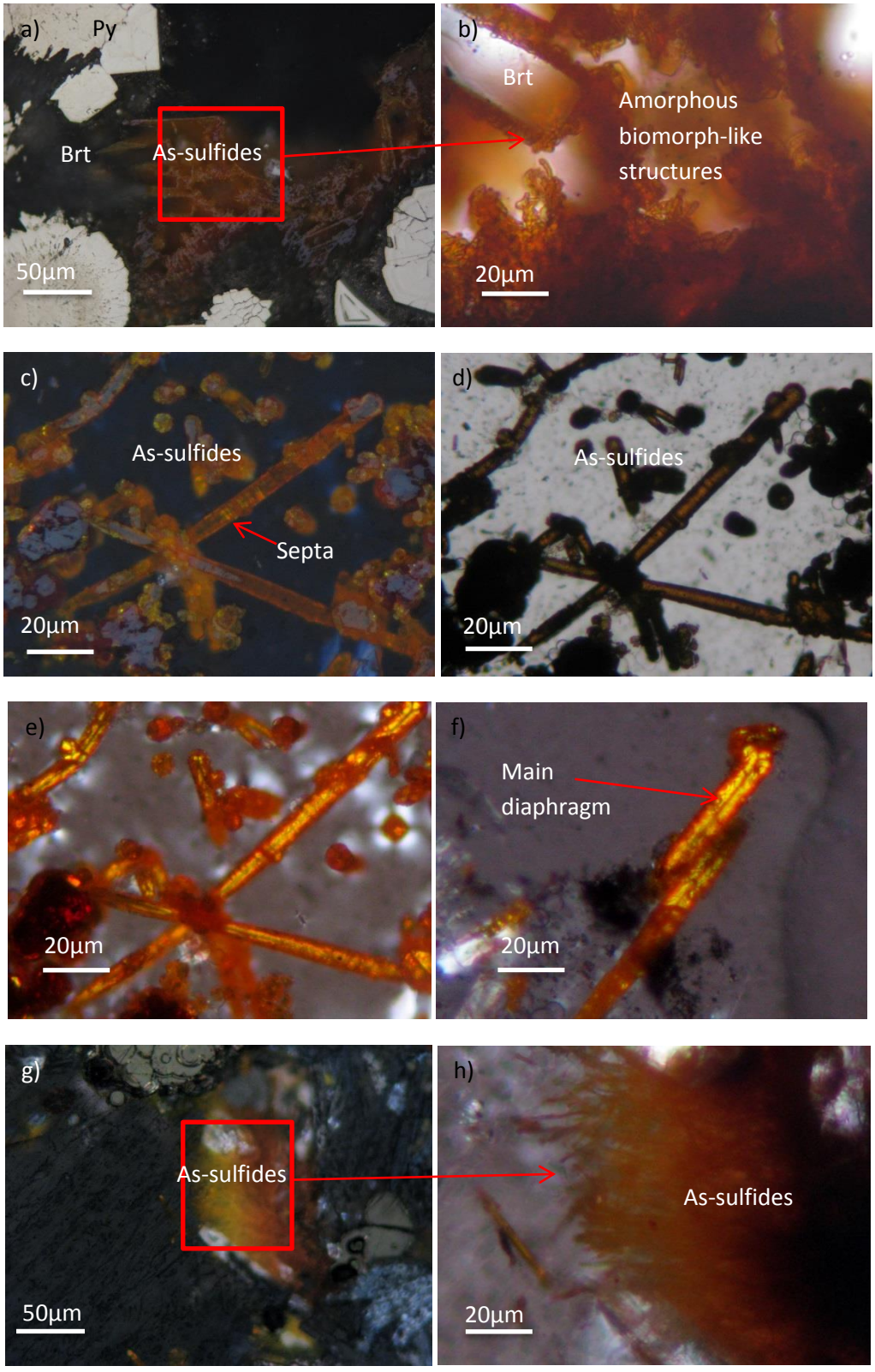
a)
Py
Brt
As-sulfides
50μm
b)
Brt
Amorphous
biomorph-like
structures
20μm
c)
As-sulfides
Septa
20μm
d)
As-sulfides
20μm
e)
20μm
f)
Main
diaphragm
20μm
g)
As-sulfides
50μm
h)
As-sulfides
20μm

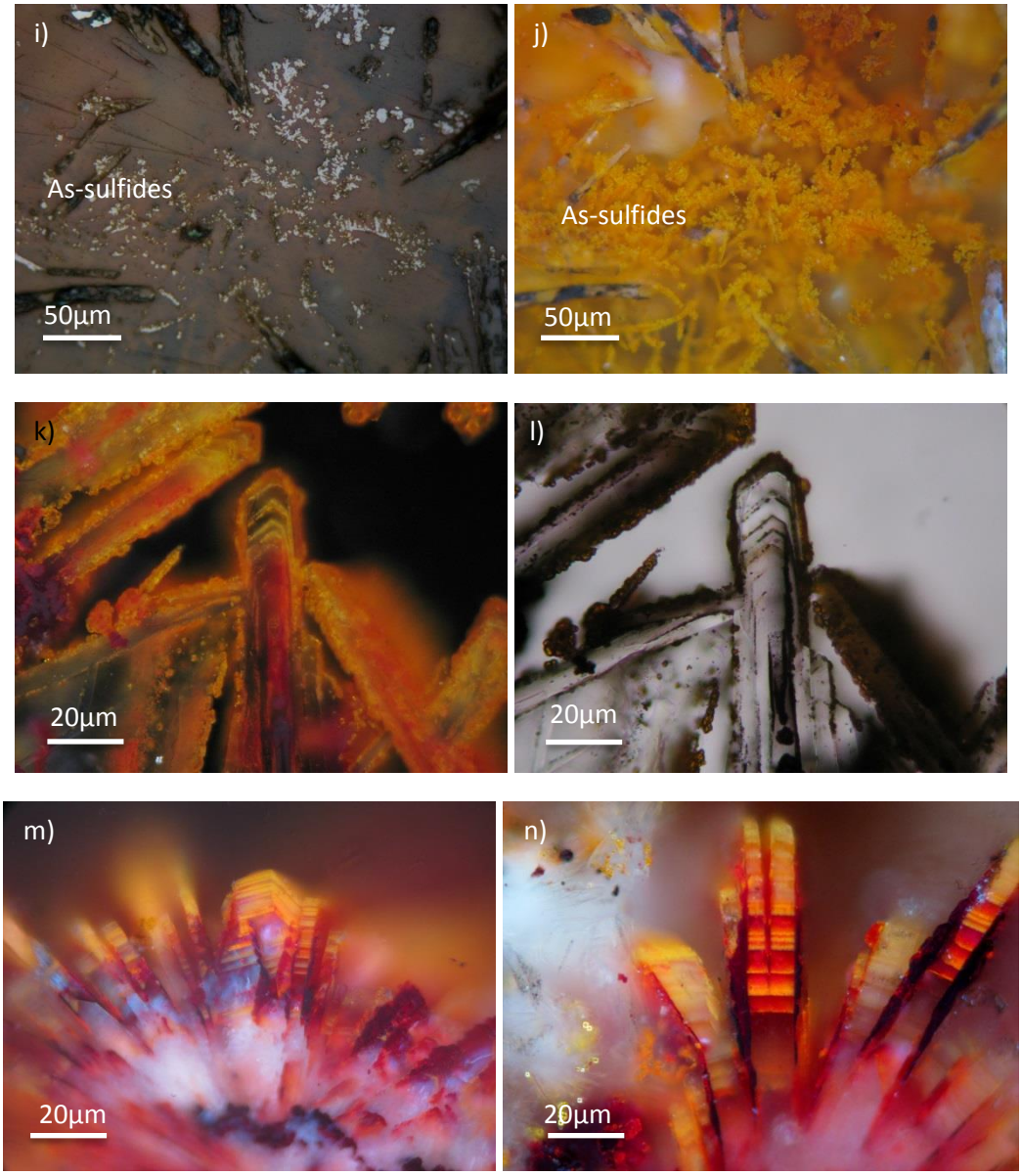

Figure 37: a) Reflected light photomicrograph of As-sulfides with strong orange internal reflections overgrowing barite and Py0, Py1 and Pb-Sb-sus. b) Zoomed photomicrograph of a) under transmitted light revealing filamentous biomorph-like structures. c) Filamentous As-sulfides with elongated core-body and spherical apex under reflected light. d) Same with c) but under transmitted light. Visible septa are identified as well at c). Also a metallic nature filament-core is observed. e), f) Transmitted light crossed Nichols photomicrograph of As-sulfides highlighting their metallic core. g) Filamentous assemblage of As-sulfides with orange internal reflections under reflected light crossed Nichols. h) Zoomed photomicrograph of g) under transmitted light with crossed Nichols. i), j) Dendritic textures of As-sulfides with strong internal reflections, related with barite crystals. k) Zonal barite related with orpiment-like and realgar-like intergrowths under reflected light with crossed Nichols. l) Same with k) but under transmitted light. Note that the red realgar-like intergrowths occur almost entirely in the core of barite while the orpiment-like are located at the edges. This zonation might indicate co-precipitation of barite with As-sulfides. m), n) Relfected light crossed Nichols photomicrographs of zonal barite related with As-sulfides.

Fe-Oxides: Fe-Oxides usually occur in the most outer parts of the chimney were sulfide minerals contact sweater, whereas there are a few cases in which they appear in the more centric parts. They typically form around the oxidized mineral, but in rare occasions the original mineral has been fully disseminated. They exhibit a variety of colors from brown to red and they resemble biomorph-like structures. Their chemical composition remains unidentified as there is no record of analytical studies on them.

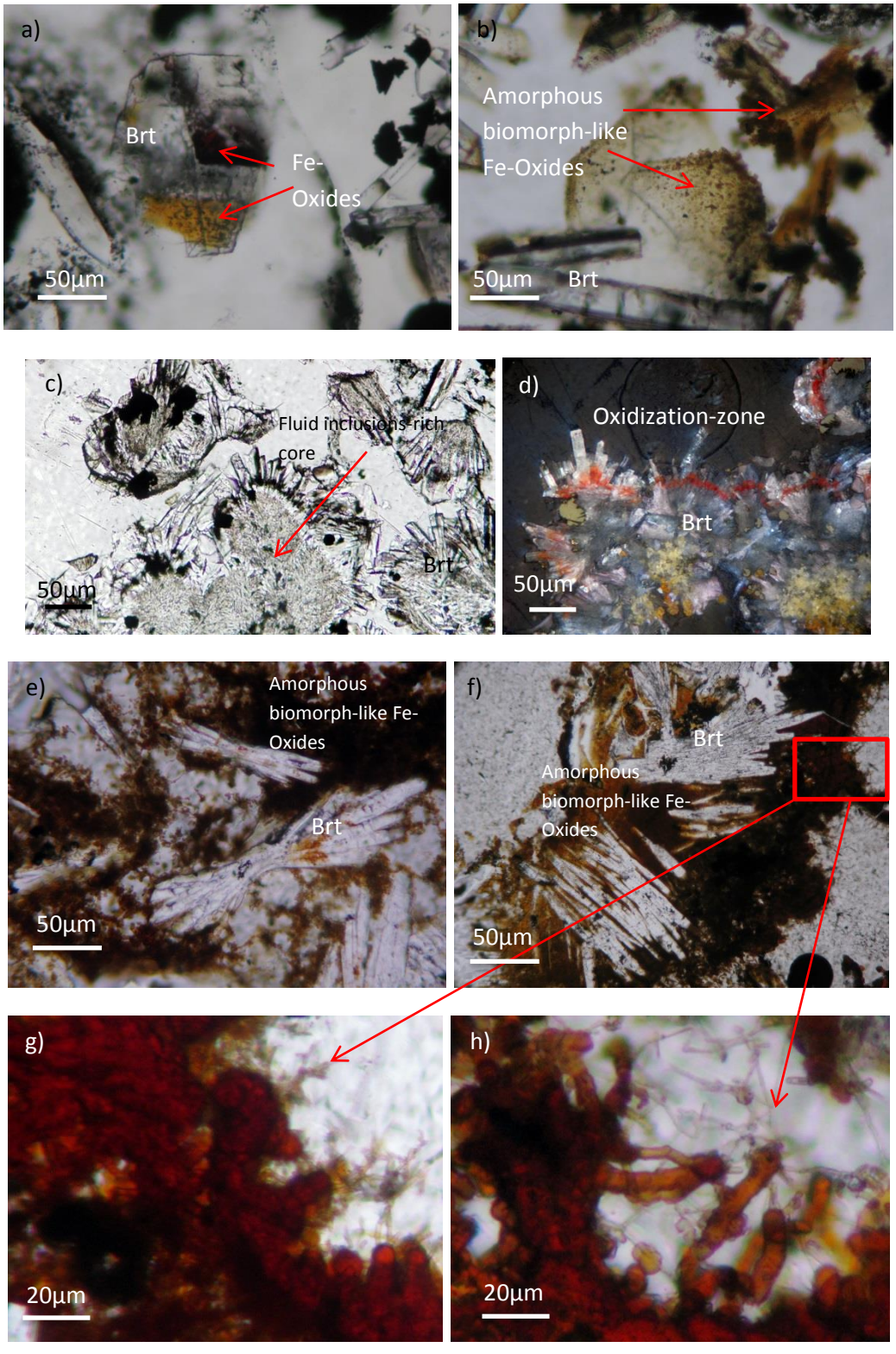

Figure 38: a) Fe-oxides, probably Hematite, overgrown by later barite crystal. b) Relics of primary sulfide phase after oxidization processes. c), d) Fe-Oxides derived from primary sulfides overgrow barite rosette aggregates creating an oxidization zone on the barite crystals. Note the layering of Barite with a rich in fluid inclusions core that evolves into clear crystals that are covered with the Fe-Oxides c) under reflected light with crossed Nichols and d) under transmitted light). e), f) Fe-oxides with brown to red colors associated with plumose barite aggregates. e), f) Zoomed photomicrograph of d) under transmitted light. Biomorph-like structures are observed with a globular red core transiting to brown-orange filamentous phases. Notice how the filamentous phases interrogate with each other creating branches. Also smaller filamentous phases are identified.

8.3 Paragenetic sequence of the ISSC

The in depth observation and description of the mineral assemblages in the ISSC alongside the very detailed previous studies such as Zegkinoglou (2020), have led to the result that extended zone refinement controlled the system. Evidence for that claim comes from the textural variations and the changes in the minerals compositions in the different zones of the chimney. Specific in the ISSC there have been three main mineral deposition events: the Pyrite stage, the Zn-Pb-Sb low temperature stage and the Fe-Zn-Pb-Cu high temperature stage. Additional, an early mineralization stage of anhydrite and barite that constructed the hydrothermal chimneys can be assumed.

8.3.1 Early sulfate stage

The formation of an SMS deposit consisting of hydrothermal chimneys requires an early stage mineralization of sulfate minerals that formed as the result of mixing cold seawater with hot hydrothermal fluids. In the majority of the situations those primary minerals are anhydrite and barite that are typical in white smokers. Those two minerals act as a protective wall that doesn't allow the cold seawater to infiltrate the chimneys. This will let the hot fluids to circulate the chimney without losing their temperature and will finally lead to the precipitation of metal-bearing minerals. Textural evidence from Kolumbo chimneys and along the simultaneous absence of anhydrite and prevalence of barite show that the first wall was constructed by anhydrite that later dissoluted into barite. On that primary sulfate wall ore-forming mechanism started to create the SMS style mineralization. The constant presence of seawater in the system makes it possible for barite to precipitate to almost every stage through-out the chimneys zones.

8.3.2 Pyrite stage

Pyrite as the most abundant sulfide mineral exhibits a great textural variation. As seen in previous chapters there have been identified four different pyrite generations (Py0, Py1, Py2, and Py3) with Py0 predating the other types as the product of replacement of recrystallized primary anhydrite and minor barite. Pyrite 1 in turn predates Py2 and Py3 as it seems to be the primary product of Pyrite precipitation. Pyrite 2 overgrows Py1 as the result of rapid precipitation on the surface of Pyrite 1 and the hydrothermal fluid and/or from Couple Dissolution-Repricipitation (CDR) processes (Zegkinoglou 2020). Pyrite 3 that covers Py2 and Py1 is also a product of recrystallization of Pyrite 1. Marcasite participates in both Pyrite and Fe-Zn-Pb-Cu stage in the form of intergrowths with pyrite, galena, sphalerite and chalcopyrite.

Marcasite is never present in intergrowths with Pb-Sb-sulfosalts. Inclusions of sphalerize, galena and Pb-Sb-sulfosalts are common in pyrite.

8.3.3 Zn-Pb-Sb stage

Based on textural observations after the Pyrite stage mineralization there are other two different temperature-depending stages. One of low temperatures characterized by the presence of Pb-Sb-Sulfosalts alongside sphalerite, pyrite and rarer galena and one of high Temperatures consisting usually in the form of intergrowths of marcasite, galena, sphalerite and chalcopyrite. In the first one sphalerite occurs as rims around pyrite and in other occasions replaces pyrite. While the Pb-Sb-sus cross-cut both minerals. This paragenetic sequence is found in areas inside the chimney where the system wasn't well insulated and therefore the temperature remained relatively low. The high concentration of Tl in the sulfosalts (Zegkinoglou 2020) can work as an indicator for low precipitation temperatures. In this stage is also notably the presence of barite.

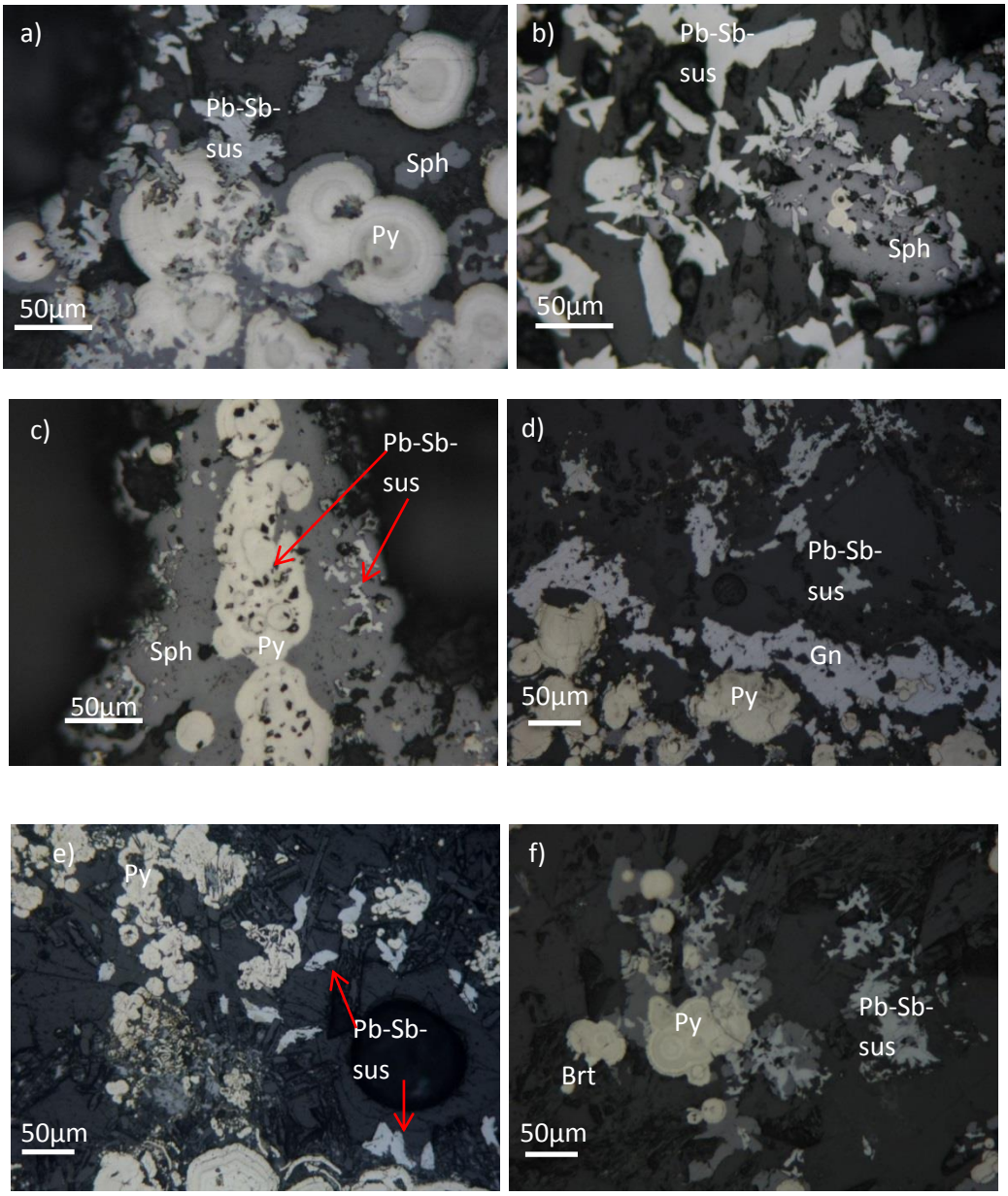

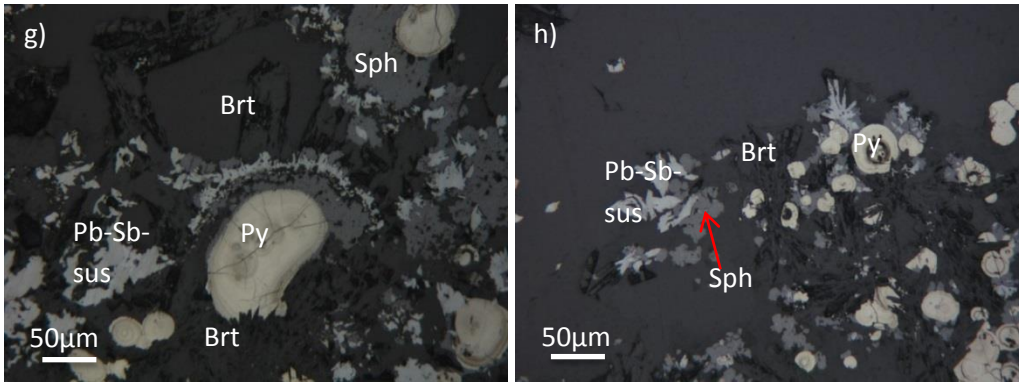

Figure 39: Paragenetic mineral sequence at relatively low temperature conditions. Note that Sphalerite overgrows primary pyrite and in occasions Galena and that the Pb-Sb-sus cross-cut all the other phases or occur as inclusions (Figure 36 c)). Barite crystals happen to be the matrix of this paragenesis as well.

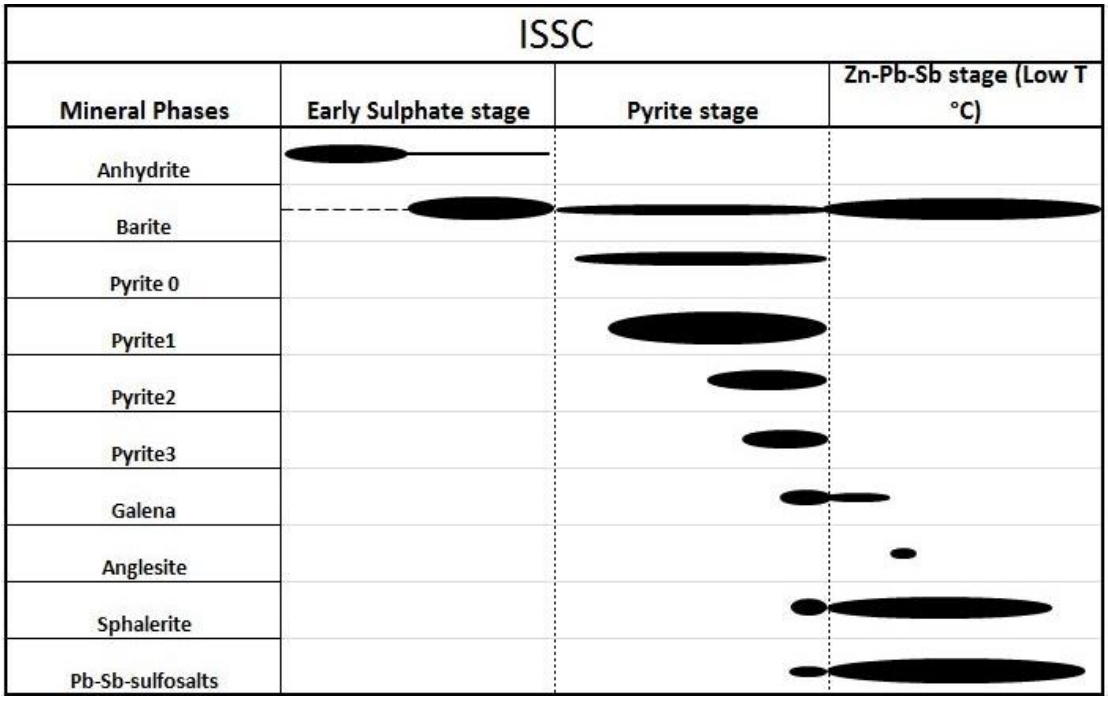

Figure 40: Simplified paragenetic sequence of the studied samples from the ISSC for the low temperature conditions. The sequence is classified in two different successive depositional stages. Modified by Zegkinoglou (2020).

8.3.4 Fe-Zn-Pb-Cu stage

A high temperature paragenesis has also been observed that is characterized by the presence of chalcopyrite (>250 °C). This mineral assemblage commonly occurs in well insulated conduits. This insulation is typically achieved by a µm thick marcasite layer that overgrows pre-existing pyrite, allowing high temperature fluids to pass through them and precipitate complex intergrowths. At these sulfide rich conduits, barite is almost never present revealing that in this stage there is absent of seawater.

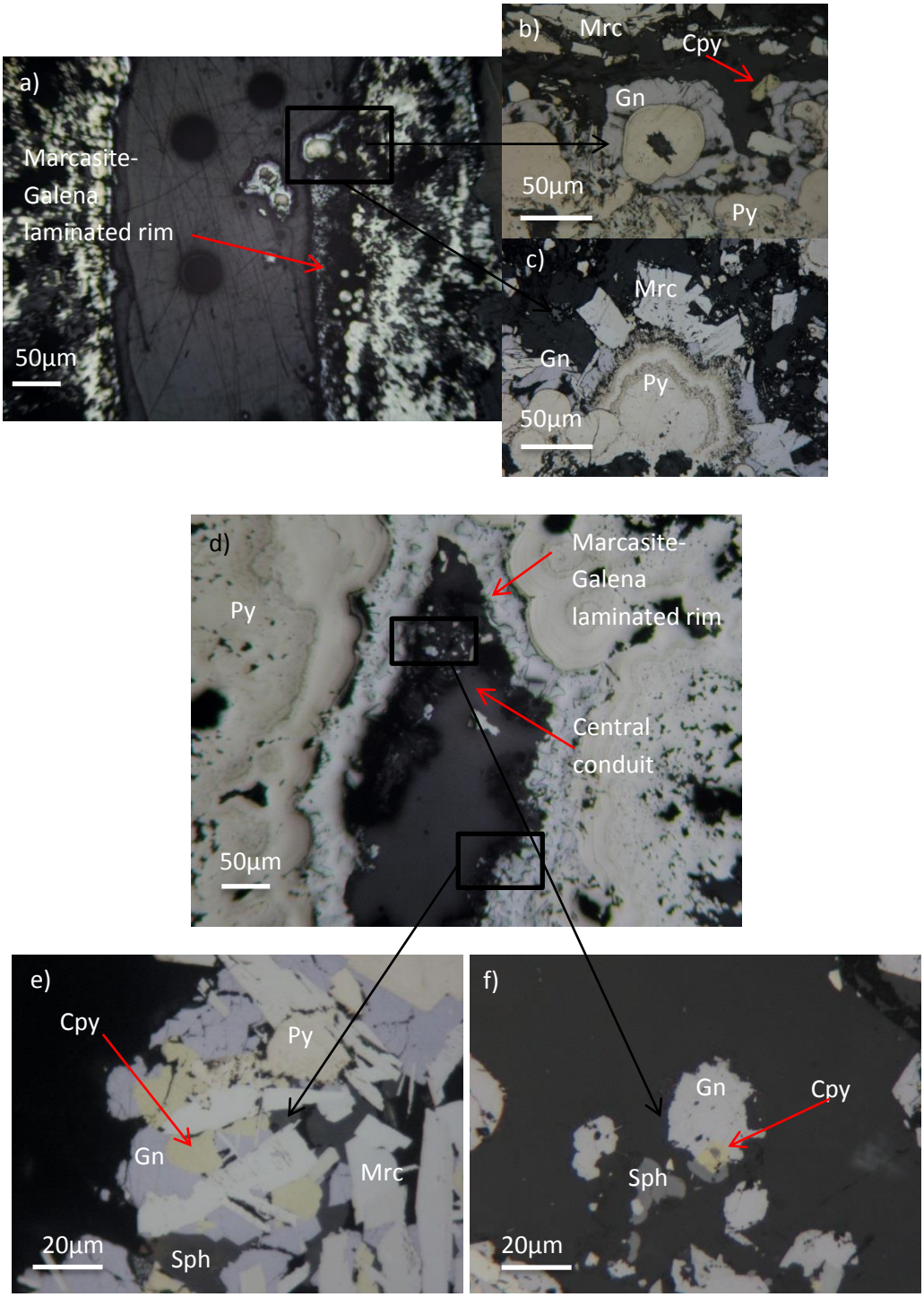

Figure 41: a) Example of hydrothermal conduit covered by a marcasite and galena insulating wall allowing temperature to rise for the High-T paragenesis. b), c) Complex sulfide intergrowth grains consisting of Pyrite 2, marcasite, sphalerite, galena and chalcopyrite.

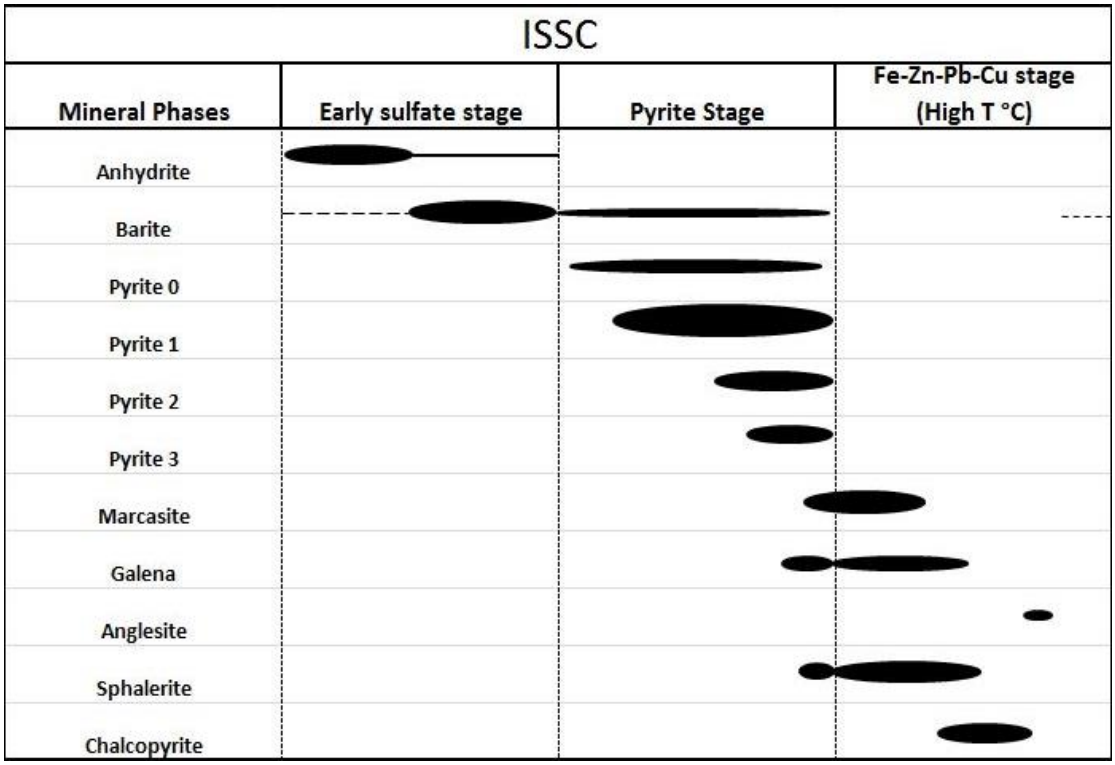

Figure 42: Simplified paragenetic sequence for the studied samples from the ISSC for the high temperature conditions in the well-insulated conduits, classified in two different depositional events. Modified by Zegkinoglou (2020).

8.3.5 Paragenetic sequence of the OAsL

The OAsL covers the most outer parts of the chimneys and it's defined by an orange-yellow color due to high As concentrations. Barite is precipitated throughout this sequence too as textural evidence suggests so. After the barite formation, a smaller in volume compared to that of the ISSC, pyrite mineralization takes place mainly consisting of Py1 that is locally overgrown by Py2. Following that, a second Pb-Zn-Sb-As stage precipitates. Galena seems to be the starting point of that stage as it overgrows pyrite and in turn is overgrown by Pb-Sb-sus. These sulfosalts are often coverd by As-Pb-Sb-sulfosalts that transit to stibnite. The last phase that marks the end of this stage is As-sulfides that overgrow around Pyrite 1 and barite rosette aggregates, blades and laths an in cases stibnite. Often they co-precipitate with barite giving it strong internal reflections and rarer they create impressive zonal barite crystals.

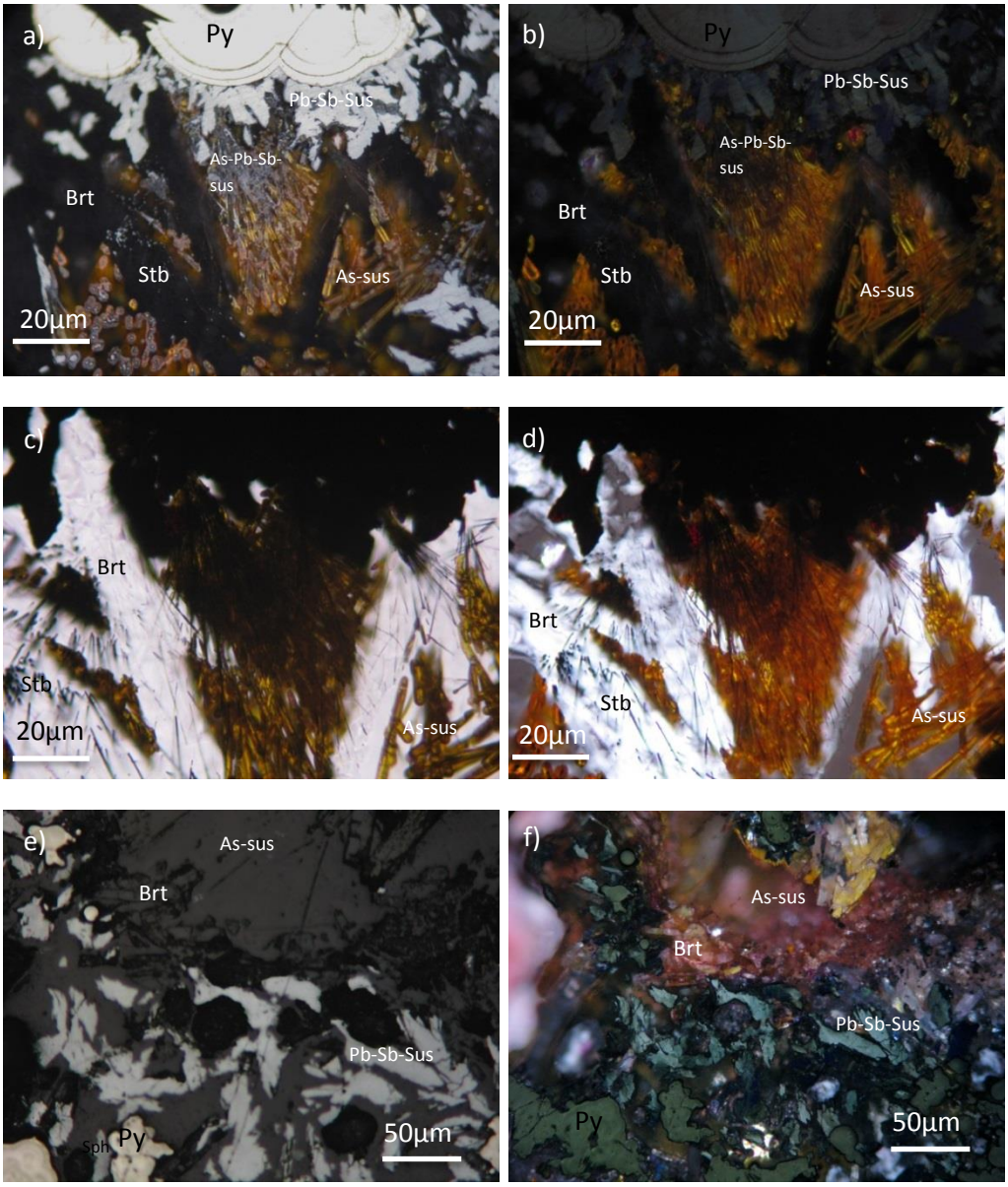

Figure 43: a), b), c), d) Photomicrographs showing the complete paragenetic sequence of the OAsL. Colloform Py1 is overgrown by plumose Pb-Sb-sus which in turn are overgrown by As-Pb-Sb sus. The later transit to stibnite needle-like crystals (identified easier in c), d)) that are covered by As-sulfides. The entire seguence is controlled by the barite mineralization. e), f) Globular pyrite and anhedral sphalerite crystals overgrown by plumose Pb-Sb-sus that are in turn overgrown a barite wall with As-sulfides intergrowths (red internal reflections).

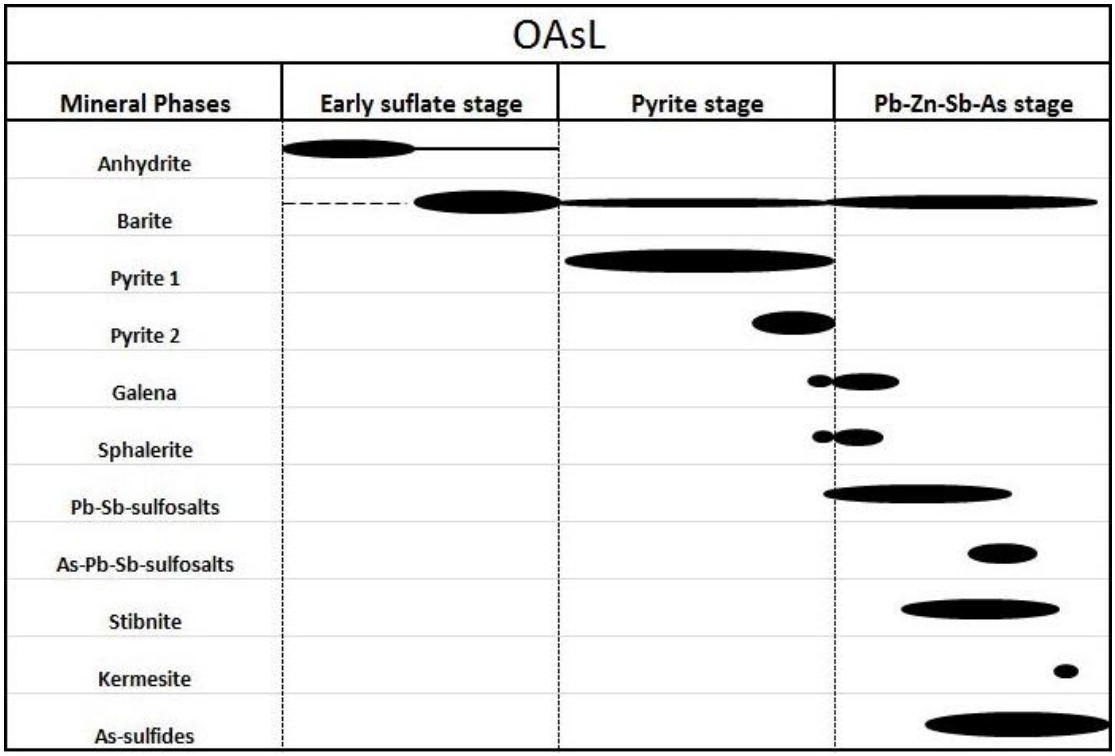

Figure 44: Simplified paragenetic sequence for the studied samples from the OAsL, categorized into three different mineralization stages. Modified by Zegkinoglou (2020).

8.4 Energy Dispersive Spectroscopy (EDS) data

A total of fifteen (15) major element analyses were conducted with the use of SEM coupled with EDS to determine the geochemistry of Barite crystals. These measurements revealed that small concentrations of elements such as Sr, Zn, Pb, Fe and As are possible to be contained in barite. Concentrations of Sr in barite are very common as it is present in high concentrations in seawater and also barite forms a solid-solution series with celestine ($SrSO_4$). The existence of solid micro-inclusions in barite crystals might also be able to explain the small concentrations of Zn, Pb, Fe and As. The combination of primary solid-micro inclusions and the small concentrations of metals indicate that barite is in equilibrium with the ore formation. Grains rich in Ag content have also been identified in the cracks between barite and As-sulfide, showing that barite might be able to trap that way metals and metalloids.

Sample	Spectrum	O	S	Ba	Sr	Fe	Zn	Pb	As
SB-3-A1	1	34.90	14.93	47.55	3.12	-	-	-	-
	2	36.36	15.33	46.44	1.87	-	-	-	-
	3	34.17	14.00	48.82	3.01	-	-	-	-
	4	33.12	13.37	51.21	1.53	-	0.77	-	-
	5	20.78	15.89	61.54	-		1.79	-	
	6	18.72	17.00	61.15	-	2.03	0.06	0.96	0.07
	7	19.58	16.46	62.25	-	1.01	0.11	0.6	-
	8	19.55	16.1	63.73	-	-	0.61	-	-
	9	30.32	14.52	53.8	-	-	1.11	0.25	-
	10	19.38	16.44	63.29	-	-	0.88	-	-
SB-3-A2	11	21.98	16.71	60.05	2.33	0.82	-	-	-
	12	21.56	16.08	62.37	-	-	-	-	-
NA-014-003	13	22.3	15.28	59.85	-	-	2.58	-	-
SB-7-A2 NEW	14	25.26	14.05	60.04	-	-	-	0.66	-
SB-10-A	15	24.00	14.77	58.96	-	1.59	-	0.55	0.13

Table 3: Major elements wt% concentration of barite crystals as it transcripts from SEM coupled with EDS analyses.

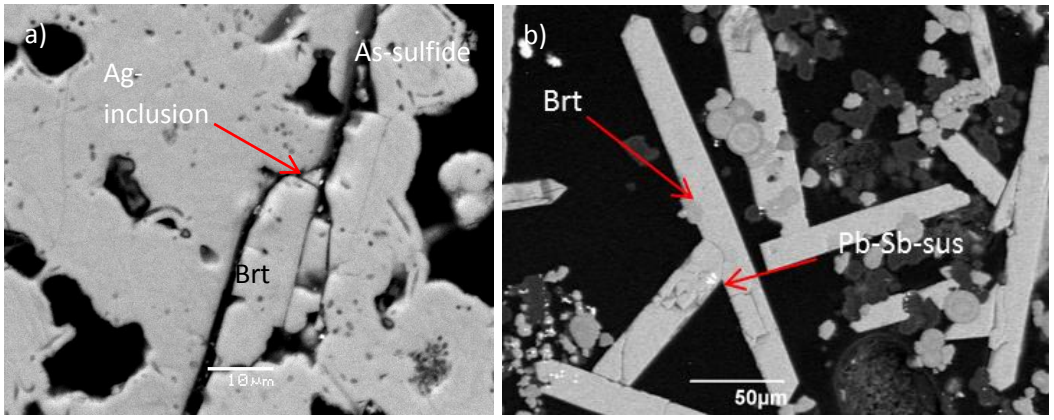

Ag-Incluion					
Sample		count	S	Ag	As
Sb-3-A2		1	20.92	51.57	26.83

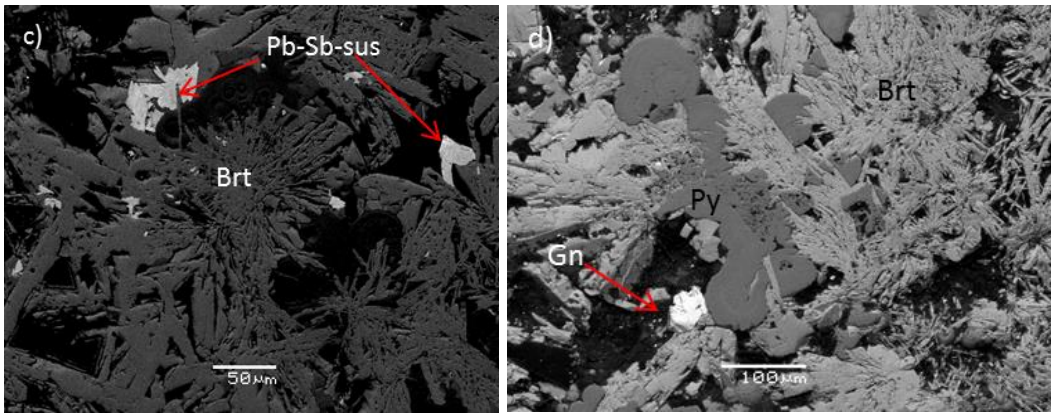

Figure 45: a) Barite crystals overgrown by As-sulfides with solid micro-inclusions rich in Ag. b) Big open-space barite blades and laths with Pb-Sb-sus inclusions. c) Typical rosette barite aggregates related with Pb-Sb-sulfosalts. d) Barite rosette aggregates related with galena cross-cutting pyrite.

8.5 Suggested Chimney growth model

Taking into consideration the before mention observations and the previous work, the following growth model has been proposed.

A

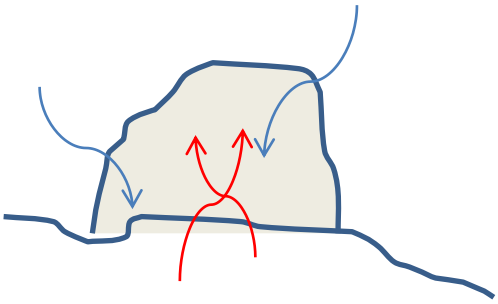

B

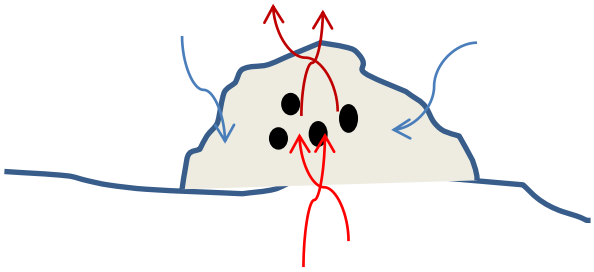

C

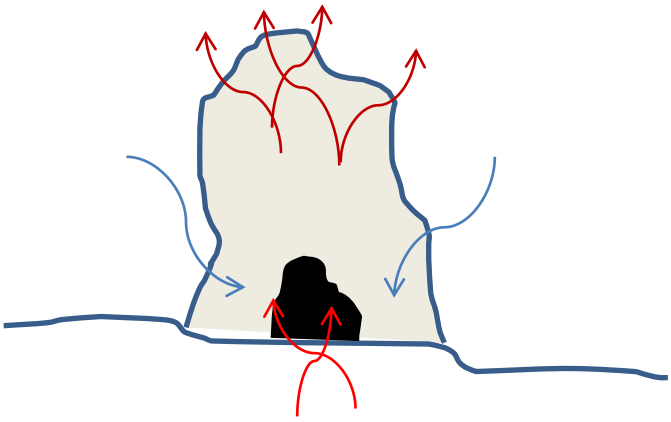

D

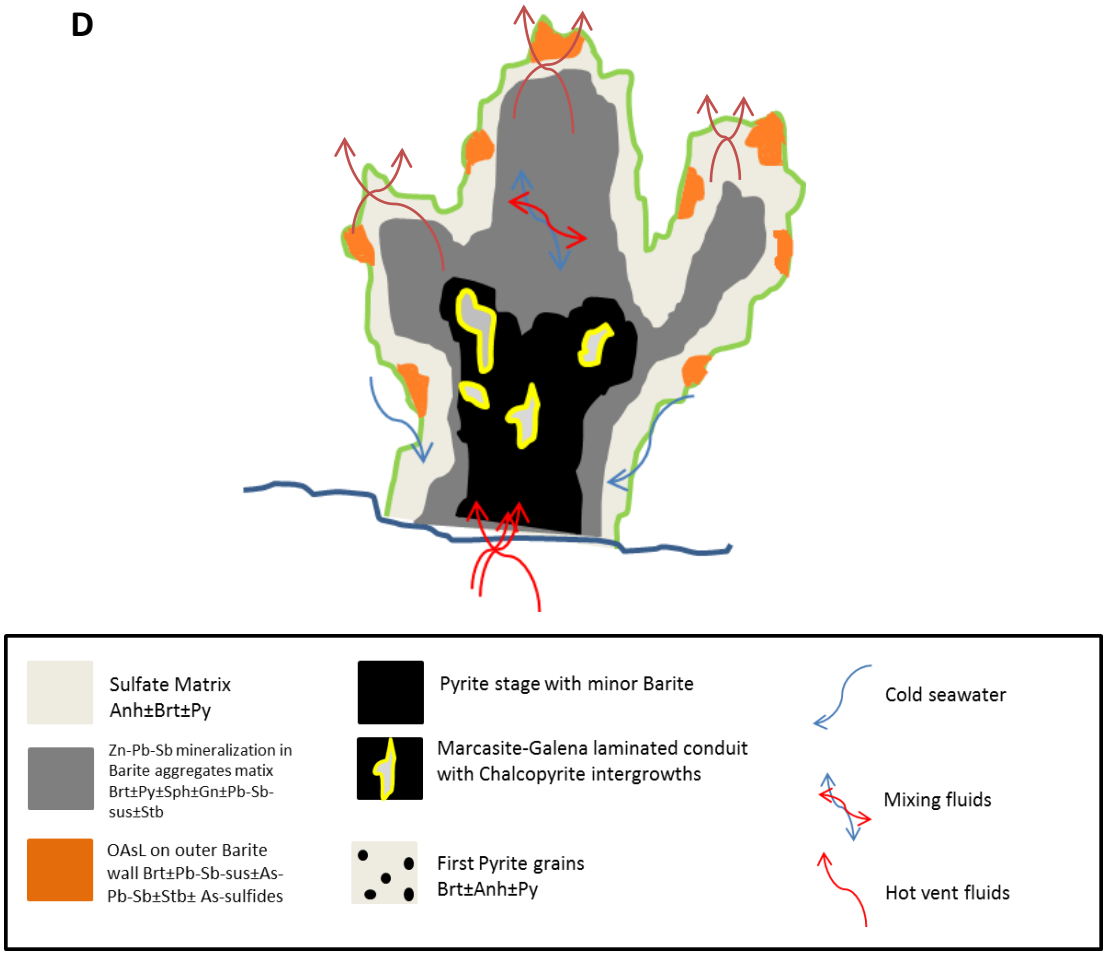

(Modified by Berkenbosch et al.2012)

A: At the first stage where the temperatures are still low, small anhydrite-barite mounds are formed with small concentrations of pyrite crystals. These first sulfate walls will be the stepping ground in which the sulfide minerals will form.

B: As the chimney grows it becomes more compacted making it possible for higher temperature fluids to circulate inside it. These fluids will dissolute and recrystallize the first sulfate phases and at this point is where the first pyrite grains will start precipitating.

C: The system's continuous hydrothermal activity has as a result repeatedly pulses of sulfide precipitation. These sulfide minerals will be assembled into the core of the chimney through zone refinement processes.

D: As the chimney grows higher temperatures are reached allowing marcasite and galena to form laminated rings around the chimney's conduits. In these rims complex

intergrowths of marcasite, galena, sphalerite, chalcopyrite and minor pyrite will start to from. At the outer parts where the seawater is present Pb-Sb-sulfosalts, sphalerite and minor pyrite characterize this (Zn-Pb-Sb) stage, while barite confines the whole system. As-sulfides and barite co-precipitate, creating intergrowths that are covering the surface of the chimney, as mixing of hot hydrothermal fluid and cold seawater.

9 Conclusions

In this current thesis Optical Microscopy and SEM were used in order to determine the different barite petrographic types, their distribution and their relationship with the other sulfate-sulfide minerals. Also, to understand the main paragenetic sequences for different zones of the chimney and finally present a growth model. There have been observed at least four different generations of barite and each one of those generations displays a great variety of textures.

The first generation is the one that replaces the primary anhydrite crystals that started to construct the chimney. This generation consists of large (mm) barite aggregates of laths and blades and rarer in recrystallized mosaic structures. The first pyrite grains are deposit on that early barite wall.

The second generation to precipitates in the pyrite stage consisting of mainly big singular barite laths and blades and topically in the form of rosette and plumose aggregates in the open conduits of ISSC. Moving to the outer parts from the core this generation is usually covered/replaced by sphalerite.

The third barite generation starts to precipitate at the late pyrite stage and is often related with galena, sphalerite and Pb-Sb-Sulfosalts inclusions inside pyrite crystals. This third generation dominates the outer parts of the ISSC and the Zn-Pb-Sb mineralization stage exhibiting a great textural variety. The most common petrographic types it displays are rosette, plumose and dendritic aggregates, needle-like structures and complex intergrowths created by laths and blades.

The fourth generation reconstructs the outer barite wall of the chimney where the As-sulfides will mineralize. This outer wall consists of big open-space barite laths and blades or from plumose and rosette aggregates. Needle-like structures have also been observed. The existence of zonal barite crystals related with As-sulfides intergrowths indicates that barite mineralization is continuous throughout this stage as well. In the parts of the chimney where OAsL isn't developed, barite is associated with Fe-Oxides and amorphous Fe-biomorph-like structures.

In general, barite increases both in concentration and size in the outer parts of the chimney relatively with the core. Also, the same applies in textural variety and complexity. This might be explain by the fact that in the outer parts the participation of water is greater, thus the fluids are oversaturated with respect to Barite.

The large individual crystals are related with pyrite while rosette and plumose aggregates are related with galena, sphalerite and Pb-Sb-sulfosalts in the ISSC. Also, barite blades and laths are often associated with stibnite intergrowths. At the OAsL plumose and rosette aggregates are associated with As-Pb-Sb sulfosalts and blades and laths are associated with As-sulfides.

Two different paragenetic sequences have been identified in the ISSC one containing pyrite, galena, anglesite, sphalerite and Pb-Sb-Sulfosalts in a barite matrix and one of high temperatures containing pyrite, marcasite, galena, sphalerite and chalcopyrite. At the OAsL the paragenetic sequence contains Pyrite, Pb-Sb-sulfosalts, stibnite, kermecite, As-Pb-Sb-sulfosalts and As-sulfides. Barite precipitates through all the mineralization stages except for (Fe-Zn-Pb-Cu stage), where the contribution of the barite ingredients is low and the temperatures might be too high for barite to precipitate.

The SEM-EDS analyses identified small concentrations of Sr, Zn, Fe, Pb and As. Zinc was found in the majority of the measurements showing a close relationship between barite and sphalerite. The small primary solid inclusions might be the reason for the observation of these concentrations in barite, proving that barite is closely associated with the main ore stages not only texturally but also geochemically. Also, the occurrence of Ag-inclusions trapped between barite crystals shows another way of ore deposition and further examination needs to be done on that matter.

The chimney start to grow from small sulfate mounds containing mostly anhydrite. As the time passes the primary precipitated anhydrite dissolves and gets replaced by barite mineralization. The first pyrite grains start to precipitate at this stage related with the barite mineralization. As time passes and the system can sustain higher temperatures the ISSC starts to form in the most central parts of the chimney. This stage is characterized by pyrite domination with minor barite precipitation in the form of large individual crystals. At the outer parts of the ISSC where the temperatures are lower the (Zn-Pb-Sb stage) mineralization takes place, characterized by the presence of sphalerite, Pb-Sb-sulfosalts and pyrite in a barite matrix. Marcasite, galena, sphalerite, chalcopyrite and minor pyrite mantle pyrite conduits in the (Fe-Zn-Pb-Cu stage) mineralization in the ISSC. At the last stages in the OAsL As-sulfides, As-Pb-Sb-sulfosalts and stibnite co-precipitate with barite as a product of mixing of hot hydrothermal fluids with cold seawater.

Future Work

As previously mentioned barite is abundant in all of the mineralization stages, therefore it can provide the answer to a lot of unanswered questions for the whole system. Isotopic analyses on barite with the $^{87}Sr/^{86}Sr$ are perfect in order to determine its origin, as it contains very low rubidium content. Interesting enough the primary observed solid and fluid inclusions can show insight about the composition, the salinity, temperature and the pressure conditions of the primary fluids. In order to resolve all these problems microthermometric studies and new analytical technics such as Laser-Ablation-ICP-MS are needed.

References

Ahmad Q., 2018.,The source of metals in the recent polymetallic seafloor massive sulfide mineralization at the Kolumbo arc-volcano, Greece. Master Thesis. Karlsruhe Institute of Technology.

Aloisi, G Wallmann, K., Bollwerk, S.M., Derkachev, A., Bohrmann, G. and Suess, E., 2004., The effect of dissolved barium on biogeochemical processes at cold seeps, Geochim. Cosmochim. Acta, v. 68, p. 1735–1748.

Alt, J. C., Laverne, C., Coggon, R. M., Teagle, D. A. H., Banerjee, N. R., Morgan, S., Smith-Duque, C. E., Harris, M., Galli, L., 2010., Subsurface structure of a submarine hydrothermal system in ocean crust formed at the East Pacific Rise" ODP/IODP Site 1256. Geochem. Geophys. Geosyst. v. 11 (10). DOI: 10.1029/2010GC003144.

John W., Anthony, Richard A., Bideaux, Kenneth W., Bladh, and Monte C., Nichols, Eds., Handbook of Mineralogy, Mineralogical Society of America, Chantilly, VA 20151-1110, USA. http://www.handbookofmineralogy.org/. p. 379.

Arrhenius, G. and Bonatti, E., 1965., Neptunism and volcanism in the ocean, Prog. Oceanogr. v. 3, p. 7–22.

Beaulieu, S.E., Baker T. D., German R. C., Maffei A., 2013., An authoritative global database for active submarine hydrothermal vent fields: Geochemistry Geophysics Geosystems, v. 14(11), p. 4892-4905.

Beaulieu S. E., Graedel T. E. and Hannington M. D., 2017., Should we mine the deep seafloor?, Earth's Futur. v. 5, p. 655–658.

Bellon, H., Jarrige, J., Sorel, D., 1979., Les activites magmatiques egeennes de l' Oligocene a nos jours et leurs cadres geodynamiques. Donnees nouvelles et synthese, Revue de Géologie Dynamique et de Géographie Physique v. 21 (1), p. 41–55.

Berkenbosch, H., de Ronde C. E. J., Gemmel J. B., McNeill A. W., and Goemann K., 2012., Mineralogy and formation of black smoker chimneys from Brothers submarine volcano, Kermadec arc, Economic Geology v. 107(8), p. 1613-1633.

Bernstein, R.E., Byrne, R.H. and Schijf, J. 1998., Acantharians: a missing link in the oceanic biogeochemistry of barium, Deep-Sea Res. I, v. 45, p. 491–505.

Bertram, M.A. and Cowen, J.P. 1997., Morphological and compositional evidence for biotic precipitation of marine barite, J. Mar. Res., v. 55, p. 577–593.

Bishop, J.K.B., 1988., The barite-opal-organic carbon association in oceanic particulate matter, Nature, v. 311, p. 341–343.

Bolze, C.E., Malone, P.G. and Smith, M.J., 1974., Microbial mobilization of barite, Chem. Geol., v. 13, p. 141–143.

Both, R., et al. 1986., Hydrothermal chimneys and associated fauna in the Manus Back-Arc Basin, Papua New Guinea, EOS Transaction American Geophysical Union v. 67(21), p. 489-490.

Breheret, J.-G. and Brumsack, H.-J., 2000., Barite concretions as evidence of pauses in sedimentation in the Marnes Bleues Formation of Vocontian Basin (SE France), Sed. Geol., v. 130, p. 205–228.

Brumsack, H.J. and Gieskes, J.M., 1983., Interstitial Water Trace-Metal Chemistry of Laminated Sediments from the Gulf of California, Mexico, Mar. Chem., v. 14, p. 89–106.

Butterfield, D., Holden, J. F., Shank, T. M., Tunnicliffe, V., Sherrin, J., Herrera, S., Baker E. T., Lovalo D., Makarim, S., Malik , M. A Wirasantosa, S., Hammond, S. R., 2010., Video observations by telepresence reveal two types of hydrothermal venting on Kawio Barat seamount, AGU Fall Meeting Abstracts, v. 2010, p. OSC13C-1236.

Burchfiel, B. C., Papanikolaou D., Pearce, F. D., Royden, L. H., 2018., Crustal development within a Retreating Subduction System: The Hellenides, Geosphere, v. 14, no. 3, p. 1119-30.

Cantner, K. A. 2010., Volcanologic and petrologic analysis of the 1650 AD submarineeruption of Kolumbo Volcano, Greece, Master Thesis. University of Rhode Island.

Cantner, K. and Carey, S., 2014., Integrated volcanologic and petrologic analysis of the 1650 AD eruption of Kolumbo submarine volcano, Greece, Journal of Volcanology and Geothermal Research v. 269, p. 28-43.

Carey, S., Bell, K. L. C., Nomikou, P., Vougiouklakis, G., Roman, C. N., Cantner, K., Bejelou, K., Bournouli, M., and Martin, J. E., 2011., Exploration of the Kolumbo volcanic rift zone, In Bell, K.L.C. & Fuller, S. A. eds. New Frontiers in Ocean Exploration: The E/V Nautilus 2010 Field Season. Oceanography v. 24(1), supplement (2011).

Carey, S., Nomikou, P., Bell., K. L. C., Lilley, M., Lupton, J., Roman, C., Stathopoulou, E., Bejelou, K., Ballard, R., 2013., CO_2 degassing from hydrothermal vents at Kolumbo submarine volcano, Greece, and the accumulation of acidic crater water, Geology v. 41(9), p. 1035-1038.

Cecile, M.P., Shakur, M.A. and Krouse, H.R., 1983., The isotopic composition of Western Canadian barites and the possible derivation of oceanic sulfate d34S and d18O age curves, Can. J. Earth Sci., v. 20, p. 1528–1535.

Chang, L.L.Y., Howie, R.A. and Zussman, J., 1996., Rock- Forming Minerals. Non-Silicates: Sulfates, Carbonates, Phosphates, Halides,5B, Geological Society, London, p. 383

Church, T.M., 1979., Marine barite. In: Marine Minerals, Reviews in Mineralogy, (Ed. M. Burns), v. 6, p. 175–210. Mineralogical Society of America, Washington, D.C.

Connelly, D. P., Copley, J. T., Murton, B. J., Stansfield, K., Tyler, P. A., German, C. R., Van Dover, C. L., Amon, D., Furlong, M., Grindlay, N., Hayman, N., Hühnerbach, V., Judge, M., Le Bas, T., McPhail, S., Meier, A., Nakamura, K., Nye, V., Pebody, M., Pedersen, R. B., Plouviez, ., Sands, C., Searle, R. C., Stevenson, P., Taws, S., and Wilcox, S., 2012., Hydrothermal vent fields and chemosynthetic biota on the world's deepest seafloor spreading centre, Nature Communications v. 3 (620).

Craig, H., 1987., Hydrothermal vents in the Mariana Trough: results of the first Alvin dives, EOS Transaction American Geophysical Union v. 68, p. 1531.

de Ronde, C.E.J., Bakert, E. T., Massoth, G. J., Lupton, J. E., Wright, I. C., Feely, R. A. Greene, R. R. 2001., Intra-oceanic subduction-related hydrothermal venting, Kermadec volcanic arc, New Zealand, Earth and Planetary Science Letters v. 193, p. 359–369.

de Ronde, C.E.J., Massoth, G. J., Baker, E. T., Lupton, J. E., 2003., Submarine hydrothermal venting related to volcanic arcs, Society of Economic Geologists Special Publication v. 10, p. 91–110.

de Ronde, C.E.J., Hannington, M. D., Stoffers, P., Wright, I. C., Ditchburn, R. G., Reyes, A. G., Baker, E. T., Massoth, G. J., Lupton, J. E., Walker, S. L., Greene, R. R., Soong, C. W. R., Ishibashi, J., Lebon, G. T., Bray, C. J., Ring, J. A., 2005, Evolution of a submarine magmatic-hydrothermal system: Brothers volcano, southern Kermadec arc, New Zealand, Economic Geology v. 100(6), p. 1097–1133.

Dean, W.E. and Schreiber, B.C.,1977., Authigenic barite. In: Proceedings of the Deep Sea Drilling Project, Initial Reports, Eds J. Gardner and J. Herring), U.S. Government Printing Office, Washington, D. C. v. 41, p. 915–931.

Dekov V. M., Kamenov G. D., Abrasheva M. D., Capaccioni B. and Munnik F., 2013. Mineralogical and geochemical investigation of seafloor massive sulfides from Panarea Platform (Aeolian Arc, Tyrrhenian Sea), Chem. Geol. v. 335, p. 136–148.

Edmonds, H.N., Michael, P. J., Baker, E. T., Connelly, D. P., Snow, J. E., Langmuir, C. H., Dick, H. J. B., Mühe, R., German, C. R., Graham, D. W., 2003., Discovery of abundant hydrothermal venting on the ultraslow spreading Gakkel Ridge in the Arctic Ocean, Nature v. 421(6920), p. 252–256.

Edwards, K. J., Glazer, B. T., Rouxel, O. J., Bach, W., Emerson, D., Davis, R. E., Toner, B. M., Chan, C. S., Tebo, B. M., Staudigel, H., and Moyer, C. L., 2011., Ultra-diffuse hydrothermal venting supports Fe-oxidizing bacteria and massive umber deposition at 5000 m off Hawaii, ISME J. v. 5, p. 1748–1758.

Ehya, F., Mazraei, S. M., 2017., Hydrothermal barite mineralization at Chenarvardeh deposit, Markazi Province, Iran: Evidences from REE geochemistry and fluid inclusions, Journal of African Earth Sciences v.134, p. 299-307.

European Commission, Study on the EU's list of Critical Raw Materials – Final Report 2020

Ford, H., 2014., Barite in the Ore deposits of western Milos as a possible genetic link between shallow marine and subaerial epithermal mineralization, Master Thesis, Applied and Envrionmetal Geology, University of Leicester.

Fouque, F., 1879., Santorin et ses Eruptions. Masson et Cie, Paris

Fouquet, Y., Von Stackelberg, U., Charlou, J. L., Donval, J. P., Erzinger, J., Foucher, J. P., Herzig, P., Mühe R., Soakai, S., Wiedicke, M., and Whitechurch, H., 1991., Hydrothermal activity and metallogenesis in the Lau back-arc basin, Nature v. 349, p. 778–781.

Fouquet, Y., Charlou, J. L., Von Stackelberg, U., Wiedicke, M., Erzinger, J., Herzig, P., Mühe R., 1993., Metallogenesis in back-arc environments; the Lau Basin example, Economic Geology v. 88(8), p. 2154-2181.

Fouquet, Y., Charlou, J. L., Costa, I., Donval, J. P., Knoery, J. R., Pelle, H., Ondreas, H., Lourengo, N., Segonzac, M., Tivey, M. K., 1994 A detailed study of the Lucky Strike hydrothermal vent site and discovery of a new hydrothermal site: Menez Gwen; Preliminary results of the DIVA 1 cruise (2-29 May), InterRidge News v. 3(2), p. 14-17.

Francheteau, J., Needham, H. D., Choukroune, P., Juteau, P., Seguret, M., Ballard, R. D., Fox, P. J., Normak, W., Carranza, A., Cordoba, D., Guerrero, J., Rangin, C., Bougault, H., Cambon, P., Hekinian, R., 1979., Massive deep-sea sulphide ore deposits discovered on the East Pacific Rise, Nature v. 277(5697), p. 523-528.

Fytikas, M., Innocenti, F., Manetti, P., Mazuoli, R., Peccerilo, A., Villari, L., 1984., Tertiary to Quaternary evolution of the volcanism in the Aegean Region. In: Dixon, J.E., Robertson, A.H.F. (Eds.), The Geological Evolution of the Eastern Mediterranean, Geol Soc London Spec Pub., v. 17, p. 687–699.

Ganeshram, R.S., Francois, R., Commeau, J. and Brown- Leger, S.L. 2003., An experimental investigation of barite formation in seawater. Geochim. Cosmochim, Acta, v. 67, p. 2599–2605

Goldberg, E.D. and Arrhenius, G. 1958., Chemistry of pelagic sediments, Geochim. Cosmochim. Acta, v. 13, p. 153–212.

Gontharet, S., Pierre, C., Blanc-Valleron, M.-M., Rouchy, J.M., Fouquet, Y., Bayon, G., Foucher, J.P., Woodside, J., Mascle,J. and The Nautinil Scientific Party. 2007., Nature and origin of diagenetic carbonate crusts and concretions from mud volcanoes and pockmarks of the Nile deep-sea fan (eastern Mediterranean Sea), Deep-Sea Res.II, v. 54, p. 1292–1311.

Gooday, A.J. and Nott, J.A. 1982., Intracellular barite crystals in two Xenophyaphores, Aschemonella Ramuliformis and Galatheammina Sp. with comments on the taxonomy of A. Ramuliformis, J. Mar. Biol. Assoc. UK, v. 62, p. 595–605.

Griffith, E. M. and Paytan A., 2012., Barite in the ocean – occurrence, geochemistry and palaeoceanographic applications, Sedimentology (2012) v. 59, p. 1817–1835

Gonza´lez-Mun˜ oz, M.T., Fernandez-Luque, B., Martinez-Ruiz, F., Chekroun, K.B., Arias, J.M., Rodriguez-Gallego, M., Martinez-Canamero, M., Linares, C.D. and Paytan, A. 2003., Precipitation of barite by Myxococcus xanthus: possible implications for the biogeochemical cycle of barium, Appl. Environ. Microbiol., v. 69, p. 5722–5725.

Guichard, F., Church, T.M., Treuil, M. and Jaffrezic, H. 1979., Rare earths in barites: distribution and effects on aqueous partitioning, Geochim. Cosmochim. Acta, v. 43, p. 983–997

Halbach, P., Nakamura, K. I., Washner, M., Lange, J., Sakai, H., Kasteliz, L., Hansen, R. D., Yamano, M., Post, J., Prause, B., Seifer, R., Michaelis, W., Teichman, F., Kinoshita, M., Marten, A., Ishibashi, J., Czerwinski S., Blum, N.,1989., Probable modern analogue of Kuroko-type massive sulphide deposits in the Okinawa Trough back-arc basin, Nature v. 338(6215), p. 496-499.

Halbach, P., Nakamura, K. I., Washner, M., Lange, J., Sakai, H., Kasteliz, L., Hansen, R. D., Yamano, M., Post, J., Prause, B., Seifer, R., Michaelis, W., Teichman, F., Kinoshita, M., Marten, A., Ishibashi, J., Czerwinski S., Blum, N 1993, Geology and mineralogy of massive sulphide ores from the central Okinawa Trough, Japan, Economic Geology v. 88(8), p. 2210-2225.

Halbach, P., Blum, N., Munch, U., Pluger., W., Garbe-Schoberg, D., Zimmer., M., 1998., Formation and decay of a modern massive sulfide deposit in the Indian ocean, Mineralium Deposita v. 33(3), p. 302-309.

Hannington, M. D., de Ronde, C. E. J., Petersen, S., 2005., Sea-floor tectonics and submarine hydrothermal systems, Economic Geology 100th Anniversary v. , p. 111–141.

Hannington, M., Jamieson, J. W., Petersen, S., Monecke, T., 2011., The abundance of seafloor massive sulphide deposits, Geology v. 39(12), p. 1155-1158.

Hannington, M. D. 2014., Volcanogenic Massive Sulfide Deposits. In Holland, H. D. (Ed.), Treatise on geochemistry, v. 2, p. 463-488.

Hannington M., Petersen S. and Krätschell A. 2017., Subsea mining moves closer to shore, Nat. Geosci. v. 10, p.158.

Hanor, J.S. 2000., Barite-celestine geochemistry and environments of formation, In: Reviews in Mineralogy & Geochemistry – Sulfate Minerals (Eds C.N. Alpers, J.L. Jambor and D.K. Nordstrom), . Mineralogical Society of America, Washington, D.C. v. 40, p. 193–275.

Hawthwore C. Frank, Krivovichev V. Sergey and Burns C. Peters 2000., The Crystal Chemistry of Sulfate Minerals, Reviews in Mineralogy and Geochemistry v. 40 (1), p. 1-112 DOI:10.2138/rmg.2000.40.1

Hanusa, T. P., Evans, W. J., 2013., Alkaline Earth Chemistry: Synthesis and Structures, Reference Module in Chemistry, Molecular Sciences and Chemical Engineering , v. 1, p. 2013, Pages 1133-1187.

Mißbach, H., Duda, JP., van den Kerkhof, A.M. et al. 2021., Ingredients for microbial life preserved in 3.5 billion-year-old fluid inclusions, Nat Commun v. 12, p. 1101. https://doi.org/10.1038/s41467-021-21323-z

Herzig, P.M. and W.L. Plüger 1988., Exploration for hydrothermal activity near the Rodriguez triple junction, Indian Ocean, Canadian Mineralogist v. 26(3), p. 721-736.

Hübscher C., Ruhnau M. and Nomikou P., 2015., Volcano-tectonic evolution of the polygenetic Kolumbo submarine volcano/Santorini (Aegean Sea), J. Volcanol. Geotherm. Res. v. 291, p.101–111.

Hein, J.R., Zierenberg, R.A., Maynard, J.B. and Hannington, M.D. 2007., Multifarious barite-forming environments along a rifted continental margin, Southern California Borderland, Deep-Sea Res.II, v. 54, p. 1327–1349.

Jamieson, J.W., Clauge, D. A., Hannington, M. D., 2014a., Hydrothermal sulfide accumulation along the Endeavour Segment, Juan de Fuca Ridge, Earth and Planetary Science Letters v. 395, p. 136–148.

Johnson, C.A., Piatak, N.M., and Miller, M.M., 2017., Barite (Barium), chap. D of Schulz, K.J., DeYoung, J.H., Jr., Seal, R.R., II, and Bradley, D.C., eds., Critical mineral resources of the United States—Economic and environmental geology and prospects for future supply: U.S. Geological Survey Professional Paper 1802, p. D1– D18.

Kastner, M., Craig, H., Sturz, A., 1987., Hydrothermal deposition in the Mariana trough: preliminary mineralogical investigation, EOS Transaction American Geophysical Union v. 68, p.1531.

Kilias, S. P., Nomikou, P., Papanikolaou, D., Polymenakou, P. N., Godelitsas, A., Argyraki, A., Carey, S., Gamaletsos, P., Mertzimekis, T. J., Stathopoulou, E., Goettlicher, J., Steininger, R., Betzelou, K., Livanos, I., Christakis, C., Bell, C. K., and Skoulos, M., 2013., New insights into hydrothermal vent processes in the unique shallow submarine arc-volcano, Kolumbo (Santorini), Greece, Scientific reports 3.

Krasnov, S. G., Cherkasev, G. A., Stepanova, T. V., Batuyev, B. N., Krotov, A. G., Malin, B. V., Maslov, M. N., Markov V. F., Poroshina, I. M., Samovarov, M. S., Ashadze A. M., Lazareva, L. I., and Ermolayev I. K., 1995., Detailed geological studies of hydrothermal fields in the North Atlantic, Geological Society, London, Special Publications v. 87(1), p.43-64.

Klaver, M.; Djuly, T.; Graaf, S.; Sakes, A.; Wijbrans, J.; Davies, G.; Vroon, P. 2015., Temporal and spatial variations in provenance of Eastern Mediterranean Sea sediments. Implications for Aegean and Aeolian arc volcanism, Geochimica et Cosmochimica Acta v. 153, p. 149-168.

Klaver, M.; Carey, S.; Nomikou, P.; Smet, I.; Godelitsas, A.; Vroon, P. 2016., A distinct source and differentiation history for Kolumbo submarine volcano, Santorini volcanic field, Aegean arc, Geochemistry, geophysics, geosystems v. 17 (8), p. 3254-3273.

Kong, L. S. L., Ryan, W. B. F., Mayer, L., Detrick R., Fox, P. J., and Manchester, K., 1985., Bare-rock drill sites, O.D.P. legs 106 and 109: evidence for hydrothermal activity at 23°N on the Mid-Atlantic Ridge, EOS (Trans., Am. Geophys. Union) v. 66, p. 936.

Le Maitre, R. W. 2002., Igneous rocks a Classification and Glossary of Terms Recommendations of the International Union of Geological Sciences, Sub-Commission on the Systematics of Igneous Rocks, Cambridge University Press, p. 236.

Le Pichon, X. and J. Angelier 1979., The Hellenic arc and trench system: a key to the neotectonic evolution of the eastern Mediterranean area, Tectonophysics v. 60(1), p. 1-42.

Lizasa, K., Fiske, R. S., Ishizuka, O., Yuasa, M., Hashimoto, J., Ishibashi, j., Naka, J., Horii, Y., Fujiwara, Y., Imai, A., Koyama, S., 1999., A Kuroko type polymetallic sulfide deposit in a submarine silicic caldera, Science v. 283(5404), p. 975-977.

Martha S. O., Dörr W., Gerdes A., Petschick R., Schastok J., Xypolias P. and Zulauf G. 2016. New structural and U–Pb zircon data from Anafi crystalline basement (Cyclades, Greece): constraints on the evolution of a Late Cretaceous magmatic arc in the Internal Hellenides, Int. J. Earth Sci. v. 105, p. 2031–2060.

Martinez, F. and B. Taylor 2003., Controls on back-arc crustal accretion: insights from the Lau, Manus and Mariana basins, Geological Society, London, Special Publications v. 219(1), p. 19-54.

Mercier-Langevin P., Hannington M. D., Dube B. and Becu V. 2011., The gold content of volcanogenic massive sulfide deposits, Miner. Depos. v. 46, p. 509–539.

Mizera M. and Behrmann J. H. 2016., Strain and flow in the metamorphic core complex of Ios Island (Cyclades, Greece), Int. J. Earth Sci. v. 105, p. 2097–2110.

Monecke, T., Petersen, S., Hannington, M. D., 2014., Constraints on water depth of massive sulphide formation: evidence from modern seafloor hydrothermal systems in arc-related settings., Economic Geology v. 109(8), p. 2079-2101.

Monecke, T., Petersen, S., Hannington, M. D., Grant, H., and Samson, I., 2016., The minor element endowment of modern sea-floor massive sulphide deposits and comparison with deposits hosted in ancient volcanic successions, Reviews in Economic Geology v. 18, p. 245–306.

Morgan, J.W. and Wandless, G.A., 1980., Rare earth element distribution in some hydrothermal minerals: evidence for crystallographic control, Geochim. Cosmochim. Acta,v. 44, p. 973–980.

Murchey, B.L., Madrid, R.J. and Poole, F.G. 1987., Paleozoic bedded barite associated with chert in western North America. In: Siliceous Sedimentary Rock-Hosted Ores and Petroleum, (Ed. J.R. Hein) Van Nostrand Reinhold, New York, p. 269–283.

Murton, B. J., Van Dover, C., Southward, E., 1995., Geological setting and ecology of the Broken Spur hydrothermal vent field: 29 degree 10 minute N on the Mid-Atlantic Ridge, Geological Society, London, Special Publications v. 87(1), p. 33.

Nakamura, K., Watanabe, H., Miyazaki, J., Takai, K., Kawagucci, S., Noguchi, T., Nemoto, S., Watsuji, T., Matsuzaki, T., Shibuya, T., Okamura, K., Mochizuki, M., Orishashi, Y., Tamaki, K., 2012., Discovery of new hydrothermal activity and chemosynthetic fauna on the Central Indian Ridge at 18°–20°S, PloS ONE v. 7(3), p. e32965.

Néron A., Bédard L. P., Gaboury D., 2018., The Saint-Honoré Carbonatite REE Zone, Québec, Canada: Combined Magmatic and Hydrothermal Processes, Minerals 2018, v. 8(9), p. 397.

Nomikou, P., Carey, S., Papanikolaou, D., Bell, K. C., 2012., Submarine volcanoes of the Kolumbo volcanic zone NE of Santorini Caldera, Greece, Global and Planetary Change v. 90–91, p. 135–151.

Nomikou, P., Papanikolaou, D., Alexandri, M., Sakellariou, D., Rousakis, G., 2013., Submarine volcanoes along the Aegean volcanic arc, Tectonophysics v. 597, p. 123-146.

Pasqualon N. G., Santos K. N. S., Marsellos A. E. and Kyriakopoulos K., 2016., Implications of petrography and geochemistry of athinios metamorphic units using PXRF and GIS analyses in Thera (Santorini, Greece), Bull. Geol. Soc. Greece v. 50, p.1980–1988.

Papanikolaou, D., 1993., Geotectonic evolution of the Aegean, Bulletin of the GeologicalSociety of Greece v. XXVII, p. 33–48.

Patten C. G. C., Pitcairn I. K., Teagle D. A. H. and Harris M., 2016., Mobility of Au and related elements during the hydrothermal alteration of the oceanic crust: implications for the sources of metals in VMS deposits, Miner. Depos. v. 51, p. 179–200.

Patten, C. G. C.; Pitcairn, I. K.; Teagle, D. A. H., 2017., Hydrothermal mobilisation of Au and other metals in suprasubduction oceanic crust. Insights from the Troodos ophiolite, Ore Geology Reviews v. 86, p. 487-508.

Pedersen, R.B., Rapp, H. T., Thorseth, I. H., Lilley, M. D., Barigga, F. J. A. S., Baumberger, T., Flesland, K., Fonseca, R., Fruh-Grenn, G. L., Jorgensen, S. L., 2010a., Discovery of a black smoker vent field and vent fauna at the Arctic mid-ocean ridge, Nature Communications v. 1(126).

Pedersen, R.B., Thorseth, I. H., Nygard, T. E., Liley, M. D., Kelley, D. S., 2010b., Hydrothermal activity at the Arctic mid-ocean ridges, Geophysical Monograph Series v. 188, p. 67–89.

Peillod A., Ring U., Glodny J. and Skelton A., 2017., An Eocene/Oligocene blueschist-/greenschist facies P–T loop from the Cycladic Blueschist Unit on Naxos Island, Greece: Deformation-related re-equilibration vs. thermal relaxation, J. Metamorph. Geol.v. 35, p. 805–830

Pe-Piper, G., Piper, D., 2002., The igneous rocks of Greece. Beitrage zur perionalen geologie der erde, Gebruder Borntraeger. v. 30, p. 573

Petersen, S., Monecke, T., Westhues, A., Hannington, M. D., 2014., Drilling shallow-water massive sulphides at the Palinuro volcanic complex, Aeolian island arc, Italy, Economic Geology v. 109(8), p. 2129-2158.

Petersen S. Lehrmann, B., Murton, B. J., 2018., Modern Seafloor Hydrothermal Systems: New Perspectives on Ancient Ore-Forming Processes, Elements v. 14 (5), p. 307-312.

Plüger, W. L., Herzig, P. M., Becker, K. P., 1990., Discovery of hydrothermal fields at the Central Indian Ridge, Marine Mining v. 9(1), p. 73-86.

Rizzo, A. L., Caracausi, A., Chavagnac, V., Nomikou, P., Polymenakou, P. N., Mandalakis, M., Kotoulas, G., Magoulas, A., Castillo, A., and Lampridou, D., 2016., Kolumbo submarine volcano (Greece). An active window into the Aegean subduction system, Scientific Reports v. 6, p. 28013.

Rogers, A.D., Tyler, P. A., Connelly, D. P., Copley., J. T., James, R., Larter, R. D., Linse, K., Mills, R. A., Garabato, A. N., Pancost, R. D., Pearce, D. A., Polunin, N. V. C., German, C. R., Zwirglmaier, K., 2012., The discovery of new deep-sea hydrothermal vent communities in the Southern Ocean and implications for biogeography, PLoS Biology v. 10, p. e1001234.

Rona, P. A., Klinkhammer, G., Nelsen, T. A., Trefry, J. H., Elderfield, H., 1986., Black smokers, massive sulphides and vent biota at the Mid-Atlantic Ridge, Nature v. 321(6065), p. 33-37.

Rona, P.A., and Scott, S.D., 1993., A special issue on sea-floor hydrothermal mineralization: New perspectives–Preface, Economic Geology, v. 88, p. 1933–1976.

Ropp R. C. 2013., Encyclopedia of the Alkaline Earth Compounds, p. 599-566.

Rye O. Robert 2004., A review of the stable-isotope geochemistry of sulfate minerals in selected igneous environments and related hydrothermal systems, Chemical Geology v. 215, p. 5 – 36.

Royden, L.H., Papanikolaou, D.J., 2011., Slab segmentation and late Cenozoic disruption of the Hellenic arc, Geochemistry, Geophysics, Geosystems v.12, p.3-10.

Schmidt, M. W., Poli, S., 1998., Experimentally based water budgets for dehydrating slabs and consequences for arc magma generation, Earth and Planetary Science Letters v. 163 (1-4), p. 361-379..

Shikazono N., 1994., Precipitation mechanisms of barite in sulfatesulfide deposits in back-arc basins. Geochim. Cosmochim, Acta v. 58, p. 2203–2213.

Sigurdsson, H., Carey, S., Alexandri, M., Vougiouklakis, G., 2006., Marine investigations of Greece's Santorini volcanic field, EOS, Transactions American Geophysical Union v. 87(34), p. 337-342.

Spiess, F.N., Macdonald, K. C., Atwater, T., Ballard, R., Carranza, A., Cordoba, D., Cox, C., Garcia, V. M. D., Franchetau, J., Guerrero, J., Hawkins, J., Haymon, R., Hessler, R., Juteau, T., Kastner, M., Larson R., Luyendyk, B., Macdougall, J. D., Miller, S., Normak, W., Orcutt, J., and Rangin, C., 1980., East Pacific Rise: Hot springs and geophysical experiments, Science v. 207, p. 1421–1433.

Stamatakis, M.G. and Hein, J.R., 1993., Origin of barite in Tertiary marine sedimentary-rocks from Lefkas Island, Greece, Econ. Geol., v. 88, p. 91–103.

Stoffers, P., Wright, I. C., de Ronde, C. E. J., Hannington, M. D., Villinger, H., Herzig, P., 1999., Little-studied arc-backarc system in the spotlight, EOS Transaction American Geophysical Union v. 80, p. 353-364.

Stoffers, P., Worthington, T., Schwarz-Schampera, U., Hannington, M. D., Massoth, G., Hekinian, R., Schmidt, M., Lundsten, L., Evans, L., Vaiomo'unga , R., Kerby, T., 2006., Submarine volcanoes and high-temperature hydrothermal venting on the Tonga arc, southwest Pacific, Geology v. 34, p. 453–456.

Sun W., Arculus R. J., Kamenetsky V. S. and Binns R. A., 2004., Release of gold-bearing fluids in convergent margin magmas prompted by magnetite crystallization, Nature v. 431, p. 975–978.

Swinbanks, D.D. and Shirayama, Y.,1986., High levels of natural radionuclides in a deep-sea infaunal xenophyophore, Nature, v. 320, p. 354–358.

Tendal, O.S.n 1972.,A monograph of the Xenophyophoria (Rhizopodea, Protozoa). Galathea, Rep., v. 12, p. 7–103.

Tivey, M. K., 2007., Generation of seafloor hydrothermal vent fluids and associated mineral deposits, Oceanography v. 20(1), p. 50-65.

Ueno, H., Hamasaki, H., Murakawa, Y., Kitazono, S., and Takeda, T., 2003., Ore and gangue minerals of sulfide chimneys from the North knoll, Iheya Ridge, Okinawa trough, Japan, JAMSTEC Journal of Deep Sea Research v. 22, p. 49–62.

Van Beek, P., Francois, R., Conte, M., Reyss, J.-L., Souhaut, M. and Charette, M., 2007., 238Ra/226Ra and 226Ra/Ba ratios to track barite formation and transport in the water column, Geochim. Cosmochim. Acta, v. 71, p. 71–86.

Von Damm K. L., 2000., Chemistry of hydrothermal vent fluids from 9–10 N, East Pacific Rise:“Time zero,” the immediate posteruptive period, J. Geophys. Res. Solid Earth v. 105, p. 11203–11222.

Wright, I.C., de Ronde, C. E. J., Faure, K., Gamble, J. A., 1998. Discovery of hydrothermal sulfide mineralization from southern Kermadec arc volcanoes (SW Pacific), Earth and Planetary Science Letters v. 164: p. 335–34

Yang, K.; Scott, S. D., 2006., Magmatic Fluids as a Source of Metals in Seafloor Hydrothermal Systems, (Geophysical Monograph Series), Nature v. 383, p. 163-184.

Zegkinoglou N., 2020., Concentration and speciation of thallium in modern seafloor massive sulphides, Kolumbo arc-volcano (Santorini), Greece: Insights from laser ablation-inductively coupled plasma-mass spectrometry (LA-ICP-MS)”. Master Thesis. National and Kapodistrian University of Athens.

Appendix

Figure 46: Display of all the available spectrums from the SEM-EDS analyses

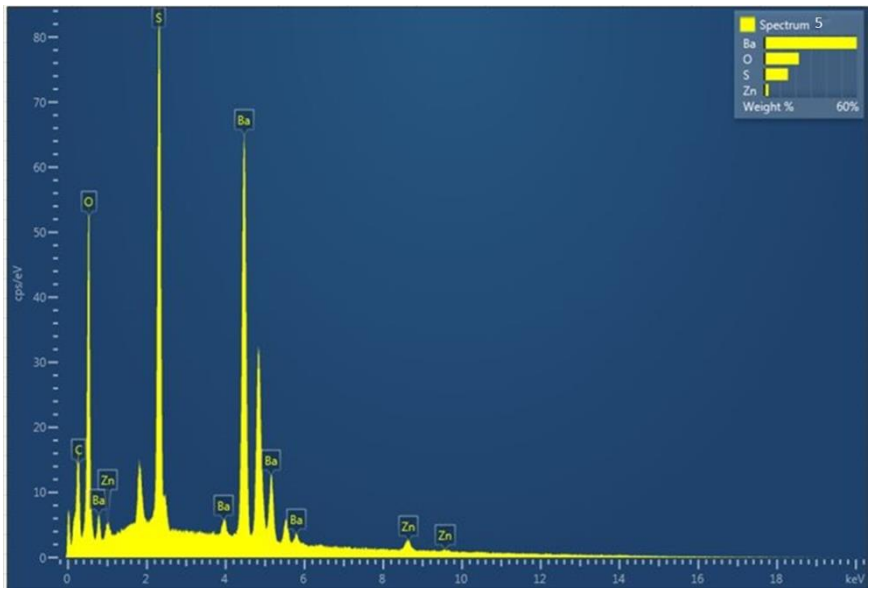

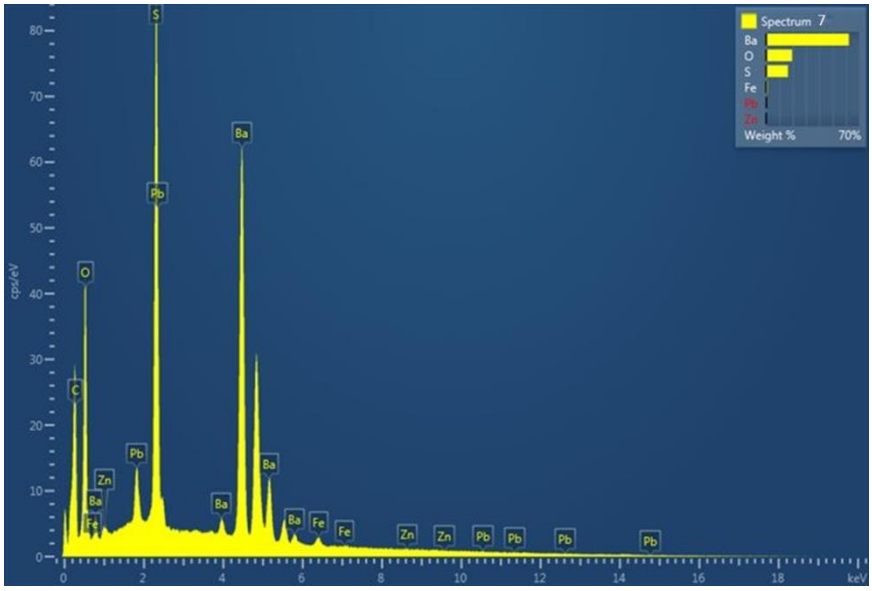

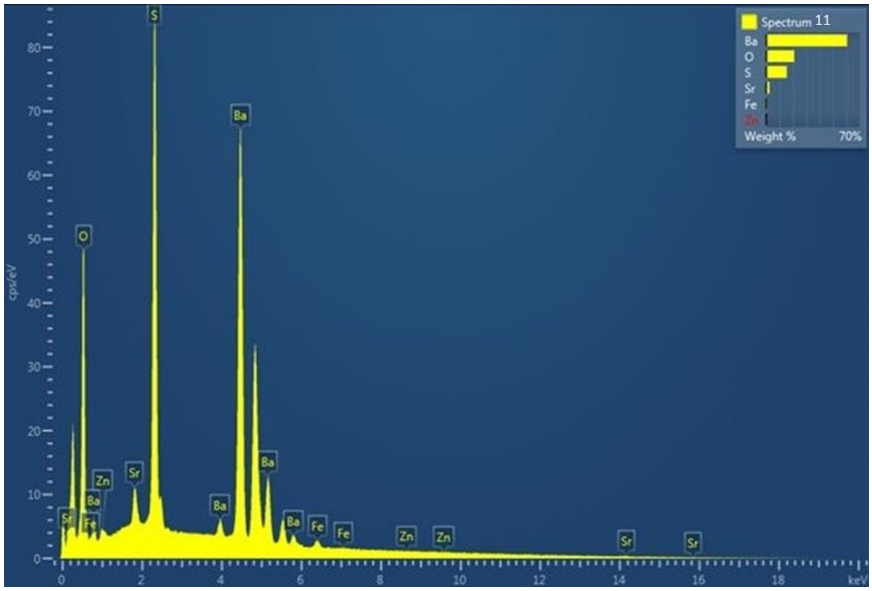
Spectrum 11
Ba
O
S
Sr
Fe
Zn
Weight % 70%
cps/eV
keV

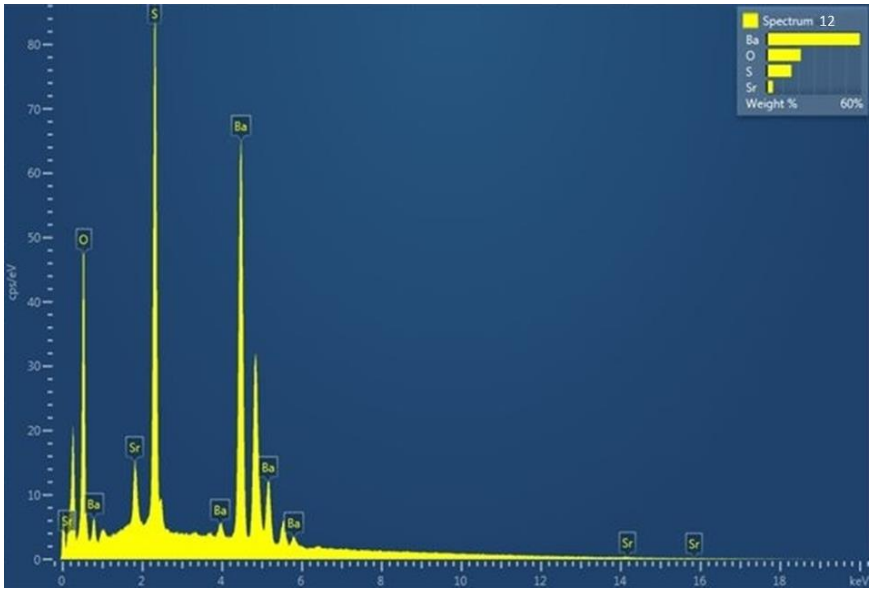
Spectrum 12
Ba
O
S
Sr
Weight % 60%
cps/eV
keV

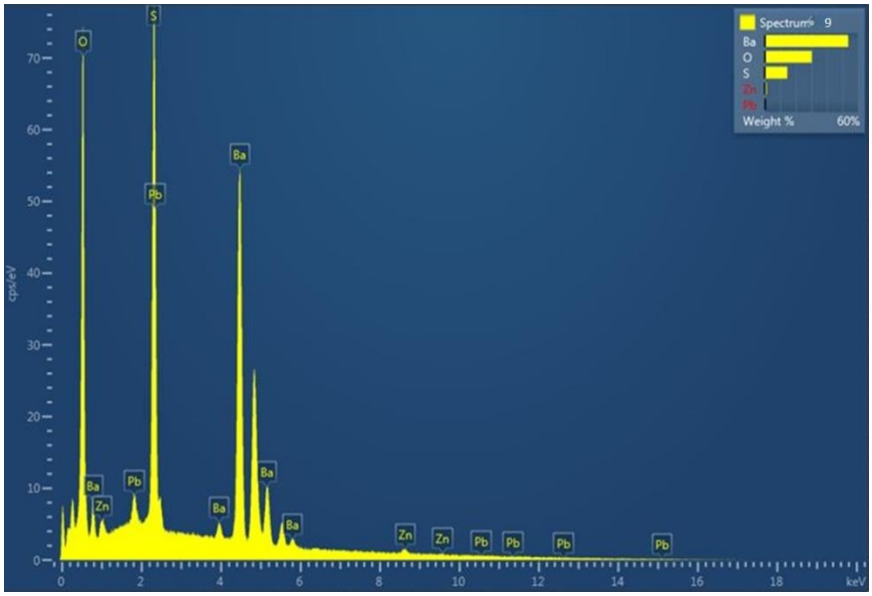
Spectrum 9
Ba
O
S
Zn
Pb
Weight % 60%
cps/eV
keV

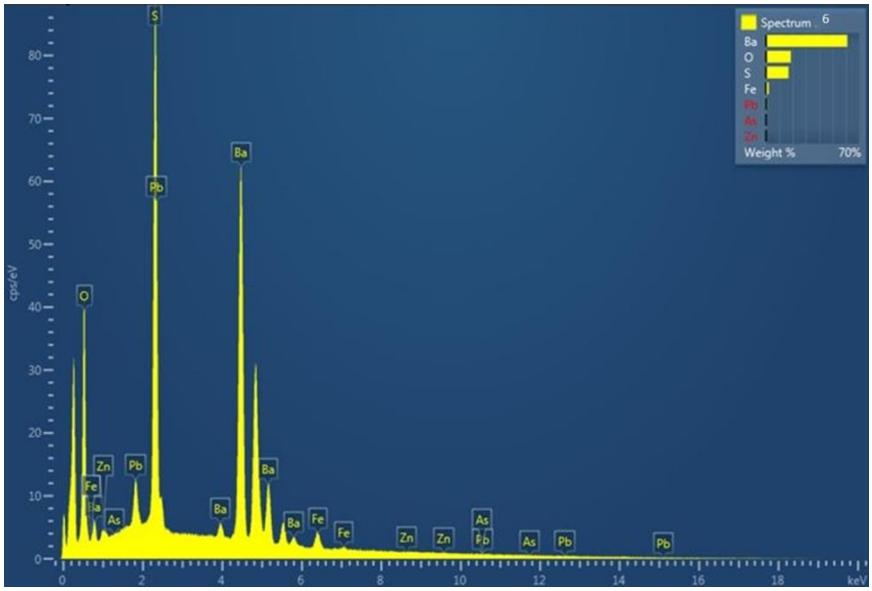
Spectrum 6
Ba
O
S
Fe
Pb
As
Zn
Weight % 70%
cps/eV
keV

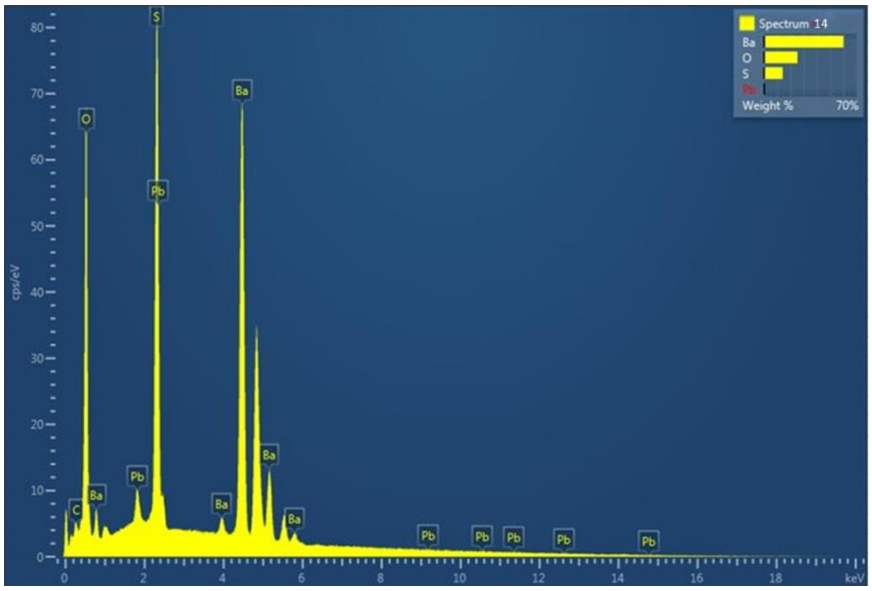
Spectrum 14
Ba
O
S
Pb
Weight % 70%
cps/eV
keV

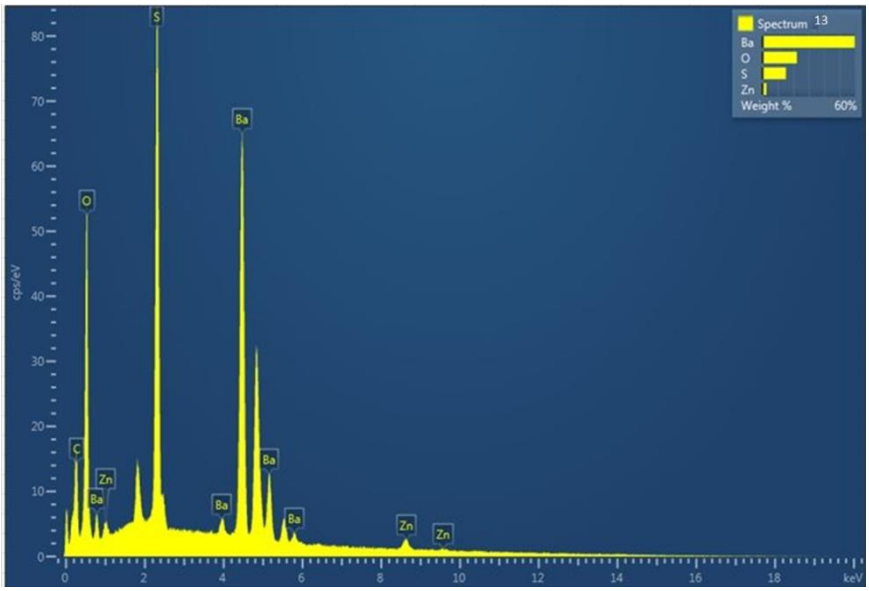
Spectrum 13
Ba
O
S
Zn
Weight % 60%
cps/eV
keV

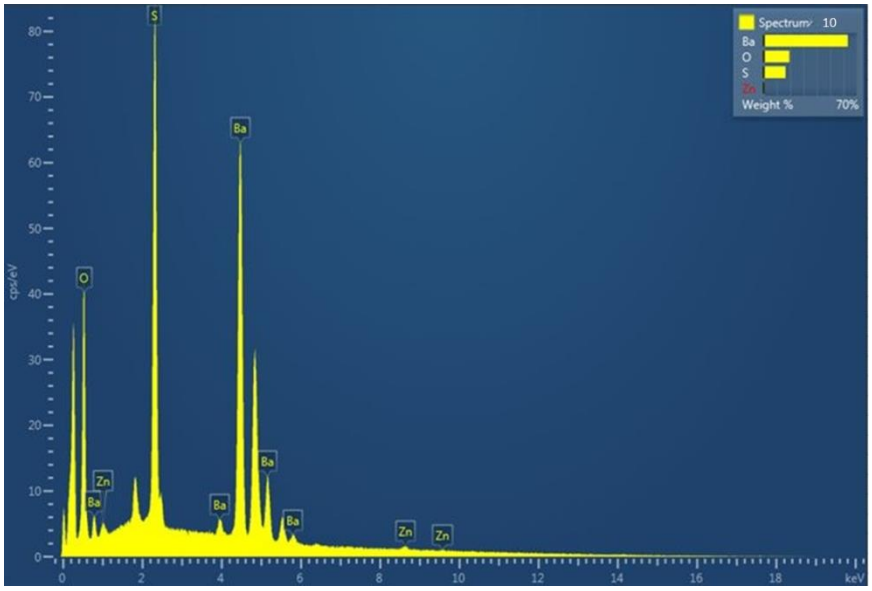
Spectrum 10
Ba
O
S
Zn
Weight %
70%
cps/eV
keV
S
Ba
O
Zn
Ba
Ba
Ba
Ba
Zn
Zn

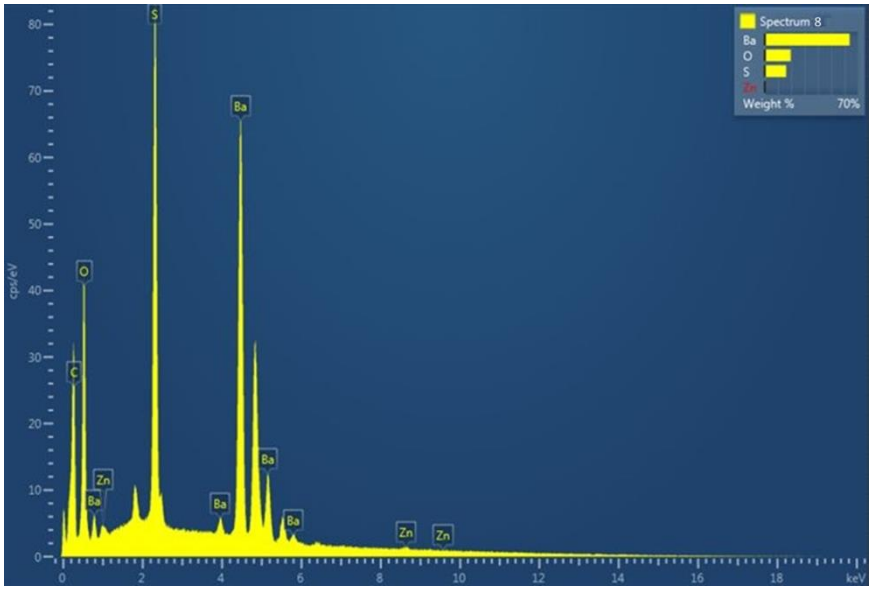
Spectrum 8
Ba
O
S
Zn
Weight %
70%
cps/eV
keV
S
Ba
O
C
Zn
Ba
Ba
Ba
Ba
Zn
Zn